HIGH PRESSURE OPTICAL STUDIES

OF SEMICONDUCTORS

A Thesis Submitted to

the Faculty of Engineering of the University of Glasgow

for the Degree of Doctor of Philosophy

by

Haiping Zhou

October   1992

ProQuest Number: 13834019

ProQuest 13834019

Acknowledgements

Any scientific research nowadays must, ultimately, be a joint effort of many individuals and varieties of expertise. My thesis could not have been begun, never mind completed, without the help of many such individuals.

Over the last three years I have been greatly indebted to my supervisor, Dr Clivia Sotomayor Torres. Her patient help, insightful comment, constant encouragement in my research and friendship have been invaluable.

My work colleagues in the spectroscopy laboratory deserve special mention. The technical staff, Doug Irons and Alex Ross, have provided excellent support, above and beyond the call of duty, promptly solving irritating experimental problems raised. Many hours of informal discussion with Morag Watt, William Rodden and Peidong Wang, fellow colleagues in 3.8, were invaluable.

I thank M. I. Eremets at the High Pressure Physics Institute in USSR for the gift of the micro-diamond anvil cell which has been used in my experiments. Samples for this work were provided by B. Lunn and D. E. Ashenford at the University of Hull for CdTe/CdMnTe samples, E. G. Scott at British Telecom Research Lab. for AlInAs samples and G. Armelles at the National Centre of Microelectronics in Spain for GaAs/GaP samples. For these I am very grateful.

I would like to thank the University of Glasgow for awarding me with a post-graduate scholarship and the Overseas Research Students Scholarship for providing additional finance during the three years.

My husband Alan Johnston has given me much support since we met during my Ph.D studies. He has often given me the confidence and the understanding I needed.

Any thesis represents far more than the required three years study. Essentially, it is the culmination of many years of study. Therefore, the people to whom I owe the most are my parents and family in China. Without their many years of self-sacrifice, patience, constant encouragement and support, throughout my academic career, this thesis would never have been possible. To them I will be eternally grateful.

I dedicate this thesis to

my parents

for the love and care they have shown me over the years.

ABSTRACT

Until this work was completed no detailed studies of the low-temperature emission of $Al_{0.48}In_{0.52}As$ under high pressures were available to the best of our knowledge. We investigated the low-temperature emission of $Al_{0.48}In_{0.52}As$ under high pressures from 1 bar up to 92 kbar, especially with respect to the changes in luminescence mechanisms that occur concurrently with the crossover between the direct- and indirect-related bands. By investigating the temperature and excitation power dependence of the photoluminescence (PL) together with the photoluminescence excitation (PLE), we demonstrated that the low-temperature emission of $Al_{0.48}In_{0.52}As$ is not excitonic but due to (D^O, A^O) transitions with a relatively deep acceptor of ~ 68 meV, which occurs in both the direct- and in the indirect-related bands. We suggest that the shallow donor ground states associated with the X- and the Γ- conduction bands seem to be tied quite rigidly to these conduction bands. Variations in the donor binding energies with the pressure and the direct-indirect crossover seem to be minor. The linear pressure coefficients α^{Γ} and α^X of the (D^O, A^O) related to the Γ- and X- minima in the conduction band are 7.9 ± 0.1 and ~ 2.9 ± 0.1 meV/kbar, respectively. The Γ-X related state crossover occurs at ~ 52.5 ± 0.5 kbar at 2 K.

We studied the optical properties of a type-II $(GaAs)_6/(GaP)_6$ strained-layer super-lattice (SLS) grown on a GaAs substrate. $(GaAs)_6/(GaP)_6$ is a spatially indirect (type-II) SLS and the lowest conduction band is X level in GaP layers. The energy separation between the X-related state in GaP layers and the Γ-related state in GaAs layers is ~ 44 meV, which was found to decrease with time. Therefore, the type-II $(GaAs)_6/(GaP)_6$ SLS is mechanically unstable. The strain relaxation is a crucial problem in this kind of systems. We also discovered that the temperature dependence of the PL spectrum for this type-II $(GaAs)_6/(GaP)_6$ SLS is different from previously reported results.[4.10] We

probably observed strain relaxation induced optical transitions, which may be associated with defects or impurities related to the Γ- and the X-conduction bands.

The PL properties of CdTe/Cd$_{1-x}$Mn$_x$Te MQWs and SQWs with well widths from 2 to 15 nm has been studied as a function of hydrostatic pressure (0 − 35 kbar) at 4 K. No band crossovers were observed before the phase transition at ∼ 33 kbar. The pressure coefficient is found to increase with decreasing well width, as in InGaAs/-GaAs strained QWs but unlike that observed in the unstrained GaAs/AlGaAs QWs. The magneto-optical spectra of CdTe/Cd$_{1-x}$Mn$_x$Te QWs have been investigated as a function of hydrostatic pressures at 4 K. The band gap of the Cd$_{1-x}$Mn$_x$Te barrier layers decreases with increasing magnetic fields. We found that the magnetic field dependence of the luminescence intensity of the Cd$_{1-x}$Mn$_x$Te layers can be dramatically changed by high pressures due to the variations of the distance between the carriers and the Mn ions with pressure. CdTe/Cd$_{1-x}$Mn$_x$Te MQWs (x = 0.063), the CdTe wells (L$_W$ = 10 nm) have no detectable exciton energy shift with field at atmospheric and high pressures. In contrast, in CdTe/Cd$_{1-x}$Mn$_x$Te SQWs (x = 0.125), the CdTe well (L$_W$ = 2 nm) has large energy shifts with magnetic field under high pressures. These behaviours are consistent with the degree of penetration of the electron-hole pair wavefunction into the DMS barrier layers.

HIGH PRESSURE OPTICAL STUDIES

OF SEMICONDUCTORS

Ch. 2. Experimental Approaches

Ch.3. Optical Properties of $Al_{0.48}In_{0.52}As$ under hydrostatic Pressures

Ch. 4. Optical Properties of GaAs/GaP Strained-Layer Superlattices

Ch. 5. Megneto-Optical Studies of CdTe/CdMnTe QWs under High Pressures

List of Tables

List of Figures

List of Papers

Published:

1. "Magneto-optical Studies of High Pressure Spectroscopy of CdTe/CdMnTe Quantum Wells", H. P. Zhou, C. M. Sotomayor Torres, B. Lunn and D. E. Ashenford, to appear in the Proceedings of the 21th International Conference on the Physics of Semiconductors, (Beijing, August 1992).

2. "Optical Properties of a Type-II GaAs/GaP Strained-layer Superlattice", H. P. Zhou and C. M. Sotomayor Torres, the SPIE Proceedings, Vol. 1675, 186 (1992).

3. "Luminescence Properties of $Al_{0.48}In_{0.52}As$ under Hydrostatic Pressures", H. P. Zhou and C. M. Sotomayor Torres, the SPIE Proceedings, Vol. 1678, 96 (1992).

4. "Pressure Dependence of Photoluminescence of CdTe/CdMnTe Quantum Wells", H. P. Zhou, C. M. Sotomayor Torres, B. Lunn and D. E. Ashenford, the SPIE Proceedings, Vol. 1675, 203 (1992).

To be published:

1. "Optical Properties of CdTe/CdMnTe Quantum Wells under High Pressures and Magnetic Fields", H. P. Zhou, C. M. Sotomayor Torres, B. Lunn and D. E. Ashenford, to be supplied to J. Appl. Phys.

2. "High Pressure Spectroscopy of $Al_{0.48}In_{0.52}As$ at Low Temperature", H. P. Zhou and C. M. Sotomayor Torres, to be supplied to J. Appl. Phys.

3. "Strain Relaxation of Strained-Layer Superlattice GaAs/GaP", H. P. Zhou and C. M. Sotomayor Torres, to be supplied to Appl. Phys. Letters.

Ch. 1. THEORY AND REVIEW

Ch. 1. THEORY AND REVIEW

1.1 Introduction

Over the last decade, an area which has seen the greatest advances within semiconductor physics has been that of low dimensional structures (LDS). This field covers the growth, characterization, fabrication and physics associated with thin, lattice matched and mismatched, semiconductor layers and devices.

It was the development of growth techniques such as molecular beam expitaxy (MBE) and metal-organic chemical vapour deposition (MOCVD) which allowed the realization of superlattice structures. These novel growth techniques have caused a revolution within devices physics; quantum well lasers where the emission energy is tuned by varying well thickness and high electron mobility transistors have been produced, the properties of which depend on engineered band structure.

For future applications and to add to our understanding of fundamental physics, compound semiconductor materials with reduced dimensionality are increasingly being investigated. When the thickness is compared to the De Broglie wavelength of a carrier within a superlattice then quantum mechanical size effects, such as discrete energy levels within the band-structure occur. The dramatic changes in the energy spectrum and the density of states alter many properties of these systems.

The optical and electronic properties of quantum wells (QWs) and superlattices (SLs) have been studied extensively both theoretically and experimentally in recent years. The measurement of photoluminescence (PL) under hydrostatic pressure can be used as a powerful method for the investigation of semiconductor band structures and impurity states. This technique has also been employed to study the electronic properties of the QWs and SLs since the nature of Wannier excitons confined in the SLs

and QWs have attracted considerable interest. High magnetic fields, which further quantize the energy levels and thus provide discrete optical spectra, have proved to be a useful means to study exciton states in QWs.

The main advantages of high pressure (HP) techniques include:

(1) HP can be used to perturb artificial semiconductor structures and change their lattice constants. These changes affect important parameters such as energy gaps and effective masses and, to a lesser degree, the dielectric constants.

(2) HP can continuously change the relative energy positions of Γ, L, X valleys due to their very different pressure coefficients. This property can be used to determine:

(a) the nature of the lowest conduction band states;

(b) the energy separation between Γ- and X-levels;

(c) band offsets in QW's and SL's;

(d) Γ-X mixing effects.

(3) HP can change the carrier density, it is possible to measure mobility on the same sample, at different carrier densities.

The obvious advantage of HP is that it can be used as an external parameter to modify the electronic structure without changing the intrinsic properties of the material, consequently HP is a powerful method for studying the electronic and optical properties of QWs and SLs.

The aims of my research work involve the use of high pressure techniques to perturb artificial semiconductor structures which hold promise for optoelectronic devices, in the quest to:

(1) Investigate the electronic structures and optical properties,

(2) Determine the dominant emission mechanisms,

(3) Study the effect of impurities upon the light emitting properties,

(4) Understand the pressure dependence of recombination mechanisms,

all as function of band-gap variation in III-V and wide-gap II-VI semiconductor structures (lattice matched and mismatched) grown by MBE. High resolution optical spectroscopy techniques as well as magneto-optical measurements are used.

In this work, chapter 1 provides the basic understanding of the luminescence properties of direct band gap semiconductors and is extended to show how reduction of the dimensionality results in strong quantum confining effects. Hydrostatic pressure and strain effects are also described. Chapter 2 details the experimental approaches, the setting up of a photoluminescence excitation and collection system, and the use of two diamond anvil cells, suitably modified, for optical spectroscopy at high pressures, low temperatures and strong magnetic fields.

Chapter 3 gives to the best of our knowledge, the first in depth investigation of the optical properties of $Al_{0.48}In_{0.52}As$ under hydrostatic pressures up to ~ 92 kbar at temperature T = 2 K, particularly considering the mechanisms of the low temperature emission and the pressure dependence of the emission. This work was motivated because $Al_{0.48}In_{0.52}As$ was becoming more and more technologically important in devices such as HEMTs and superlattice structures.

In chapter 4, the assignment of the excitonic emissions from a type-II GaAs/GaP strained layer superlattice is made. The temperature and excitation power dependences of the emissions are explained. Chapter 5 explores to the best of our knowledge, the first investigation of magneto-optical spectroscopy of $CdTe/Cd_{1-x}Mn_xTe$ quantum wells under high pressures. The experiments and theories involved in the project and the purpose of the research are described. Then in the final chapter, future research topics arising from this work are presented.

1.2 Low Dimensional Effects

1.2.1 Superlattices and Quantum Wells

Since the pioneering work of Esaki and Tsu in 1970,[1.1] a considerable amount of results have been obtained as regards the physical and device properties of semiconductor heterostructures following the concept of semiconductor superlattice proposed by them: a periodic structure of alternating ultra thin layers.

If the layer thickness is comparable to the De Broglie wavelength of a carrier within the superlattice then quantum mechanical size effects, such as discrete energy levels within the band structure occur. When two finite quantum wells are placed near each other such that the barrier between them is small enough to allow interaction between the wells, the degenerate states split into two bound states of nearly the same energy. If this multiple quantum well arrangement is extended to many wells placed together, then the energy levels broaden into bands, much like the energy bands of the host crystal which are due to the periodicity of the atomic lattice. The differences are that the quantum well lattice is one dimensional with a period several times larger than that of the crystal, and the energy bands, due to the coupled wells, are superimposed onto the allowed energy bands of the host. Superlattice structure gives rise to a new band structure, which is due to an array of square wells of width L_w, separated by barriers of width L_b and height U_o.

With the development growth techniques such as Molecular Beam Epitaxy (MBE) and Metaloganic Vapor Phase Epitaxy (MOVPE), it has become possible to grow high quality semiconductor superlattices and quantum well structures and tailor the band structures to achieve the desired electronic properties and device applications. Very thin (lattice matched and mismatched) epitaxial layers can thus be deposited, defined on the

monolayer scale. Fig. 1.1 shows the energy gaps for different materials and their respective lattice constants.[1.43]
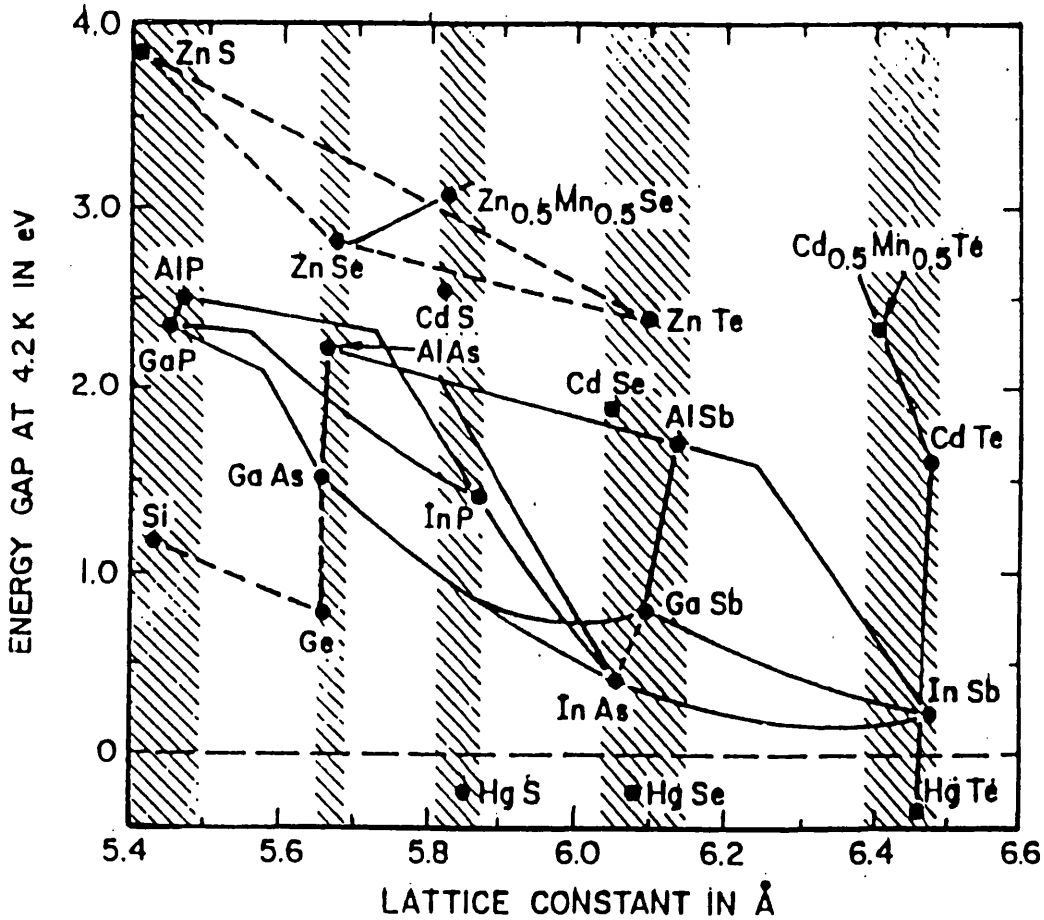
Fig. 1.1 Energy gaps at 4.2 K against lattice constants (After Esaki 1986).

The interest in these low dimensional structures is primarily motivated by strong quantum confining effects produced by reducing the dimensionality from three dimensions (3D) to quasi-two dimensions (Q2D). Because lower dimensional structures have larger confining effects, reduction of dimensionality can be extended, in principle, to quasi-one dimension (Q1D) and quasi-zero dimension (Q0D) to further increase the quantum confining effect.

In the case of 3D or bulk materials, the density of states (DOS) follows an $E^{1/2}$ dependence on the energy of the carrier and the occupation of the energy levels is governed by Fermi-Dirac statistics. Lowering the dimensionality to 2D leads to a step-like DOS. In 1D the edges of the 2D DOS develop a spike with a tail decaying as $E^{-1/2}$ to high energies, and finally in 0D the DOS is reduced to a set of δ-functions. Fig. 1.2 shows the schematics of 3D, 2D, 1D and 0D quantum systems and corresponding DOS's.
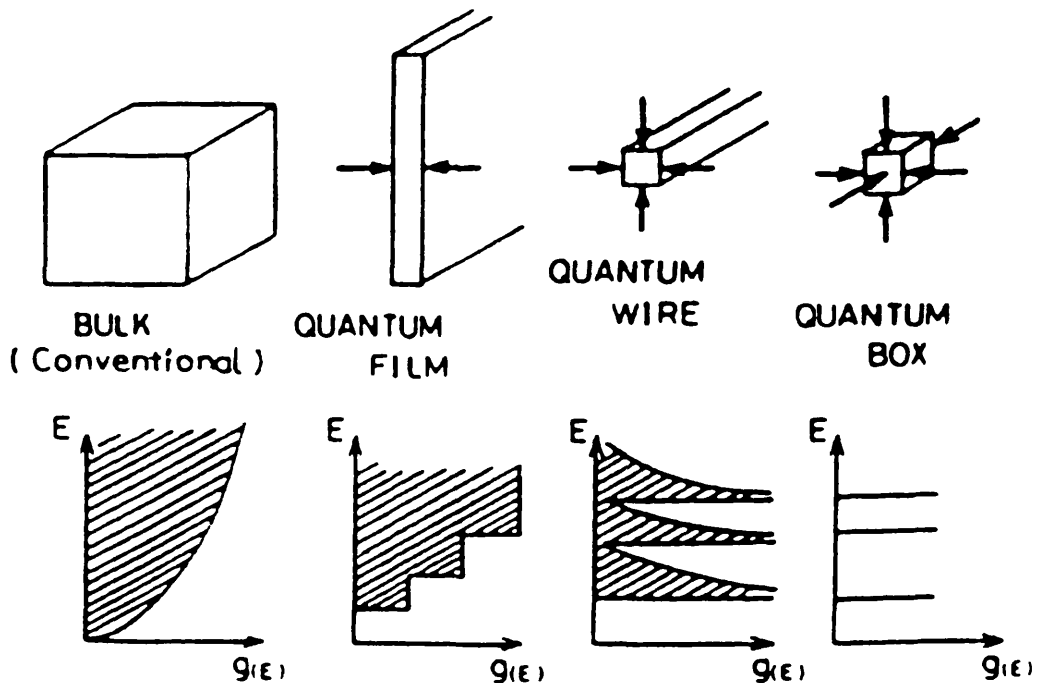
Fig. 1.2 Schematics of 3D, 2D, 1D and 0D quantum systems and corresponding DOS's.

With progress of microfabrication technology, we expect that Q1D and Q0D structures can be fabricated for device applicatons in the near future. Since devices can be designed to have structures with any of these dimensions and sizes, it is important to know the electronic and optical properties of structures with lower dimensions.

1.2.2 Optical Transitions

Interband optical phenomenon can be described within the terms of the dielectric function in which the absorption coefficient $\alpha(\omega)$ is directly proportional to the imaginary part of $\varepsilon(\omega) = \varepsilon_1(\omega) + i\, \varepsilon_2(\omega)$.[1.2] Therefore, optical transitions are induced by an electromagnetic wave (e.m) between electronic states $|m\rangle$ and $|n\rangle$ at a rate calculated using Fermi's golden rule. We can write:[1.2]

$$\alpha(\omega) \sim \varepsilon_2(\omega) \sim |<n\,|\,\mathbf{e}\cdot\mathbf{p}\,|\,m>|^2\, \varrho(\omega) \qquad (1.1)$$

where m and n are initial and final states of the optical transition, $\mathbf{e}$ and $\mathbf{p}$ are the light polarization vector and momentum operator, respectively, and $\varrho(\omega)$ is the density of states at energy ω. The wavefunctions $|m\rangle$ and $|n\rangle$ are given by

$$\Psi^{m,\,n}(r) = \Phi^{e,\,h}(z)\, \exp^{i\,k_{//}\cdot r_{//}}\, u_{c,\,v,\,k}(r), \qquad (1.2)$$

where $\Phi^{e,\,h}(z)$ represents the confined electron (or hole) envelope wavefunction, $k_{//}$ and $r_{//}$ are the transverse momentum and position, $u_{c,\,v,\,k}(r)$ are the usual periodic part of the Bloch wavefunctions.

In calculating the matrix element in Eq. (1.1) it can factorize into a sum at the lattice points R_i of the slowly varying envelope wavefunction and an integral over the unit cell of the fast varying part of the Bloch functions. Thus

$$|<n\,|\,\mathbf{e}\cdot\mathbf{p}\,|\,m>| = \Sigma_{R_i}\, \Phi^e(R_i)\, \Phi^h(R_i)\, \exp^{i\,(k_{e//} - k_{h//})\cdot R_i}$$

$$\cdot \int_{\Omega} u_{(c,\,ke//)}\, \mathbf{e}\cdot\mathbf{p}\, u_{(v,\,kh//)}\, dr^3. \qquad (1.3)$$

The integral is independent of R_i and is the usual bulk matrix element p which contains the selection rules due to light polarization and band symmetry. The sum yields, after transformation back to an integral and taking into account normalization factors:

$$| < n \, | \, e \bullet p \, | \, m > | \sim L_z^{-1/2} < \Phi^e \, | \, \Phi^h > p \, \delta_{(ke//, \, kh//)} \, . \qquad (1.4)$$

Since $k_{e//} = k_{h//}$ then transitions are vertical. The DOS is constant in two-dimensional systems, thus equation (1.1) becomes

$$\alpha(\omega) \, L_z \sim \varepsilon_2 \, (\omega) \, L_z \sim \text{const.} < \Phi^e \, | \, \Phi^h >^2 p^2 \sim \text{const. } p^2 \, . \qquad (1.5)$$

Because p^2 is almost constant for all semiconductors ($p^2 / 2 \, m_o \sim 23$ eV) then $\alpha \, (\omega)$ is almost independent of well thickness, 6×10^{-3} per transition per quantum well.

When a semiconductor crystal is excited by an optical pump such as a laser, electrons are excited to the conduction band leaving behind a hole in the valence band; subsequently the excited carriers relax towards the band edge on a picosecond time scale. If the electron and the hole stay within the vicinity of each other coulombic attraction occurs to form a bound electron-hole pair, an exciton. In III-V semiconductors the electrons and holes form loosely bound Wannier excitons and are free to move throughout the whole crystal. The exciton has no associated charge transfer and forms the lowest excited state of the whole crystal.

In a quantum well, due to the quantum size effect, excitons have characteristics different from those in bulk material. The exciton becomes quasi-two dimensional, its binding energy is enhanced, the degeneracy of heavy- and light-hole band is removed, resulting in two exciton systems.

The exciton can be described by a two particle envelope wavefunctions with either 0

or 1 occupancy, so

$$\alpha(\omega) \sim \varepsilon_2(\omega) \sim |<0 | e \cdot p | \Psi_{exc} >|^2$$

$$\sim |<u_{c, ke} | e \cdot p | u_{v, kh} >|^2 | \Phi^n |^2 \delta_{(0, k)} , \qquad (1.6)$$

where $| \Phi^n |^2$ is a measure of the electron-hole wavefunction overlap which decreases

rapidly with n. In type I quantum wells $| \Phi^n |^2$ is correspondingly larger than in the bulk

material and the exciton binding energy increases as well width decreases. Considering

that only the exciton state which matches the light momentum can be coupled to

incoming photons[1.3], the exciton appears as a sharp peak in the emission spectrum due

to the k conservation rule, $\delta_{(0, k)}$, although this may be relaxed due to interface

disorder.

1.2.3 Selection Rules

In type-I quantum wells the electron and hole wavefunctions are localized in the

same quantum layer. For an infinite well Φ^e and Φ^h are orthogonal, so $< \Phi^e | \Phi^h >$ is

zero unless the wavefunctions have the same quantum number, thus $\Delta n = 0$ selection

rule. For finite depth wells, the conduction and valence wavefunctions are no longer

exactly orthogonal as the penetration of the wavefunction in the barrier layer depends

on the quantum number. However, the single-particle wavefunctions still retain their

parity (even or odd), due to the symmetric confinement potential and $\Delta n = 0$ transitions

with either even or odd parity become weakly allowed.

According to the correspondence principle, quantum mechanical electric dipoles

radiate like their classical counterparts.[1.4] Therefore, zero-order selection rules on the

optical matrix element p and radiation patterns can be deduced from atomic physics.

Fig. 1.3. shows the dipole moment between an electron s-state and a hole p-state and the emission diagram. Although this description is somewhat oversimplified, excitons tend to retain these selection rules if band mixing effects are neglected.[1.5]
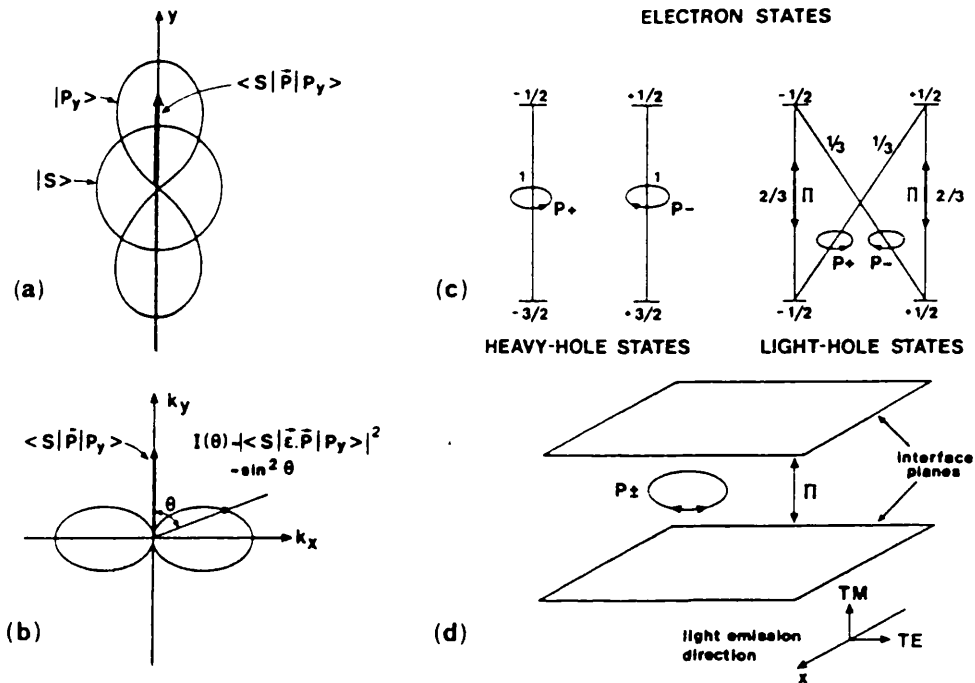
Fig. 1.3. Optical selection rules for absorption and luminescence between atomic-like states (Bloch states) of valence and conduction band (After Weisbuch 1987).

(a) Dipole matrix element between an s and a p state.

(b) Emission diagram of that dipole according to the correspondence principle.

(c) Possible dipole moments between conduction and valence band states; p+(-) indicate rotating dipole moments, which emit circularly polarized light; π indicates a linearly polarized dipole. Relative dipole strengths are indicated.

(d) Geometry of the dipoles in the quantum well situation. One can see that heavy-holes only emit TE polarized light in the x-direction.

1.3 Hydrostatic Pressure in 3D and 2D

Hydrostatic pressure have proved to be a valuable tool for studying the influence of the band structure parameters on the electronic and optical properties of semiconductors, bulk crystals, or two-dimensional systems.[1.6]

Consider a bulk crystal under uniform hydrostatic pressure, and plot the magnitude of the separations (gaps) between the top of the valence band and the conduction band minima, Γ (the principal, lowest minimum), X and L (secondary minima at the Brillouin zone boundaries along the <100> and <111> directions, respectively); we obtain a diagram such as is shown in Fig. 1.4. We can see that the lowest Γ minimum moves rapidly up and the direct gap increases with pressure by about ~ 10 meV/kbar. The secondary X minimum moves down in energy, at a rate of about ~ 1 meV/kbar. This means that the indirect gap between the X conduction band minimum and the top of the valence band (which occurs at the centre of the Brillouin zone at Γ) decreases until it crosses below the direct gap (Γ) value.

It is interesting to note that the behaviour of the band gaps at Γ, X and L illustrated in Fig. 1.4 (i.e., a large positive pressure coefficient for the Γ gap and a small negative one for the indirect X gap) represents a general trend that applies to all diamond and zinc-blende semiconductor crystals. Owing to the pronounced differences of the pressure coefficients related to the Γ, X and L valleys, it is possible to identify the nature of the lowest conduction band states by measuring the pressure coefficients of the photoluminescence energies in quantum wells or superlattices.

The reason that dE_g / dp is negative for the gap between the valence band at Γ to the

conduction band at X is the strong influence of the d levels that lie in energy well above the X minima of the conduction band. These levels repel the conduction band at X, forcing it downward in energy (relative to the minimum at Γ).[1.7]
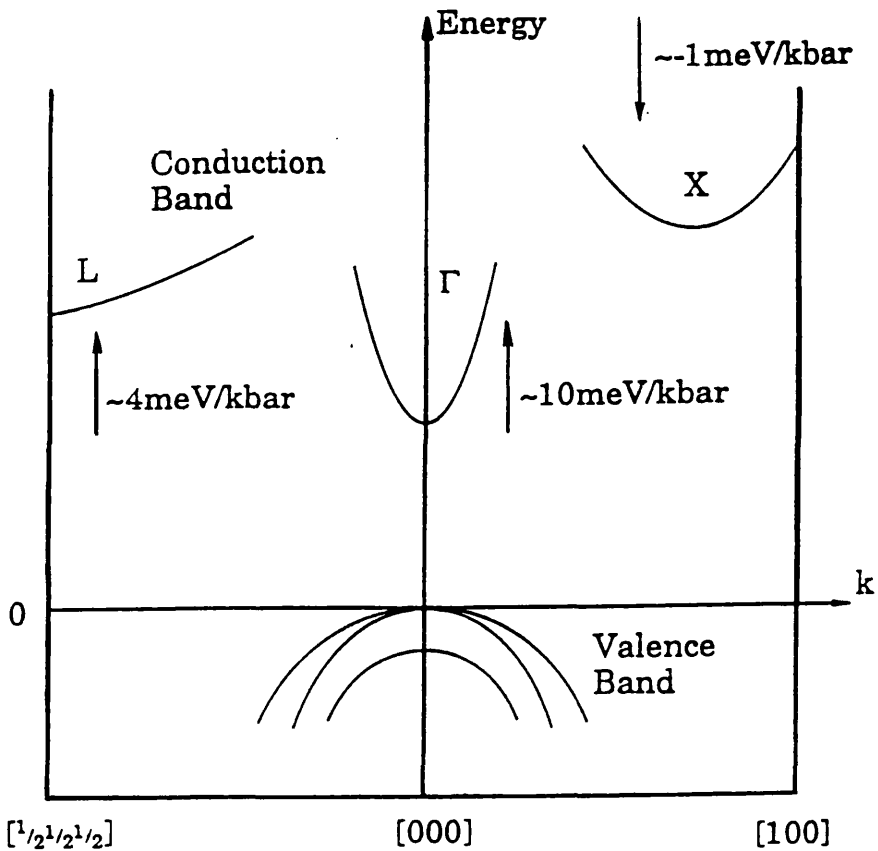
Fig. 1.4. Schematic of the energy bands under hydrostatic pressure for diamond and zinc-blende semiconductor crystals.

In addition, an extrapolation of the pressure dependence of the X-like or Γ-like states to atmospheric pressure will give the value of the energy separation between Γ-like and X-like states at atmospheric pressure. The pressure dependence of the relative

PL intensity will also provide information about the transition probabilities and the state mixing.

As the near band-edge luminescence shifts to higher energies with pressure, an initial pressure coefficient for the band-gap can be derived. With further increasing the pressure, the luminescence quenches around the Γ-X crossover as the optical transitions become dominated by an indirect level. This allows some of the characteristics of the X minima related levels, such as impurity binding energy, to be examined experimentally.

1.3.1 High Pressure Effects in 3D

In general, hydrostatic pressure applied to a semiconductor up to a level below a structural phase transition acts as a perturbation on the electronic properties of the crystal, without destroying the symmetry and removing the symmetry degeneracies of the crystal. The effect of hydrostatic pressure on the electronic and optical properties of zinc blende semiconductors is linked directly to a decrease in the crystal volume and hence a decrease in the lattice constant. Therefore, only band edges which are not required by symmetry to be degenerate may be removed with respect to one another.[1.8] The connection between pressure p and lattice constant a, at a given temperature T, is given by the Murnaghan's equation of state[1.9]

$$- (\Delta a \, / \, a_0)_T = 1 - [\, 1 + (B_0{}' \, / B_0) \, p \,]^{-1 \, / \, (3B_0')}, \qquad (1.5)$$

where B_0 is the isothermal bulk modulus at p = 0 and $B_0{}'$ is the derivative with respect to pressure p. These changes lead to changes in the charge distributions of the covalent bonds and consequently affect all main important parameters, such as principal energy gaps, effective masses and oscillator strengths all of which play a major role in the description of most optical and transport properties of semiconductors.[1.10]

For zinc-blende type crystals, the variation of energy gap with hydrostatic pressure is described by the deformation potential defined as

$$a = dE_g / d(\ln V) = -1/3 \, (C_{11} + 2C_{12}) \, dE_g / dp \, , \qquad (1.7)$$

where C_{11} and C_{12} are the elastic constants [1.11] The variation in energy ΔE_g of an energy band E_g is proportional to the relative variation $\Delta V / V_o$ of the unit-cell volume V_o:

$$\Delta E_g = a \, \Delta V / V_o \, , \qquad (1.8)$$

here the proportionality constant a is the hydrostatic deformation potential associated with the energy band E_g , sometimes called acoustic deformation potential.[1.12] For bulk materials the elastic constants are related to the change in volume by[1.13]

$$\Delta V / V_o = 3 \, p / (C_{11} + 2C_{12}) \, . \qquad (1.9)$$

The change in lattice constant is related to the change in volume by

$$3 \, \Delta a / a_o = \Delta V / V_o \, . \qquad (1.10)$$

Therefore we can write the normalized change in lattice constant as

$$\Delta a / a_o = p / (C_{11} + 2C_{12}) \, . \qquad (1.11)$$

The deformation potential concept was introduced by Bardeen and Shockley[1.14] in the study of the coupling between electrons or holes and acoustic phonons. The electron-phonon coupling constant is the shift in the energy bands due to the local deformation produced by vibrational modes. Their main idea is to assume that the local deformation accompanying a vibration mode is similar to those of a homogeneously

deformed crystal. So, the electron-phonon coupling constants are equivalent to the deformation potentials which are the shifts in the energy bands induced by a macroscopic strain, in the hydrostatic stress which can be associated with long-wavelength longitudinal acoustic phonons.[1.15]

Normally, the luminescence or absorption spectra provide a relative measure of the position of the band-gap, E_g. It is found, in most instances, that as the pressure is increased the band edge varies sub-linearly with pressure and can be fitted to a quadratic equation of the form

$$E_g(p) = E_g(0) + \alpha\, p + \beta\, p^2, \tag{1.12}$$

where α is in meV/kbar, the initial pressure coefficient and β is in meV/kbar^2. The sublinear pressure dependence of $E_g(p)$ is accounted for by the non-linearity of the equation of the state. A plot of $E_g(p)$ against pressure, assuming that a linear relationship exists with the lattice constant, gives a gradient corresponding to the deformation potential:

$$E_g(p) = E_g(0) + 3\, a\, (\Delta a / a_0) \tag{1.13}$$

where a is the deformation potential. However, this analysis only applies for bulk samples grown as single crystals. A thin, lattice matched or mismatched, epitaxial layer grown onto a substrate of different bulk modulus produces further complications.

It was only recently that the problem of studying thin epitaxial layers under hydro-static pressure was first considered.[1.16] Ferguson et al[1.17] presented the first high pressure optical data obtained for $Al_{0.48}In_{0.52}As$ grown lattice matched onto a InP substrate. From their data, an initial pressure coefficient for the $Al_{0.48}In_{0.52}As$ was obtained, a deformation potential for the band edge was calculated and the pressure dependence of the effective mass using k.p theory was derived.

1.3.2 High Pressure Effects in 2D

Heterojunctions are basic building units of semiconductor microstructures. In particular, the key parameter on which much of the physics of low-dimensional structures rests is the heterojunction band offset. The magnitude of the band offset depends on the relative position of the band edges of the constituent materials with respect to each other. Since the sum of band offsets is a constant given by the difference in bulk energy gaps, it is customary to quote the ratio of the conduction to the valence band offset, $\Delta E_c / \Delta E_v$.

In order to determine the position of confined levels, and consequently the band gap of a micro-structure together with the degree of penetration of electron wave functions into the barrier, an accurate value of the band offset is required. The problem of the band offset in LDS has been recently solved by an experimental solution, namely using a pressure induced Γ-X crossover.[1.18]

As shown in Fig.1.5, when the pressure $p < p_c$, the Γ conduction band of GaAs is lowest in energy, and E^Γ_{1h} is the dominant emission in this type-I superlattice (the lowest-lying conduction- and valence-band minima are both in the same layers of the superlattice). Because of the pronounced differences of the pressure coefficients related to the Γ, X and L bands, the pressure causes a decrease in the indirect gap of the AlGaAs, and an increase in the confined Γ-related state in the GaAs. With sufficient pressure $p > p_c$, the confined state in the GaAs is pushed above the X minima in the AlGaAs, which now become the lowest-lying conduction band minima in this quantum system. Hence, the application of hydrostatic pressure produces a type-II configuration (the lowest-lying conduction- and valence-band minima are on opposite sides of the

superlattice).[1.19]
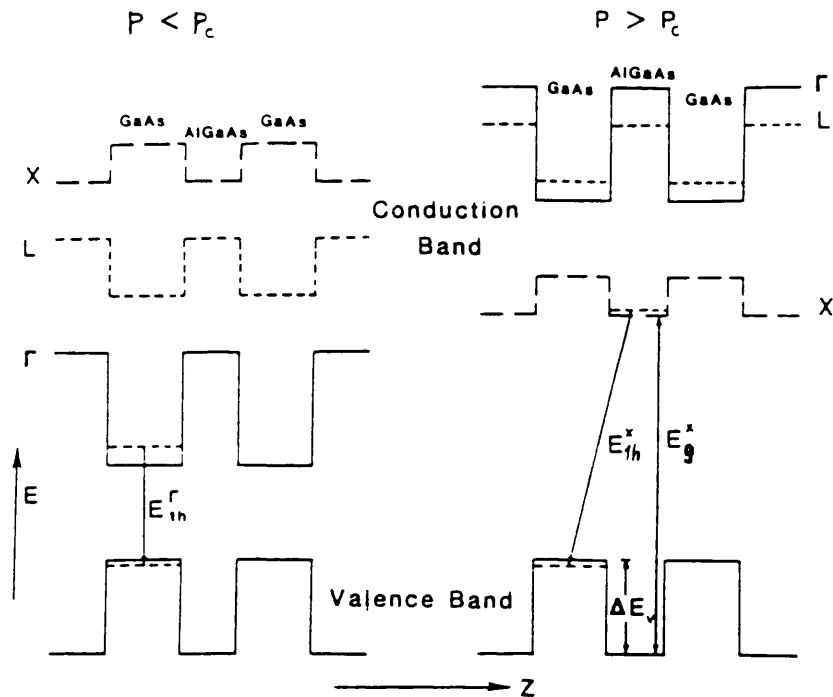
Fig. 1.5. Schematic band diagram in GaAs/AlGaAs heterostructure before (type-I) and

after (type-II) the $\Gamma-X$ crossover.

Beyond the $\Gamma-X$ crossover, the electrons and holes are spacially separated and

recombination takes place across the heterointerface. This staggered transition is

denoted as E^X_{1h} in Fig. 1.5. The valence band offset can be written as,

$$\Delta E_v = E_g^X - E^X_{1h} + h, \qquad (1.14)$$

where E_g^X is the indirect band gap of AlGaAs, E^X_{1h} is the observed transition energy

and h is the confinement energy of the carriers in the wells. Because of the large

effective masses of electrons in the X conduction band and heavy holes, h is small.

Hence, a knowledge of E_g^X and E^X_{1h} would enable one to determine ΔE_v .

The behaviour of QW's and SL's under HP is rather complicated since several effects have to be considered:[1.20]

(a) The well width (L_z) diminishes with pressure. This results in a rise in energy for the conduction (valence) band levels and, as a consequence, an increase in the transition energy between the ground states. The pressure dependence of the L_z with pressure is taken from the elasticity theory:

$$L_z \, (p) = L_z \, (0) \, [1 - p / (C_{11} + 2C_{12})] , \qquad (1.15)$$

where p is the magnitude of the external pressure, which is possitive for a compression; C_{11} and C_{12} are the elastic constants of well layers.

(b) Both barrier and well layers exhibit different pressure coefficients. Therefore, applying pressure will change the band offsets. This will vary the confinement energies of the carriers in the well layers.

(c) The size quantization and the change of the gaps with the pressure lead to an increase of the effective masses in the well and in the barriers. This change partly counteracts the changes due to the decrease in L_z.[1.21]

In analogy to the case of bulk materials, the luminescence intensity of E^Γ decreases rapidly with increasing pressure. This decrease is induced by the change of the relative position of Γ-like states with respect to X-like states and, hence, the transfer of electrons from Γ-like states to X-like ones. The intensity I^Γ can be expressed as follows[1.19]

$$I = I_0 \, \{1 + A \exp [(\alpha^\Gamma - \alpha^X) \, (p - p_c) / k_B T]\}^{-1} , \qquad (1.16)$$

where I_0 and A are constants, α^Γ and α^X are the pressure coefficients of E^Γ and E^X,

respectively. p_c is the crossover pressure at which $E^\Gamma - E^X = 0$, determined from the intersection point of E^Γ against p and E^X against p curves. p_c is mainly governed by the difference in the subband energies $E^\Gamma_{1h} - E^X_{1h}$. Neglecting small effects such as the changes due to pressure upon the confinement energies in the X conduction band and the binding energies of the excitons (small compared to E^Γ_{1h}), p_c is given by[1.23]

$$p_c = [\, E^X_{1h} - E^\Gamma_{1h} \,(p = 0)] \,/\, (\,\alpha^\Gamma - \alpha^X\,) \,, \qquad (1.17)$$

$$E^\Gamma_{1h} \,(p) = E^\Gamma_{1h} \,(0) + \alpha^\Gamma \, p \,, \qquad (1.18)$$

$$E^X_{1h} \,(p) = E^X_{1h} \,(0) + \alpha^\Gamma \, p \,, \qquad (1.19)$$

In the absence of Γ-X mixing, the transition from the X-like state to the highest valence state at the Γ point is forbidden. The effect of Γ-X mixing is equivalent to turning a forbidden transition into a partially allowed one and the luminescence intensity is tunable over many orders of magnitude around p_c. The observed spectra are a very sensitive probe of Γ-X mixing. Since the effective mass at the X point is much larger than that at Γ, the emitting exciton is highly localized at the interface. This provides a unique opportunity to study the interface quality on the scale of atomic separations.[1.24]

To summarize, photoluminescence measurements under hydrostatic pressure provide an effective way to investigate the band structures and optical properties of LDS. The nature of conduction band states responsible for the luminescence transitions can be derived from their pressure dependence without ambiguity. The energy separation between Γ-like and X-like states is determined independent of the relative position of these levels with respect to each other.

1.4 Effect of Strain on Energy Band Structure

With the advent of modern epitaxial growth techniques such as Molecular Beam Epitaxy (MBE) and Metal-organic Vapor Phase Epitaxy (MOVPE), it has become possible to grow semiconductor superlattices and quantum well structures tailoring their band structures to achieve the desired electronic properties and device applications. Strained-layer superlattices (SLS) give an additional degree of freedom by enabling hetero-epitaxial growth of lattice-mismatched systems without creating dislocations.[1.25]

Nature knows two answers to accommodate lattice mismatched films, namely elastic accommodation by strain and plastic accommodation by misfit dislocations lying in the interface (see Fig. 1.6). Nature seems to prefer elastic accommodation for a thin film up to a critical thickness. The strain energy in these structures is taken up by the elastic deformation of the lattice. All of the lattice mismatch is accommodated by the strains in the layer without the generation of misfit dislocations as long as the individual layers are kept below their critical thickness. Above the critical thickness misfit dislocations are generated relaxing the built-in strain.
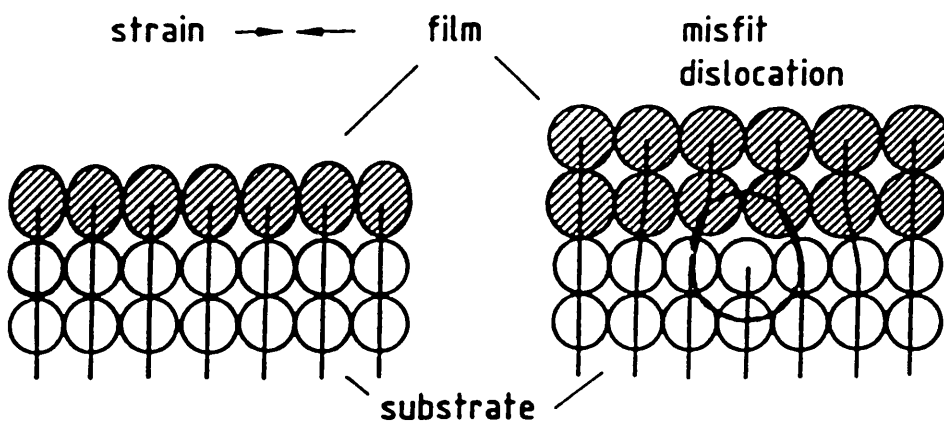
Fig. 1.6. Mismatch accommodation by strain (left) or misfit dislocations (right).

1.4.1 Strains due to Lattice Mismatch

In strained-layer semiconductors, the biaxial strain in a plane is equivalent to applying a hydrostatic pressure plus a uniaxial strain along the growth direction (see Fig. 1.7). A hydrostatic pressure will shift the energy band gap of a semiconductor. However, the general effect of a uniaxial strain on the band structure is to split the degeneracies of any equivalent valleys which are not symmetric with the direction of the applied stress.[1.26]

| **Biaxial Compression** | **Hydrostatic Pressure** | **Uniaxial Stress** |

| **Tetragonal Distortion** | **Energy Shifts** | **Energy Splittings** |
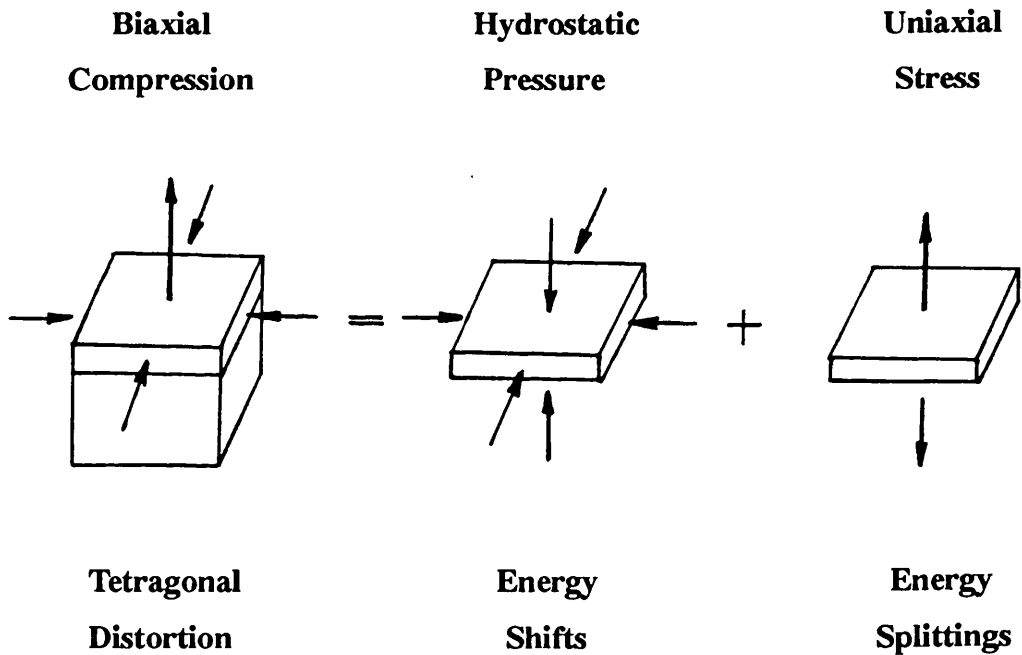
Fig. 1.7. Schematic of biaxial strain.

For the case of a free standing strained-layer superlattice (SLS), the equilibrium in-plane strained lattice constant $a_{//}$ of the SLS is given by[1.27]

$$a_{//} = a_A \left(1 - f\, G_B L_B / (G_A L_A + G_B L_B) \right) , \qquad (1.20)$$

where $L_{A, B}$ are the layer thicknesses and $a_{A, B}$ are the lattice constants. f is lattice mismatch of layer A with respect to layer B, given by

$$f = (a_A - a_B) / a_A ,$$

(1.21)

G_A and G_B are shear moduli given by

$$G_{A, B} = 2 \left[C_{11}^{A, B} + C_{12}^{A, B} - 2 (C_{12}^{A, B})^2 / C_{11}^{A, B} \right] .$$

(1.22)

$C_{ij}^{A, B}$ are the elastic constants of layers A and B, respectively.

The built-in strains in layer A due to the lattice mismatch are characterized by

$$\varepsilon = \varepsilon_{xx} = \varepsilon_{yy} = (a_{//} - a_A) / a_A ,$$

$$\varepsilon_{zz} = - 2 \varepsilon_{xx} (C_{12} / C_{11}) ,$$

(1.23)

$$\varepsilon_{xy} = \varepsilon_{yz} = \varepsilon_{zx} = 0 .$$

The direction of growth of the epilayer is taken as the z axis and $\varepsilon = \varepsilon_{xx} = \varepsilon_{yy}$ is referred to as the biaxial strain.

The effects of biaxial strain on the direct ($k = 0$) band of zinc-blende semiconductors are as follows.[1.28, 1.29] In the absence of strain, the maxima of the heavy- and light-hole valence bands are degenerate with the fundamental gap designated E_g as in Fig. 1.8. The biaxial strain shifts and splits the heavy- and light-hole bands, which can be expressed by[1.31]

$$\Delta E_{hh} = [- 2 a (C_{11} - C_{12}) / C_{11} + b (C_{11} + 2 C_{12}) / C_{11}] \varepsilon,$$

(1.24. a)

$$\Delta E_{lh} = [- 2 a (C_{11} - C_{12}) / C_{11} - b (C_{11} + 2 C_{12}) / C_{11}] \varepsilon,$$

(1.24. b)

here a is the combined hydrostatic deformation potential for transitons between the conduction and valence bands, b is the shear deformation potential constant characterizing the splitting of the Γ_8 valence band for tension or compression along [001].
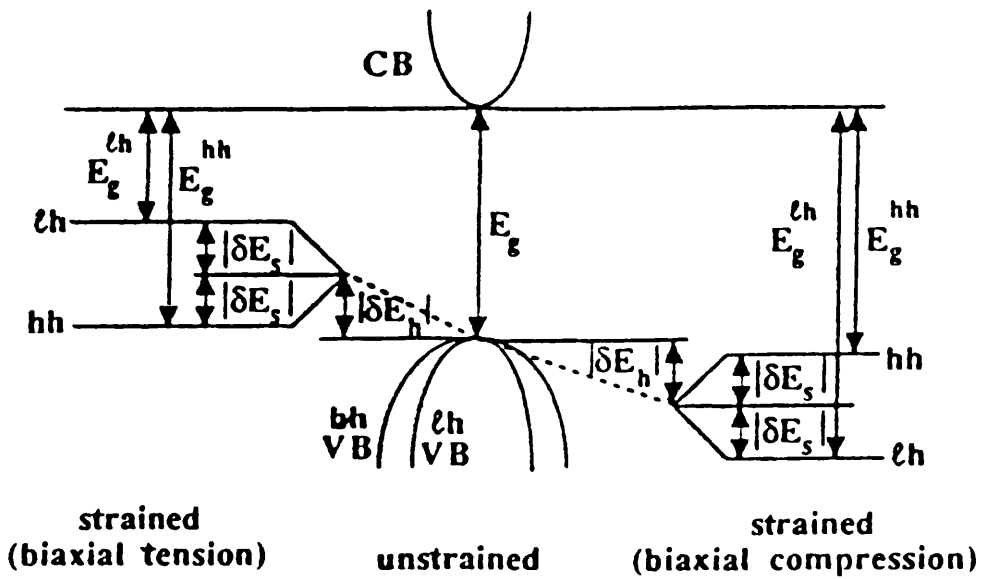
Fig. 1.8. The Γ_6 conduction band minimum and the Γ_8 valence band maximum in a zinc-blende semiconductor under a biaxial strain (After Rockwell et al, 1991).[1.30]

If layer A has a lattice constant larger than that of layer B, the biaxial strain is compressive and a corresponding band gap expansion occurs with the heavy-hole-derived band gap. Note that ε is defined as negative for biaxial compressive strain. In contrast, for biaxial tension, the fundamental gap shrinks and is light-hole related.[1.30] Note also that the direct conduction band minimum at Γ_6 is non-degenerate and therefore only subject to the hydrostatic component of the strain, and not influenced by uniaxial component.[1.32]

1.4.2 Strains due to Applied Pressure

Hydrostatic pressure decreases the lattice constants of a material. Since the compressibilities of different semiconductors vary, there can be pressure-induced biaxial strains between semiconductors that share a common interface. Fig. 1.9 depicts the strain field inside a two-component [001]-oriented SLS under hydrostatic pressure p.
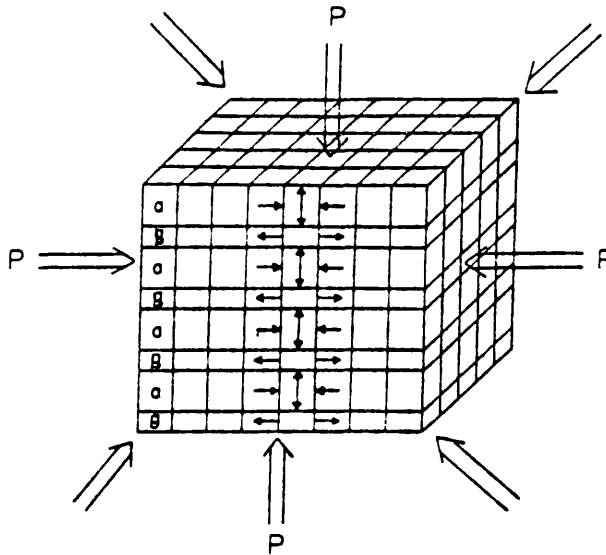
Fig. 1.9. Two-component SLS under hydrostatic pressure p showing tetragonal internal strain.

This strain field as a function of pressure p is given by[1.30]

$$\varepsilon (p) = p \left[(C_{11} + 2\,C_{12})_A^{-1} - (C_{11} + 2\,C_{12})_B^{-1} \right], \qquad (1.25)$$

where ε (p) is the pressure induced strain, p is the applied hydrostatic pressure, and the C_{ij}'s are the elastic constants for the layers A and B. The total strain on a strained layer under pressure is the sum of the strain induced by the initial lattice mismatch and that from Eq. (1.25). If the compressibility of layer A is less than that of layer B, then the strain in Eq. (1.25) is negative and hence biaxially compressive. On the other hand, if the compressibility is greater, there will be a pressure dependent biaxial tensile strain.

1.5 Photoluminescence in 3D and 2D Systems

1.5.1 Basic Features of Photoluminescence in 3D

The optical characterization of semiconductors is particularly important as it allows observation of fundamental material properties and provides a critical assessment of material quality.

Photoluminescence (PL) is the most widely used technique[1.33] due to the ease of its implementation. Luminescence occurs as the result of the creation of elementary excitations in the crystal, their thermalization in free and bound states, and their radiative recombination. The observed emission is thus the result of a complex cascade of events and represents a more or less complete thermalization of excitations into some energy-distributed radiative states.[1.5]

PL has proved a valuable technique in the studies of semiconductor electronic levels, such as band-edge determination and impurity identification at very low concentrations that cannot easily be probed by other methods. It is important for the growth and further purification of materials in that substitutional donor and acceptor impurities can be identified. Further experimental refinements to PL, selective excitation techniques and the application of perturbations, for example, electric or magnetic fields, or the use of pressure or strain, enhances the data obtained.

All the semiconductors studied in this work have the zinc-blende structure. It consists of two face-centred cubic (fcc) lattices, the point lattice group, displaced by one quarter of a body diagonal[1.34] (Fig. 1. 10). When considering a III-V compound such as GaAs; the Ga atoms will be placed on one fcc latice and As atoms on the other fcc lattice. The diamond structure is similar but the atoms are of the same chemical type on each fcc lattice. Each atom has four equally distant atoms arranged in the form of a

regular tetrahedron as a result of directional covalent bonding. The diamond structure possesses a centre of inversion symmetry at the midpoint of each line connecting nearest neighbour atoms. The zinc-blende structure does not have this inversion symmetry due to the differing atoms.
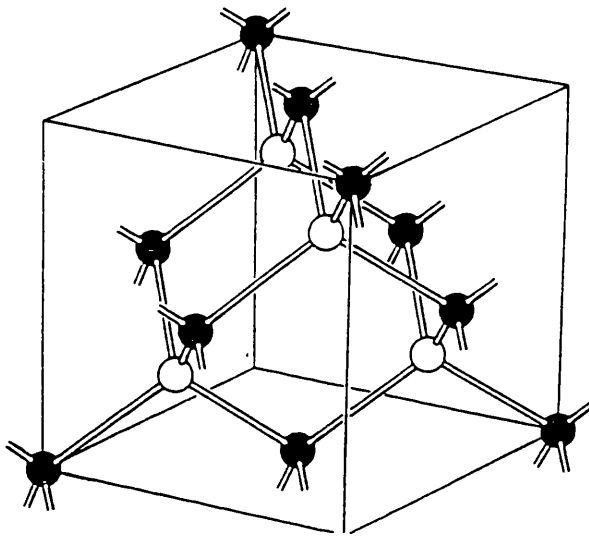
Fig. 1.10   In zinc-blende structure the different atoms (e.g. Ga and As) are on inter-penetrating face-centred cubic lattices. Diamond is similar but both atoms are chemically the same. Note the tetrahedral arrangement of bonds (After Elliot and Gibson 1982).[1.34]

Fig. 1.11. shows the possible optical transitions in 3D semiconductors,[1.35] which are excitonic, free-to-bound, donor-acceptor-pair and phonon assisted transitions. The symbols used for labeling optical transitions are shown in table 1.1. Even though non-radiative transitions are not directly detected in the luminescence they are important because they compete with the radiative transitions, thus altering the emission intensity and time dependence.
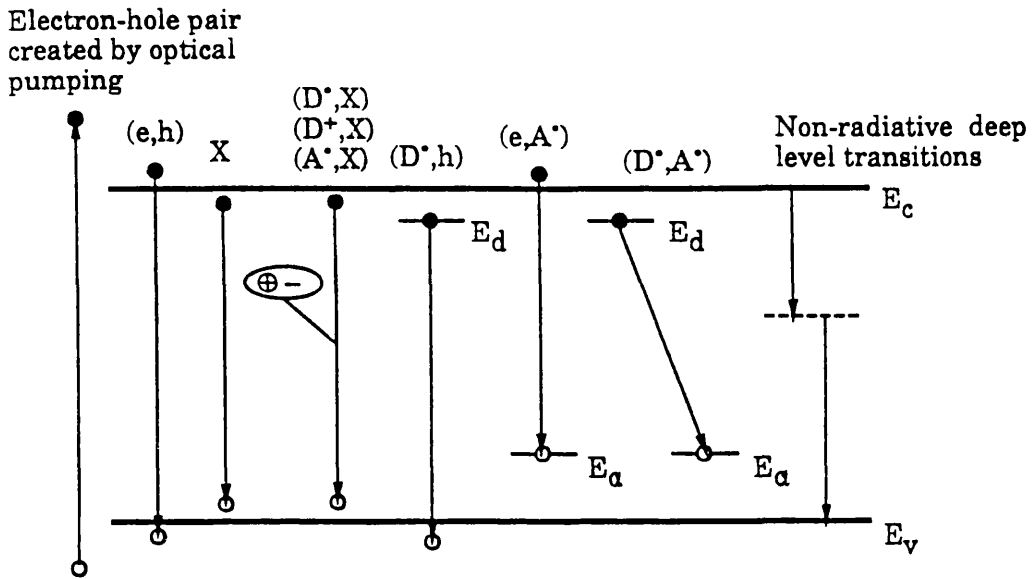
Fig. 1.11. Idealized band edge diagram showing possible optical transitions (After

Cavenett 1978).[1.35]

Table 1.1 Symbols used for labeling optical transitions (After Cavenett, 1978)[1.35].

(e,h)	Conduction band to valence band
X	Free exciton
(D*,X)	Neutral Donor bound exciton
(D+,X)	Exciton bound at an ionized donor, transition intensity increases with temperature due to thermal ionization of donors.
(A*,X)$_j$	Shallow Acceptor bound exciton, on recombination the exciton may leave the acceptor in a excited state where its total angular momentum quantum number j=0.5, 1.5, 2.5
(D*,h)	Neutral Donor to free hole
(e,A*)	Free electron to neutral acceptor
(D*,A*)	Donor acceptor pair

Emission from the conduction band to valence band (e, h) is normally only observed in degenerately doped semiconductors as a result of tail states.[1.36] Although free exciton recombination (X) can be seen in high purity GaAs and InP, it has never been shown to dominate the spectra in 3D semiconductors.[1.37] The reason for this is that the exciton trapping processes are often very efficient at impurities; the free exciton is less thermally stable and is subject to a surface recombination. Therefore, the luminescence spectra from even the purest semiconductors are dominated by impurity related transitions. There exists a vast literature on impurity related spectroscopy,[1.38] and the importance of understanding such impurity and defect systems has led to very significant advances in spectroscopic techniques.

Under certain circumstances, the binding energy of an exciton is increased by the presence of a point defect, say, a neutral or ionized impurity. Energy is the fundamental criterion that determines whether or not an exciton can be trapped by an impurity. If the total energy of the system is reduced (corresponding to an increase in the binding energy of the exciton) when the exciton is in the vicinity of an impurity, then it is energetically favorable for the exciton to remain near the defect; the exciton becomes "bound" to the impurity. Obviously, if the energy of the system is increased when the exciton is near the defect, the exciton will choose to remain free.[1.33]

The temperature and excitation density dependences of an excitonic emission can give further evidence on what the transition can be related to. For an exciton bound at an ionized donor, the transition intensity increases with temperature due to thermal ionization of donors. If the emission were impurity related it would saturate when the density of incident photons exceeds the density of impurities. Since the formation of excitons is proportional to the product of the two photocreated populations in the bands, the exciton emission intensity should increase quadratically with excitation density.

Free-to-bound or donor-acceptor-pair transitions are non-excitonic, and occur at lower energies than the excitonic emissions. When an electron (which is loosely bound on a donor) combines with a hole in the valence band, donor-to-free hole (D^O, h); or a hole (which is loosely bound on an acceptor) combines with an electron in the conduction band, free electron-to-acceptor (e, A^O), a free-to-bound transition occurs. The donor-acceptor-pair transition, (D^O, A^O), occurs between a neutral donor and a neutral acceptor leaving the impurities partially ionized.

1.5.2 Basic Features of Photoluminescence in QWs

In low dimensional structures, it well known that the most evident and ubiquitous effect of QWs light emissions is the much larger quantum efficiency compared to the 3D case reported in all material systems studied up to now[1.5]: GaAs/AlGaAs, GaInAs/AlInAs, GaInAs/InP, CdTe/CdMnTe, ZnSe/ZnMnSe, etc. The enhanced radiative efficiency in QWs has been attributed to the larger exciton binding energy, the increased electron-hole overlap and gettering of non-radiative impurities at interfaces.

At low temperatures, the intrinsic free exciton recombination dominates the optical spectra, and extrinsic recombination processes involving impurities (electron to neutral acceptor recombination, bound excitons etc.) only appear in QWs at significantly higher impurity concentrations than those in 3D. This may be due to the more efficient intrinsic radiative recombination mechanisms or inefficient 2D impurity capture mechanism.[1.5]

It is also well proven that in most material systems QWs are optically very bright; carrier collection into a QW can be very efficient. The well usually robs the surrounding barrier material of photo-generated carriers to the extent that it may be difficult to observe PL from the barrier material of a MQW stack, even when the volume of the barrier material may be orders of magnitude greater than that of the QWs.

Proof that the main emission in QWs was due to free excitons was obtained from the quasi-coincidence of PL and PLE spectra but particularly from circularly polarization experiments[1.39] (see Fig. 1.12).

PHOTON ENERGY (eV)   SELECTION RULES

(a)   (b)
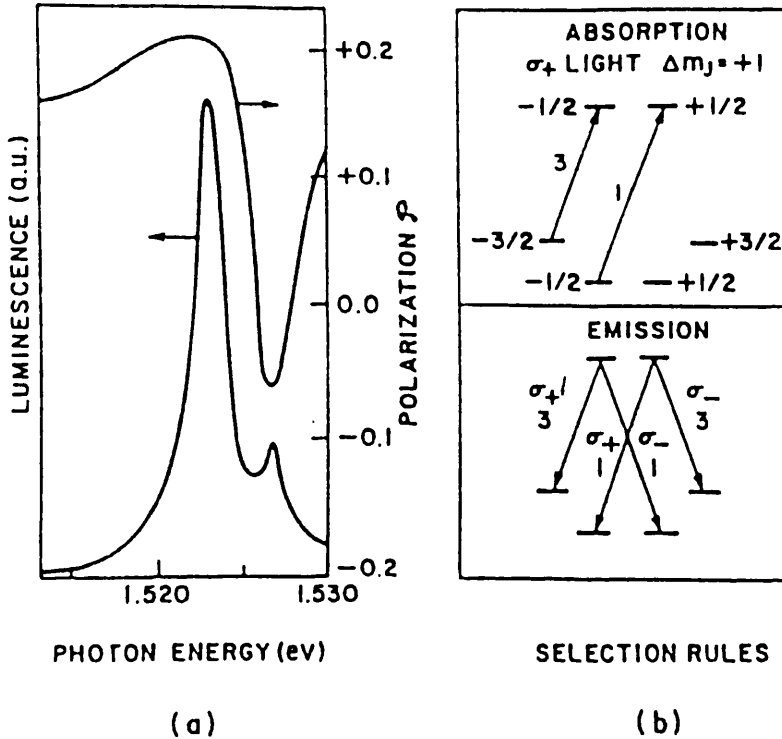
Fig. 1.12. a) Photoluminescence and its circular polarization at 50 K for excitation at 1.65 eV with circular polarized light. The sample has 25 GaAs wells (L_w = 188 Å) and $Al_xGa_{1-x}As$ barriers (L_b = 19 Å, x = 0.3). For this nonresonant excitation, m_j = $-1/2$ electrons are preferentially created which leads to heavy and light hole exciton emission with positive and negative polarizations, respectively.

b) Absorption and emission transitions for GaAs QWs with circular polarized light. The transitions involving heavy (m_j = $\pm$ 3/2) and light (m_j = $\pm$ 1/2) holes have relative strength of 3 and 1, respectively (After Miller and Kleinman, 1985).[1.39]

The emphasis for a theoretical description of the properties of QW structures has been made within the framework of the envelope function approximation.[1.40] The exciton energy level is given by:[1.5]

$$E_x = E_g + E^e_{Conf.} + E^h_{Conf.} - E_B , \qquad (1.26)$$

$$E_B = m_r^* e^4 / (2 h^2 \varepsilon^2 n^2) , \quad n \geq 1 , \qquad (1.27)$$

$$1 / m_r^* = 1 / m_e^* + 1 / m_h^* . $$

where E_B is the exciton binding energy and $E^e_{Conf.}$ and $E^h_{Conf.}$ are the confining energies for electrons and holes. For an infinite square well of width L_z, $E^e_{Conf.}$ and $E^h_{Conf.}$ are given by

$$E^{e(h)}_{Conf.} = (h\,n)^2 / (8\,m_{e(h)}^* L_z^2) , \quad n \geq 1 . \qquad (1.28)$$

The determination of $E^e_{Conf.} + E^h_{Conf.}$ through Eq. (1.26) has been widely used to assess band offsets of hetero-structures. Exciton binding energies have been determined from the distance between n = 1 and n = 2 absorption peaks[1.39] or from PLE measurements in magnetic fields.[1.41]

The sharpness and intensity of the exciton luminescence is a measure of the sample quality, as in bulk crystals. One of the key uses of PL has been the characterization of the abruptness of the interface systems. The basic concept is that since the confinement energy of the electron subband is a sensitive function of the well thickness, then the recombination energy of an exciton reflects the average thickness of the well, or at least that of the region of the well where the recombination event occurs. Thus the overall

- 33 -

line-width, representing the convolution of all possible transitions, must reflect the width fluctuations.

PL line-width from QWs depends strongly on both QW width and on the characteristic size of the fluctuations. For the case of GaAs QWs, alloy broadening of the PL line-width is often not an issue, because the wave functions are largely confined to the binary material. However, since the barriers are not infinite, the exciton wave functions do penetrate into the barrier, and the penetration is most severe for narrow wells. For the other material systems in which the barriers are binary and the wells ternary, the effect of alloy broadening may be more apparent.[1.42]

Ch. 2.   EXPERIMENTAL APPROACHES

2.1.   PL and PLE Spectroscopy Measurements

2.1.1.   Introduction

Semiconductors are transparent to light of energy less than the energy gap sepa-
rating the conduction band from the valence band. The energy at which the semicon-
ductor starts to absorb light is known as the band edge. In an experiment, the creation
of excitons can be achieved by shining a laser beam of energy higher than the band gap
onto the material. The electrons lifted into the conduction band by the beam rapidly
relax to the bottom of the band, losing their kinetic energy in collisions with lattice
vibrational waves (emitting phonons). This process is very fast (of the order of
picoseconds). Once at the bottom of the band, electrons find holes and form excitonic
states that collapse after a lifetime of about a few nanoseconds: in the process of exciton
annihilation, the electron emits a photon and jumps into the empty state in the valence
band thus annihilating the hole. This constitutes the photoluminescence (PL) signal. In
fact the detailed sequence of events can be extremely complicated. The PL spectrum is a
measure of the number of photons emitted from a structure at energy below E_g.

The PL from a QW system contrasts sharply with that obtained from similar purity
bulk material in that the intrinsic free-exciton recombination dominates the spectrum at
low temperatures where impurity related processes normally dominate that of bulk
material. The enhanced radiative efficiency in QWs has been attributed to the larger
exciton binding energy, the increased electron-hole overlap and gettering of non-
radiative impurities at interfaces. Most PL experiments are performed at liquid helium
temperature in order to narrow line-widths and to prevent the thermal quenching of
spectral features. The use of low temperatures enhances the importance of excitons in
the optical spectra, since in most semiconductors excitons are relatively stable thermally
below 5 K.

However, the PL emission really only gives information on the ground state, the

lowest energy e1-h1 transition in a QWs system. This is unfortunate because the higher states are more sensitive to phenomena like width fluctuations and so a knowledge of the position of these states is, in principle, extremely useful for characterising QWs. This failing has been in large part overcome by the use of photoluminescence excitation spectroscopy (PLE). PLE is a measure of the luminescence efficiency as a function of the pump energy (see Fig.2.1). Unlike the PL spectrum it gives information on the higher energy transitions, if a QWs is excited with light of energy sufficient to excite the higher energy transitions. In the conventional form, a tunable laser is used to excite sequentially through the absorption bands of a QW, by tuning the laser line from energy lower than that of the main PL emission upwards; these higher energy transitions can be measured as the excitons relax, emitting phonons, to the n = 1 level.
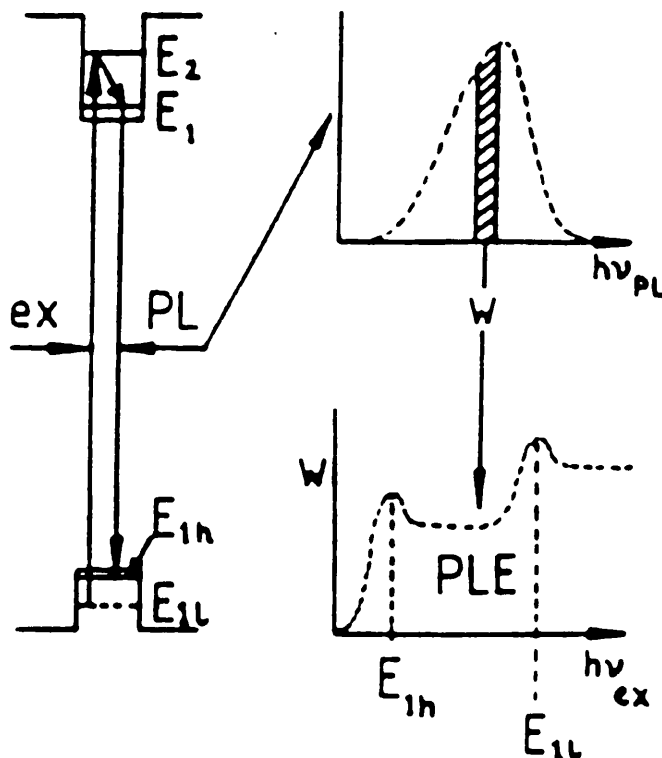
Fig. 2.1. Schematic diagram of the PL and the PLE methods.

Although the luminescence is observed from the ground state transition, when the laser energy is resonant with an exciton level, the usual resonance feature observed in

absorption is detected in the PL emission. In fact the PLE is another example of resonant excitation and fundamentally gives the absorption spectrum, replicated in the strength of the PL. The PLE technique, therefore, provides a much more complete characterization of the low dimensional systems.

This project involved using a high resolution, low temperature, high pressure and strong magnetic field luminescence system, the diagram is shown in Fig. 2.2.
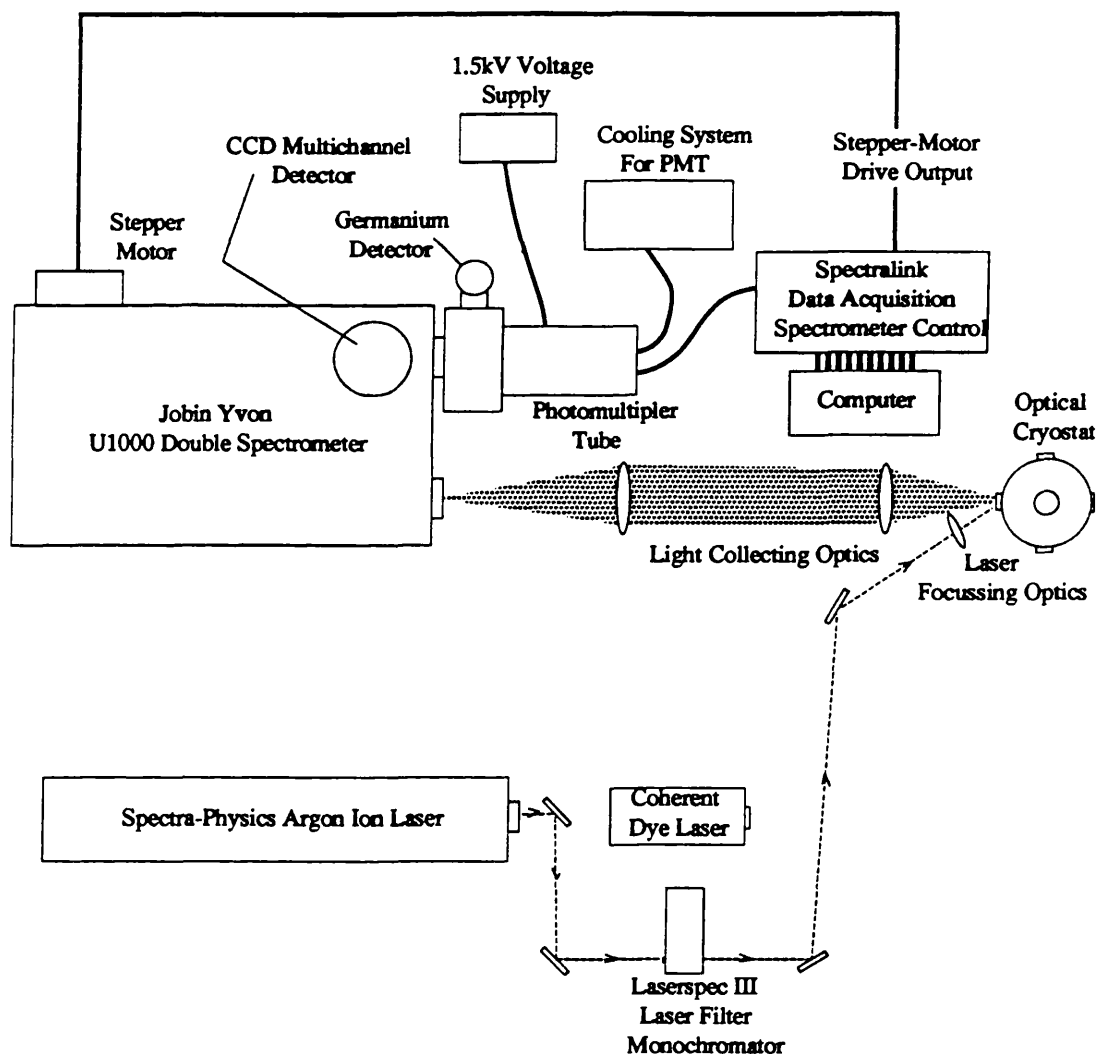
Fig. 2.2.   Schematic diagram of the experimental apparatus used for the PL and the PLE measurements (After Rodden, 1992).[2.1]

Low temperature measurements required the sample to be placed in the cryostat and cooled. A laser was used to photocreate electron-hole pairs and obtain the luminescence spectrum. The emitted radiation was dispersed by a spectrometer and then detected using a photomultiplier tube and standard photon counting techniques. In order to remove plasma lines from a laser beam, a filter monochromator was used. A large bore optical cryostat and a superconducting magnet were used to accommodate two diamond anvil cells (DAC) for high pressure and magneto-optical measurements. Because any sample inside the DAC is very thin (about 100 μm by 100 μm), it is difficult to align the laser beam exactly on the sample. Therefore, an imaging system, consisting of a CCD camera, a television and a reflecting mirror, was used to make alignment easy.

2.1.2. Lasers

The Spectra-Physics model 2045 Argon ion laser was used either directly or as a pump for a dye laser to excite the sample to produce the photoluminescence spectra. The Spectra-Physics model 2045 Argon ion laser was provided with optics allowing single line operation in the visible and UV. Typical powers available in single line operation are given in Table 2.1.

Table 2.1 Output power available from the Spectra-Physics model 2045 Argon ion laser operating in single longitudinal mode.[2.2]

Wavelength	Power	Wavelength	Power
4545 Å	480 mW	4880 Å	9.0 W
4579 Å	1.6 W	4965 Å	3.4 W
4658 Å	850 mW	5017 Å	1.8 W
4727 Å	1.4 W	5145 Å	8.9 W
4765 Å	3.3 W	5287 Å	1.1 W

The dye laser is the Coherent CR-599 and can be used in conjection with DCM (610 -720 nm), Styryl 9 (780-900 nm), Pyridin 1 (670-780 nm) and other dyes depending on the laser optics. By correct choice of the lasing wavelength PLE experiments can be performed for some samples. Fig. 2.3 shows the Coherent CR-599 dye laser optical schematic.
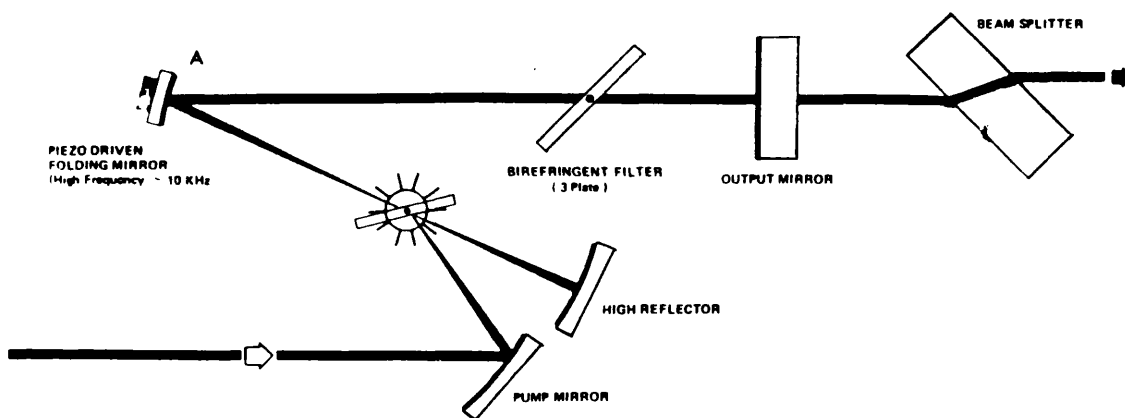
Fig. 2.3 The Coherent CR-599 dye laser optical schematic.[2.3]

2.1.3 Laser Filter Monochromator

The laser filter prism monochromator ensures only single line excitation of the sample and is important for removing the Argon laser plasma background when using the photon counting system. The prism monochromator used here allows the monochromator to operate with a transmission of over 75 % and an almost flat spectral response from 350 nm to 900 nm.[2.4] However, the transmission depended on the beam size and so a transmission of around 50 % was usual. A diagram illustrating the light path through the filter monochromator is shown in Fig. 2.4.

Input
Unfiltered laser light.

Prism to reflect light by
total internal reflection.

Prism to disperse light.
The light makes two
passes through this prism.

Lens

Prism

Slit

Output
Filtered laser light.

Lens

Rotate to change
transmitted wavelength.

Reflector
To return light through
the prism a second time.
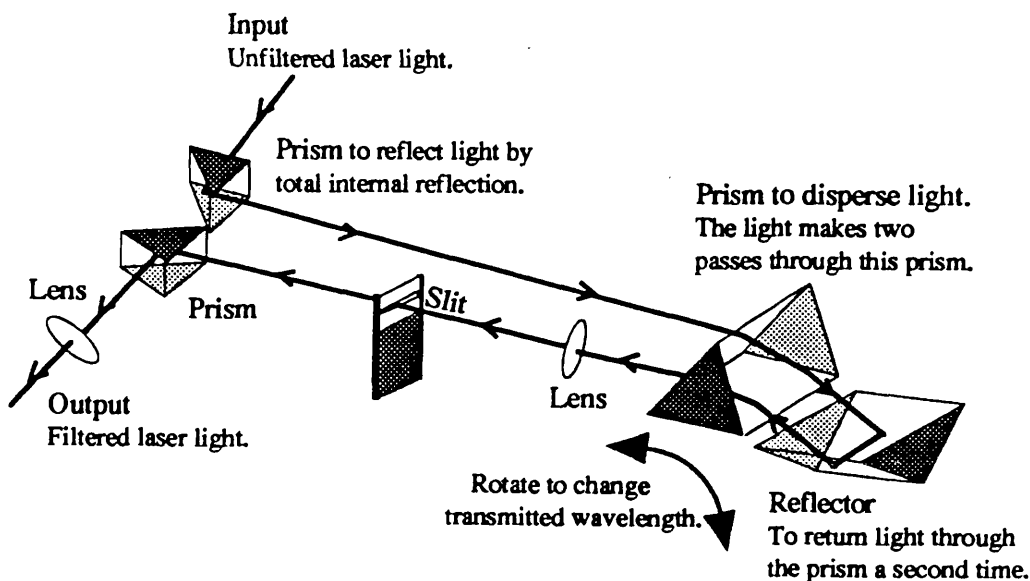
Fig. 2.4   Schematic diagram of light path through "Laserspec III" filter

monochromator (After Rodden, 1992).[2.1]

2.1.4   Spectrometer

The spectrometer used was a Jobin Yvon Ramanor U1000. This is a one metre focal length double grating spectrometer, i.e., two single spectrometers side by side with the gratings attached to a single shaft to eliminate any relative movement. The image of the exit slit of the first spectrometer falls upon the entrance slit of the second spectrometer; the light path is shown in Fig. 2.5. The gratings are coupled additively in that the second grating further disperses the light incident upon it.[2.5]

This spectrometer utilises two gratings covering two different spectral regions. For the work presented here two 1800 grooves/mm gratings were used, which are holographic gratings and efficient throughout the visible region of the spectrum, with dispersion in the range between 0.45 and 0.8 μm. The grating efficiency as a function of wavelength is shown in fig. 2.6.
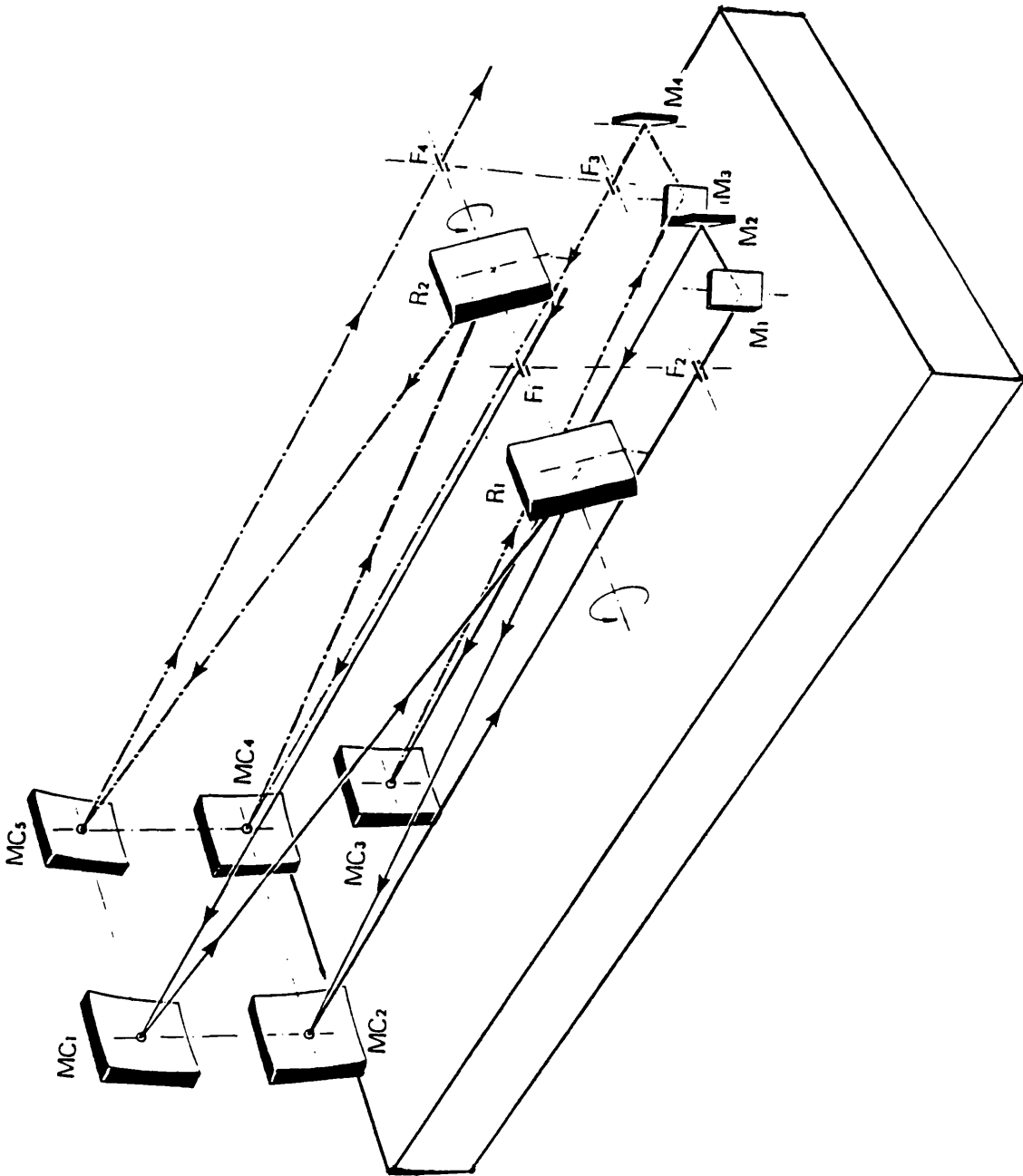
Fig. 2.5   Schematic representation of the light path within the double spectrometer.[2.5]
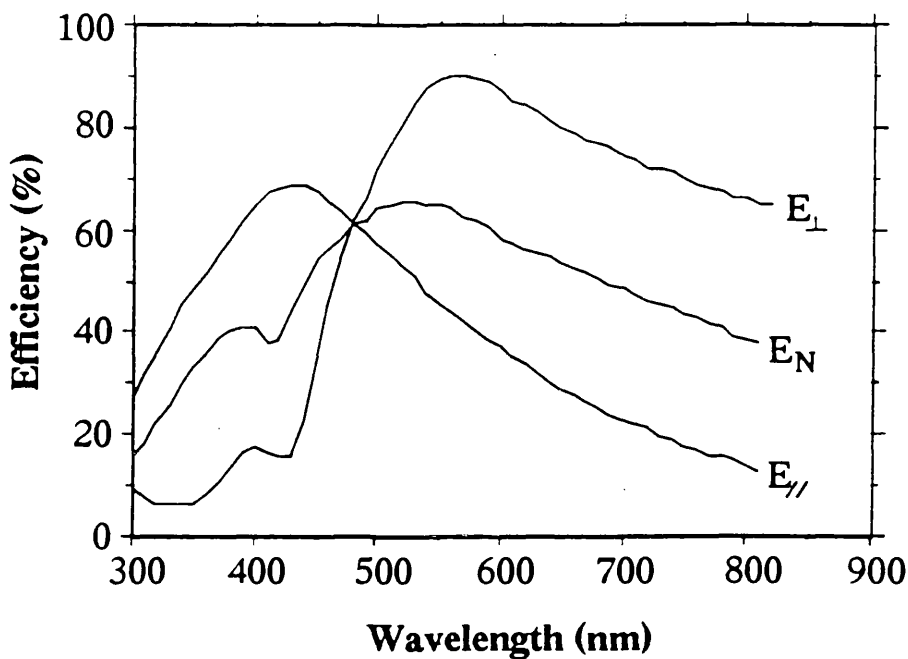
Fig. 2.6. Grating efficiency curves for the visible gratings (1800 grooves / mm gratings) for light polarized parallel to the grooves, perpendicular to the grooves and for the unpolarized light ($E_{//}$, $E_{\perp}$ and E_N respectively).

The spectrometer, with these gratings, provides a reciprocal dispersion of 0.243 nm/mm at 514.5 nm and a stray light rejection of 10^{-14} at 20 cm^{-1} from the Rayleigh line.[2.5] Such high dispersion and resolution were important for measuring narrow spectral emission and determining the values of pressures from ruby emissions. However, the actual resolution achieved during operation depends upon the slit widths (F1, F2, F3 and F4 in Fig. 2.5). The static bandwidth of a monochromator is found by multiplying the reciprocal linear dispersion by the slit width used. Normally the monochromator is used in scanning mode, which means that the total bandwidth is the sum of the static and dynamic bandwidths. The dynamic bandwidth is defined as the scanning rate in Å/s multiplied by the time constant of the associated detector. The typical curves are shown in Fig. 2.7.[2.6] There is always a trade off between resolution

and the signal-to-noise ratio, depending on equipment stability, scanning speed and time available for a scan.
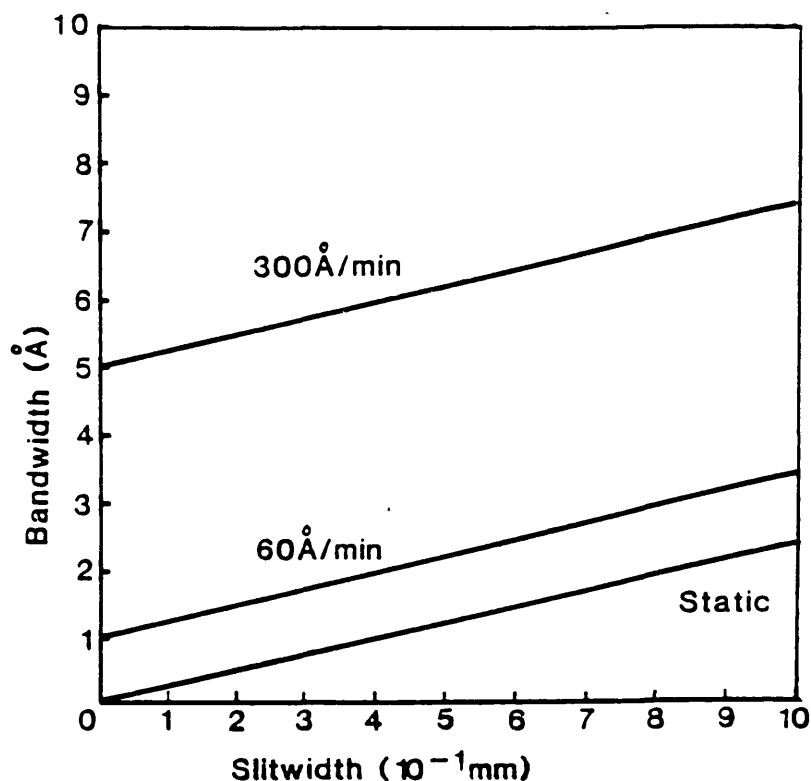
Fig. 2.7. Values of the total resolutions as a function of slitwidth for two scan speeds and a time constant of 1 second (After Watt, 1989).[2.6]

The spectrometer is controlled by a Jobin Yvon "Spectralink" spectrometer controller interfaced to an IBM compatible computer, which operates a superior electric stepper motor. The commercially written software package "PRISM" from ISA was used for data acquisition.[2.7] A laser line of known wavelength is used to calibrate the spectrometer. There is also a backlash effect when reversing the direction of travel of the spectrometer and so spectra need to be recorded always in the same direction and always approaching the start of the scan from the direction of travel of the scan.

2.1.5 Detector

For the visible region, light detection was performed using a Hamamatsu photo-multiplier tube (PMT), type R943-02, with a Cs-activated GaAs photocathode, with an approximate spectral range of 160 nm to 930 nm. The PMT was operated at 1.5 kV, supplied by a Thorn EMI photomultiplier power supply (type PM 28B).[2.8] In order to reduce thermal noise the PMT was cooled to approximately - 20 C° using a Pacific instruments PMT housing[2.9] and temperature controller,[2.10] utilizing the Peltier effect.[2.11] A Pacific Instruments model 3470/AD6 amplifier discriminator was used at the front end of the photon counting system.

Fig. 2.8 shows the spectral response of the detecting U1000 system, consisting of the light collecting optics, spectrometer (1800 grooves/mm grattings) and Hamamatsu photomultiplier tube (R943-02) cooled to - 20 C°.
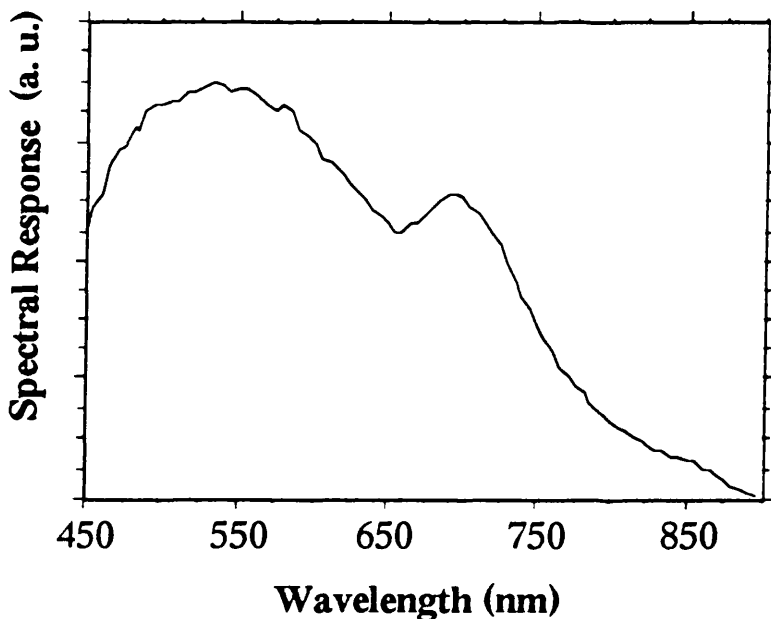
Fig. 2.8   Spectral response of U1000 system (After Watt, 1989).[2.6]

The spectral response was measured by passing light from a black body source through the spectrometer, measuring its spectrum and then correcting it for the known wavelength dependence of the emission from the black body source.[2.6]

2.2.   Low Temperature and Magnetic Field Experiments

2.2.1   Cryostats

(i)   Large Bore Optical Cryostat

Most of the optical measurements at low temperatures and high pressures were made using the cryostat depicted in Fig. 2.9. This cryostat was produced by Quantum Production Limited to specifications including: a temperature range of 1.5 - 300 K, a 50° optical access to the sample, and most importantly a large top loading aperture to take a diamond anvil cell. Both the inner and the outer windows were made of Spectrosil WF (water free) which has a flat spectral response from 250 nm to 2 μm and a transmission in excess of 80 % throughout the range.[2.6]

The cryostat could be operated in either bath or gas-flow modes, which depends on the temperature region of interest. Below 4.2 K, in bath mode, helium was transferred to the sample space from the helium reservoir through a needle valve. Once full, it was pumped by a rotary pump reducing the pressure and hence the temperature below the lambda point, where it became bubble free superfluid helium (temperature range 1.8 K to 2.1 K). For temperatures above 4.2 K, the cryostat operated in a gas flow mode. Helium gas was sucked through the needle valve and the sample temperature was controlled by balancing the cold gas/liquid input with the heat generated by a heater in the base of the cryostat, allowing the temperature to be varied from 4.2 K to 300 K, with an accuracy of ± 0.5 K.

Sample Insert

Needle Valve

(For controlling the liquid and gas
flow into the He₂ sample space)

Pumping port for the He₂ Sample space

N₂   N₂

He₄   He₄

25°

Windows, quartz Spectrosil WF

Sintered copper block

Sample position and optical axis of the cryostat
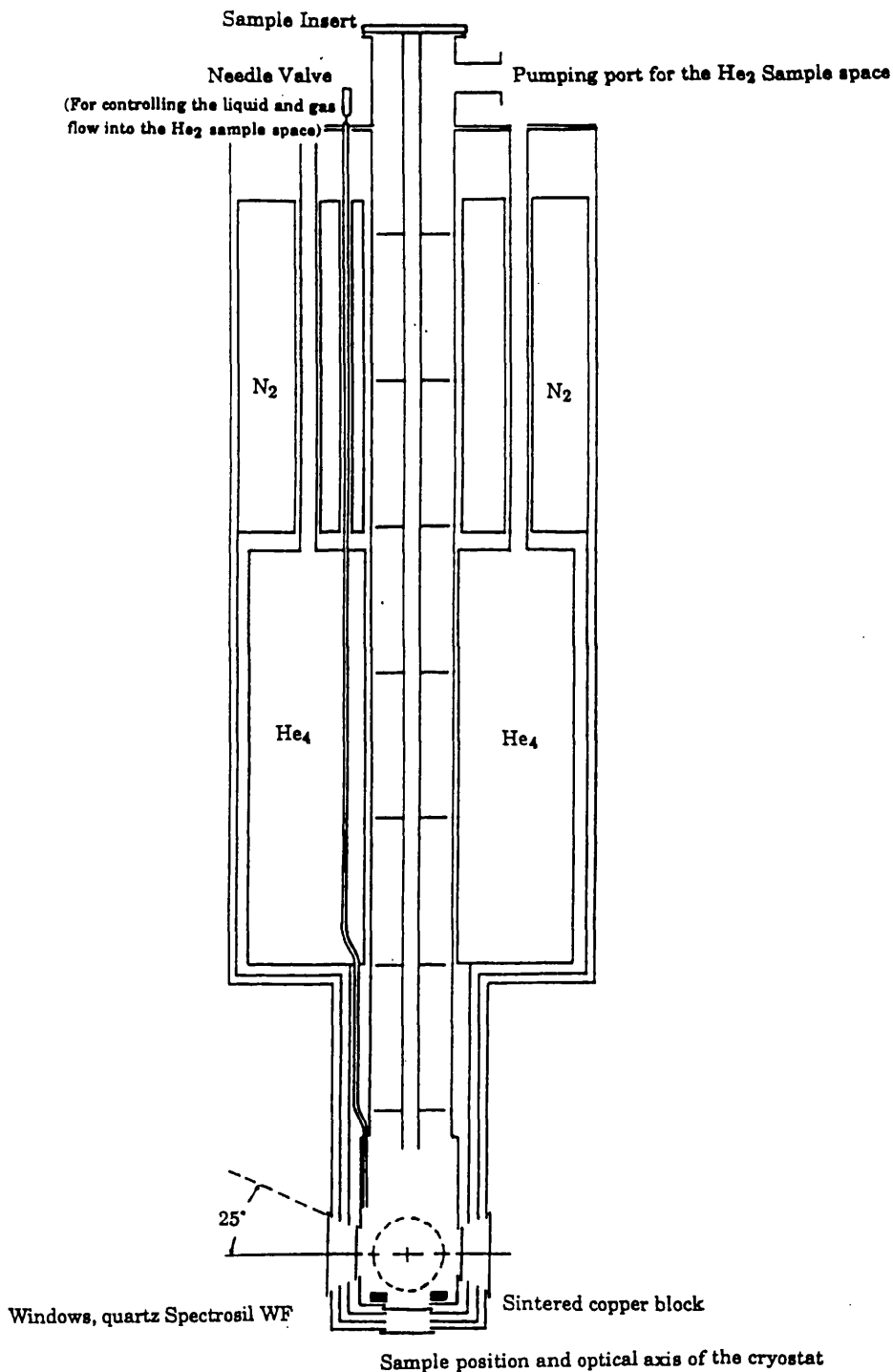
Fig. 2.9   Schematic diagram of the large bore optical cryostat used for the low temperature and high pressure experiments in this thesis.

(ii)   Baffle valve

In high pressure optical experiments, when the diamond anvil cell (DAC) was removed from the sample space of the cryostat to change sample pressures, air came into the sample space of the cryostat at the same time, which resulted in freezing on the optical windows, sometimes blocking the needle valve. This serious problem meant a rescheduling of the experiments since it was necessary to heat the cryostat back to room temperature.

To tackle this problem, a sample rod and a baffle valve were designed for the cryostat. The new sample rod allowed the sample position to be rotated through $360°$ and varied in the vertical direction. The baffle valve prevented air from coming into the sample space. The schematic of the baffle valve is given in Figure 2.10.
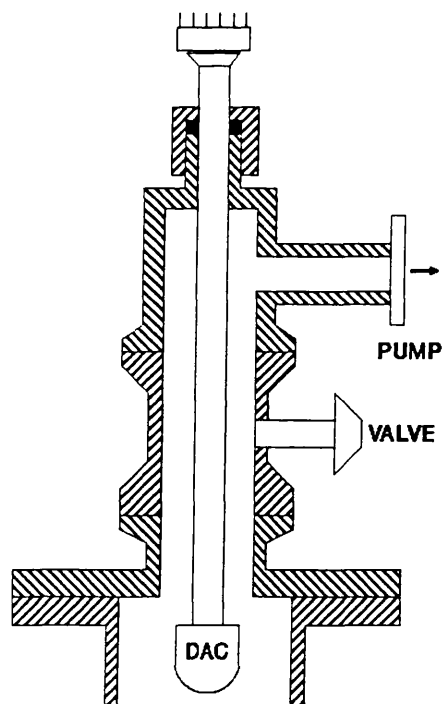
Fig. 2.10.   Schematic diagram of the baffle valve.

Since using this improved structure, the DAC could be moved to a separated region by closing the baffle valve and then, taking off the DAC from the cryostat. When the DAC inserted into the cryostat, the separated region could be pumped out before opening the baffle valve and then the DAC inserted into the sample space. In the whole process, no air came into the sample space. Consequently, the incorporation of the baffle valve made a significant con-tribution to shortening the running time of the high pressure experiments at low temperatures.

(iii)   Oxford Instrument Cryostat

For general low-temperature measurements, the Oxford Instrument CF1204 was used. The CF gas flow system is shown in fig 2.11.
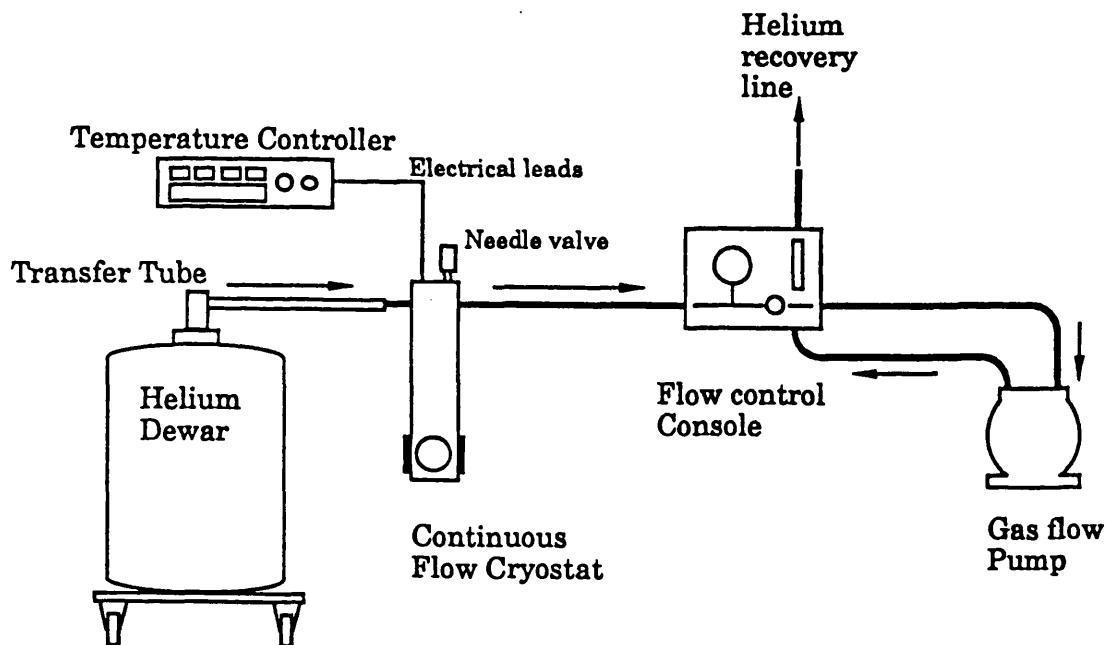
Fig. 2.11.   CF gas flow system for the Oxford Instrument CF1204 cryostat.[2.12]

The continuous flow cryostat operates by controlling the transfer of helium to a vacuum insulated, radiation shielded, sample space in the cryostat. Sample temperature was maintained to within ± 0.2 K by balancing the flow through the cryostat with

power applied to an electrical heater attached to a heat exchanger. Coolant flow is produced by generating a pressure difference between the sample vessel and the helium return line with a gas flow pump. The flow and pressure in the helium return line are monitored and controlled by the flow control console. The cryostat operates in bath mode by transferring helium from a dewar into a reservoir in the cryostat. Once the reservoir was full coolant flow through the cryostat could be controlled by the needle valve. By collecting helium in the sample chamber, sealing with the needle valve and pumping as described in the previous section a base temperature of ~ 1.8 K can be reached.[2.12]

A flow control console was used for the CF1204 cryostat. It consists basically of a vacuum gauge, needle valve and flowmeter, as shown in Figure 2.12. The gas from the cryostat enters the console, passes through the needle valve into the gas flow pump and flows along the helium return line through a calibrated flow meter. This unit controls the flow of helium through the cryostat and records helium consumption. A negative pressure gauge is connected to the gas flow line after it enters the console from the cryostat. This monitors the line pressure and can be used to check for blockages in the transfer or air leaks in the CF system.[2.12]
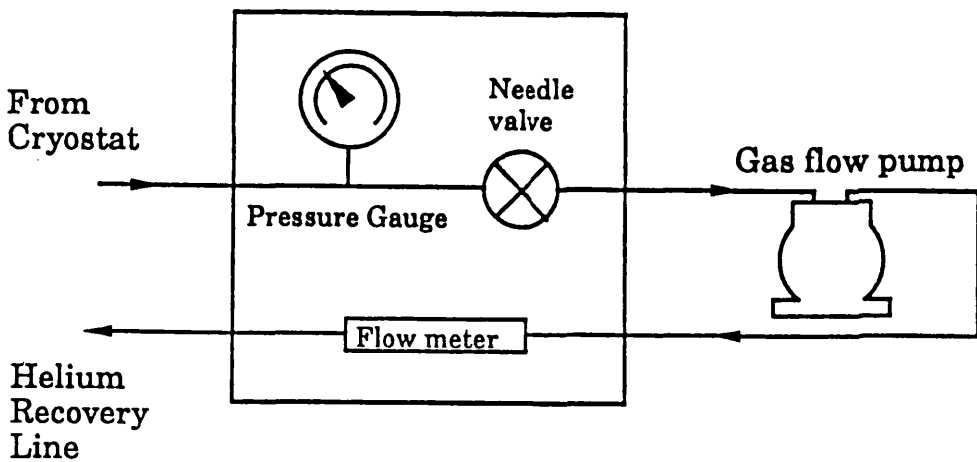
Fig. 2.12. Flow control console for CF gas flow system (After Ferguson, 1986).[2.12]

2.2.2.   Temperature controller

Temperature control and stability is very important for using a cryostat particularly above liquid helium temperatures. This can only be achieved with a temperature control unit providing a feedback system. The required temperature was, firstly, approximately obtained by controlling the flow of cold gas through a needle valve in the cryostat. The temperature controller was preset to the required temperautre and provided an error signal relating to the difference between the set point and the actual temperature. The error signal gave a proportional level for the electrical heat input into the cryostat tail to balance the cooling by the cold gas.

An Oxford Instrument Model ITC4 temperature controller with sensors attached was used to control the sample temperature. A RhFe resistor was used as the feedback temperature sensor. In the gas-flow mode a temperature gradient existed in the Quantum Products cryostat between the tail section and the sample insert. A sensor, a RhFe resistor, was attached to the insert to determine when the sample reached thermal equilibrium and obtain more accurate measurement of the actual sample temperature.

2.2.3.   Superconducting Magnet

For high pressure measurements in magnetic fields, a cryostat equipped with a superconducting magnet providing magnetic fields up to 8 Tesla was used. Its basic structure is similar to that of the large bore cryostat, but a superconducting magnet is hung near the bottom of the cryostat. A power supply was used to control the magnetic fields. A micro-diamond anvil cell (DAC) was inserted in the centre part of the magnet and the temperature was kept at 4.2 K. The magneto-optical investigations of high pressure spectroscopy were performed with two optic fibers which guided the ingoing laser light and the outgoing photoluminescence. All measurements were carried out with the magnetic field parallel to the growth axis of the samples.

2.3. High Pressure Measurements

2.3.1. Introduction

Over a period of over 20 years, the diamond anvil cell (DAC) has evolved into a fine quantitative tool for modern high pressure research.[2.13] In the history of this evolution several important innovations are to be recognised. They are (1) the introduction of the metal gasket technique[2.14] for hydrostatic pressure generation, (2) the discovery of the ruby fluorescence technique[2.15] for pressure calibration, and (3) the introduction of new pressure transmitting media.[2.16] A schematic of a diamond anvil cell with its main components is illustrated in Fig. 2.13.
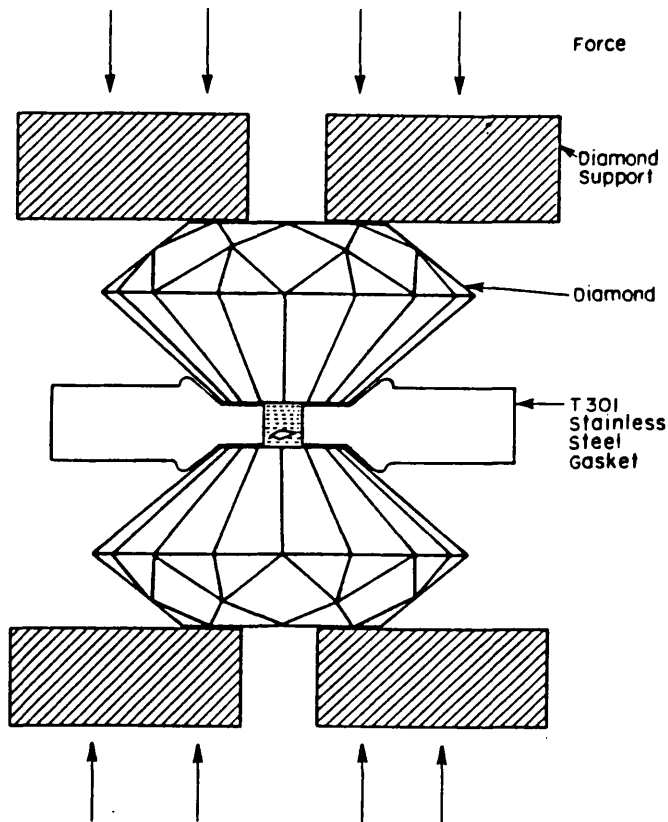
Fig. 2.13. Basic principle of the diamond anvil cell (After Jayaraman, 1986).[2.17]

- 52 -

Although many different types of cells have evolved, the basic principle of a diamond anvil cell is quite simple. When a metal gasket is compressed between the small flat faces (flattened by grinding and polishing of the culet) of two brilliant cut gem quality diamonds set in opposed anvil configuration, very high pressure is generated in the gasket hole, which is usually filled with a pressure transmitting medium. The reason for the generation of such high pressure is that the flat area is so small the applied load gets multiplied by a large factor (200 - 500, depending on the size of the flat).

For the successful operation of the diamond cell, the two anvil flats should be accurately centered and set parallel to each other. Further, a thrust generating mechanism and hardened backing support for the diamonds have to be provided. The cell can be designed in different ways to meet these requirements and this has given rise to several versions of the DAC.[2.17]

2.3.2.   Diamond Anvil Cells

The two diamond anvil cells (DAC) used in this work were a commercial Diacell DO-1 clamp cell (see Fig. 2.14) based on the Mao-Bell piston/cylinder cell[2.18] and a micro-diamond anvil cell mainly for high pressure experiments in magnetic fields (see Fig. 2.15), which was developed at the High Pressure Physics Institute of Russian Academy of Sciences.
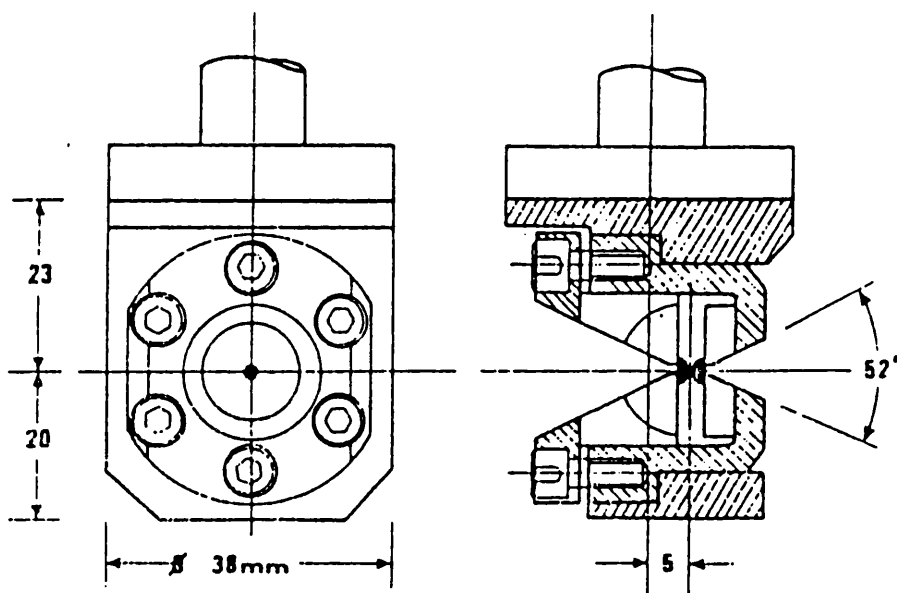
Fig. 2.14. A Diacell D0-1 mounted on a supporting rod.
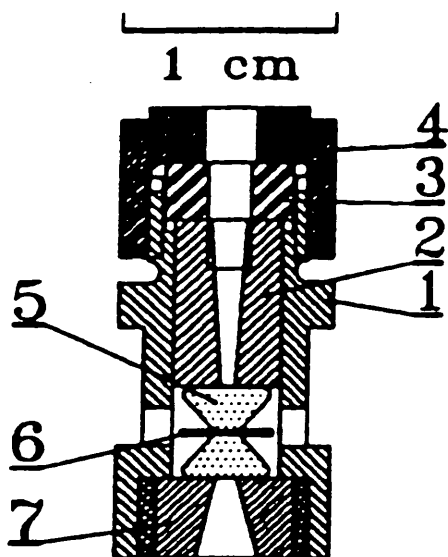
Fig. 2.15. A micro-diamond anvil cell. 1) The miniature cell body, 2) piston,

3) bearing, 4) nut, 5) anvils, 6) gasket, 7) support ring / cylinder.

The most important development in DAC usage, and the key to hydrostatic pressure generation, was the introduction of a metal gasket between the diamonds. The metallic gasket of beryllium-copper, stainless steel or inconel, is normally pre-indented from 200 μm to 100 μm before drilling a hole of 250 μm in the centre to reduce material flow and to provide a work hardened area. Not only does the gasket form the sample chamber containing the pressure medium, but it also extrudes around the diamonds, forming a seal acting as a supporting ring for them.

A sample thinned by hand to ~ 30 μm thick and cleaved to a ~ 50 - 100 μm square was placed inside the hole together with a pressure sensor ruby chip 10 - 20 μm and the pressure transmitting medium. In the diamond anvil cell, pressure is induced in the sample chamber by applying a force to the back surfaces of the diamonds, deforming the gasket. Sample volume is normally sacrificed for higher pressures.

2.3.3.   Pressure Calibration

With the introduction of the ruby fluorescence method in 1972 by Forman et al (1972)[2.15] a major obstacle to the DAC use, namely, pressure calibration, was removed, clearing the way for widespread use of DAC for high pressure investigation.

Below 200 kbar, the ruby R lines linearly shift to longer wavelengths at the rate of 0.0365 nm / kbar.[2.19] The ruby R lines are quite sensitive to temperature and exhibit a positive shift with temperature. The temperature coefficient $\Delta\lambda / \Delta T$ of the R line shifts with temperature at the rate of 0.0038 nm / K.[2.20] However, Noack and Holzapfel (1979)[2.21] have demonstrated that the linear scale holds good at any temperature. The gradient $\Delta\lambda / \Delta p$ remains the same regardless of the ruby temperature.

A tiny chip of ruby is placed in the pressure medium along with a sample, and the fluorescence is excited by any source of strong light. The R lines of ruby are quite intense, and the doublet R_1 and R_2 have the wavelengths 692.7 and 694.2 nm, respectively, at atmospheric pressure. Under pressure these shift to higher wavelengths and the shift is linear with pressure. The accepted value for the ruby R-line shift is 0.0365 nm / kbar or − 0.753 cm^{-1}/kbar.[2.13]

2.3.4   Low Temperature Pressure Transmitting Media

In using the DAC, consideration must be given to the choice of pressure transmitting medium particularly in ensuring that it will be hydrostatic at all pressures and temperatures used. This is most important for semiconductors where any uniaxial component to the applied pressure will split the valence band, complicating the observed transitions. A methanol-ethanol mixture in the ratio 4:1 was used, this should remain hydrostatic to 100 kbar.[2.16] The mixture can be used at low temperature as long as the pressurization is completed at room temperature and the cell then cooled.[2.18] Our own measurements confirm this, as no signs of non-hydrostatic pressures were observed in the ruby fluorescence.

Ch. 3 OPTICAL PROPERTIES OF $Al_{0.48}In_{0.52}As$

UNDER HYDROSTATIC PRESSURES

3.1.   Introduction

Originally the main motivation for growing semiconductor alloys such as Al_xGa_{1-x} As was to produce room temperature luminescence in the visible region. $Al_{0.48}In_{0.52}As$ appeared a good candidate as it had been shown to have a Γ-X crossover $\sim$ 100 meV higher than Al_xGa_{1-x} As.[3.1] More recently $Al_{0.48}In_{0.52}As$, grown lattice matched to InP and $Ga_{0.47}In_{0.53}As$, have become important for optoelectronic devices and heterojunctions. Its main advantage, as compared to InP, is its larger band gap resulting in a larger conduction band discontinuity $\Delta E_c = 0.6 \ \Delta E_g$ and consequently a better carrier and light confinement, e.g., in AlInAs/InGaAs lasers, whereas at the InP/InGaAs heterojunction $\Delta E_c = 0.4 \ \Delta E_g$.[3.2]

However, in the race to produce good quality superlattice structures of $Al_{0.48}In_{0.52}As/Ga_{0.47}In_{0.53}As$ with abrupt interfaces, detailed studies of the material and physical properties of $Al_{0.48}In_{0.52}As$ have been neglected. Some of the outstanding questions concerning AlInAs are the origin of the low-temperature emission, the behaviour of donors which may form metastable DX-like centres, and the pressure at which the X-minima cross the band edge (the conduction band crossover effects), all of which have serious implications in the performance of tunnelling and light emitting devices in that they give rise to conduction by "slower" carriers and light emission by less efficient states, respectively.

Defects and deep levels in semiconductors are characterized by strong lattice potentials which act to localize the electronic wave functions near the sites of the defects or impurities resulting in an enhanced electron-lattice interaction. Such potentials are dominated by short-range forces which are, in turn, strong functions of interatomic separations and the local lattice environment. By reducing the interatomic spacing, hydrostatic pressure can be used to significantly modify defect and deep level potentials

and to tune continuously the strength of the electron-lattice interactions. Thus results of pressure experiments can lead to new insights, allow testing of proposed models and aid in the determination of the microscopic nature of defects. Additionally, pressure results contain information on the lattice relaxations associated with the formation of defects as well as with the emission and capture of carriers at deep levels.

Hydrostatic pressure is a powerful tool to vary controllably the band structure and the energy sequence of the conduction band minima in semiconductors, while keeping constant extrinsic factors, such as the doping distribution, interface quality, etc, thus greatly helping the analysis of the electrical and optical processes occuring at atmospheric pressure. In addition to relative band movements, there is some change in the electron dispersion relation. This is most pronounced around the Γ minimum of the conduction band where the relative increase in effective mass, m*, is approximately proportional to the relative increase in the direct band gap.[3.3] For GaAs, the pressure dependence of the effective mass reported by Wasilewski and Stradling[3.4] is given by :

$$m* (p) / m* (0) = 1 + 6.15 \times 10^{-3} p - 1.22 \times 10^{-5} p^2 , \qquad (3.1)$$

where the pressure, p, is expressed in kbar. The changes in the heavy hole mass and the electron masses in the L- and X- minima are relatively small and are usually neglected.[3.5]

From the near band-edge luminescence shift to higher energies as the pressure is increased, an initial pressure coefficient for the band gap can be derived. As the pressure is further increased, the luminescence quenches around the Γ-X cross-over as the material becomes dominated by an indirect level which can be tracked to lower energies in the case of the X-point. This allows the characteristics of X-minima related levels, such as impurity binding energy, to be examined experimentally. Thus, using

hydrostatic pressure allows the band structure to be tuned to exactly the right condition for the observation of certain processes and also makes accessible parts of the electronic band structure only indirectly observable at atmospheric pressure.

It has been suggested that the low-temperature emission of $Al_{0.48}In_{0.52}As$ is due to band-to-band transitions or bound excitons,[3.6] but other assignments such as free-to-bound and donor-acceptor-pair transitions also should be considered. The correct assignment of the $Al_{0.48}In_{0.52}As$ emission is crucial since an accurate estimate of the lattice matched band-gap energy depends on it. This is complicated in alloys such as $Al_{0.48}In_{0.52}As$ as the near band-edge luminescence does not show the sharp excitonic transitions observed in binaries such as GaAs. PL work on $Al_{0.48}In_{0.52}As$ under hydrostatic pressure by Ferguson et al[3.7] reported the linear pressure coefficient of the direct conduction band gap to be 10.1 meV/kbar at 80 K. In their work it was hoped to observe the Γ-X cross-over at ~ 60 kbar (Γ-X separation in energy at 1 bar is ~ 0.6 eV), but no emission associated with the X-level was observed for the $Al_{0.48}In_{0.52}As$ at 80 K up to 65 kbar.

To the best of our knowledge no experimental results for the pressure-dependent low temperature emission have been reported in $Al_{0.48}In_{0.52}As$. The motivation for this work was to identify the low-temperature emission and to provide a detailed high pressure investigation of the luminescence properties of $Al_{0.48}In_{0.52}As$, grown lattice matched to InP.

These studies consist of PL and PLE measurements. Our results provide an insight into the luminescence processes that occur in $Al_{0.48}In_{0.52}As$, especially with respect to the changes in luminescence mechanisms that occur concurrently with the crossover between the direct- and indirect-related bands. At the same time these studies have furnished important data on the pressure behaviour of impurity states in the alloy.

3.2.   Experimental Considerations

3.2.1   Samples of $Al_{0.48}In_{0.52}As$

All the samples studied in $Al_{0.48}In_{0.52}As$ work were grown epitaxially on InP substrates by MBE at British Telecom. The typical thickness of the $Al_{0.48}In_{0.52}As$ layers is ~ 2 μm. Table 3.1 is the summary of the luminescence properties of $Al_{0.48}In_{0.52}As$.

Table 3.1   Summary of the luminescence properties of $Al_{0.48}In_{0.52}As$

Sample	Growth Temperature (°C)	Emission at 2K (eV)	HWHM (meV)	n (CV) at 297K (x 10^{15} cm^{-3})	Doped
MV402	550	1.5309	21.7	8.0	Si
MV408	580	1.5498	16.9	1.0	u / d
MV409	580	1.5460	15.6	9.0	u / d
MV411	580	1.5333	17.4	2.3	u / d

3.2.2   Experiments

A key aspect in high pressure measurements is sample preparation. The best way of thinning the samples, to the required total thickness of ~ 30 μm, was found to be mechanical polishing the substrates by hand. Once the samples were thinned, they were cleaved, by hand under a microscopy, into some pieces ~ 100 μm x 100 μm for loading. In many instances, the process of cleaving appeared to result in the loss of the epitaxial layer. This happened occasionally for sample MV402 and often for other samples, so sample MV402 was mainly used in high pressure experiments.

A single sample and a fine ruby particle were placed in a gasketed Diacoll diamond anvil cell (DAC). A 4 : 1 mixture of methanol and ethanol was used as the pressure transmitting fluid. The pressure was determined using the ruby luminescence method and its pressure dependence.[3.8]   The DAC was inserted in avariable-temperature

cryostat which was cooled by liquid helium. In order to achieve optimal hydrostatic conditions, the pressure was changed only at room temperature.

The PL spectra were excited using the 476 nm line from an Argon-ion laser. The emitted light was dispersed by a double-gratting 1m monochromator and detected with a cooled GaAs photomultiplier tube. The PLE apparatus was similar to the PL apparatus, where a dye laser was used as the excitation source with DCM dye which had a tuning range of 610 - 710 nm. The spectra were recorded at 2 K. The typical spectral resolution was 0.1 nm ($\sim$ 0.2 meV).

3.3. $Al_{0.48}In_{0.52}As$ under Hydrostatic Pressure

3.3.1.   Luminescence of $Al_{0.48}In_{0.52}As$ under Pressure

In Fig.3.1 we show the photoluminescence spectra of $Al_{0.48}In_{0.52}As$ under various hydrostatic pressures at 2 K. Each of the spectra is normalized to its maximum intensity. The p = 1bar spectrum consists of one strong peak A at 1.5309 eV and a much weaker peak B at 1.600 eV. The low energy emission A is assigned to the $Al_{0.48}In_{0.52}As$. The higher energy emission B may be a consequence of Si doping of the $Al_{0.48}In_{0.52}As$ sample, but its assignment is uncertain at moment.

Upon applying pressure we can see that peaks A and B both shift rapidly upward in energy. The lower energy, broad band, emission C is due to the InP substrate. Increasing the sample pressure further to 47 kbar, the peaks A and C both move to higher energies. However, at a certain pressure p_c (50 - 55 kbar), the shift of the PL spectra from $Al_{0.48}In_{0.52}As$ saturates. When the pressure is increased to 59 kbar (above the critical value p_c), peak A disappears and a new peak of weaker intensity than peak A is observable. This new peak is labelled A' in Fig. 3.1. With increasing the pressure, peak A' tends to move down slowly in energy, followed by a complete disappearance of this emission at $\sim$100 kbar.
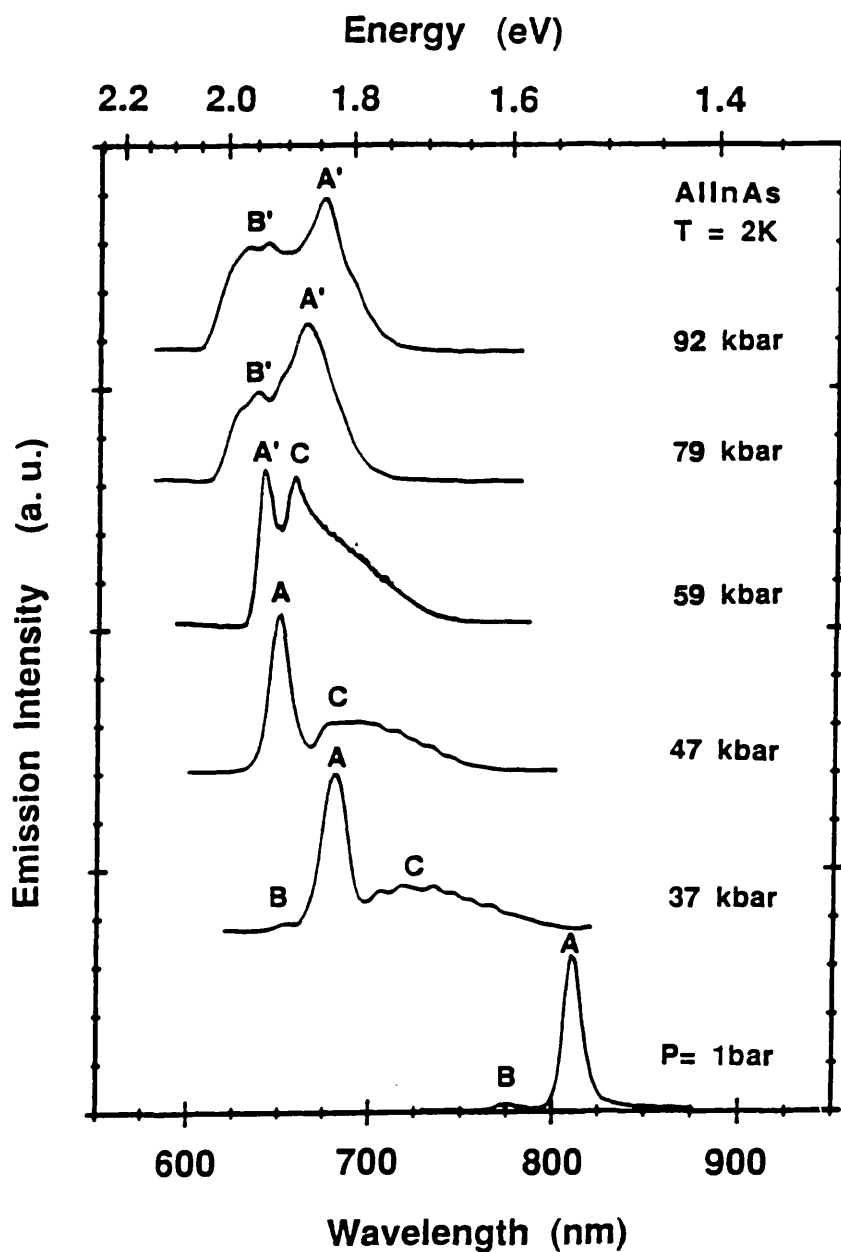
Fig. 3.1.   PL spectra of $Al_{0.48}In_{0.52}As$ under various pressures at 2 K. At p = 1 bar,

emission A is direct. With increasing pressure, the Γ-like state is shifted

above the X-like state, permitting indirect emission A' to be seen.

It is well known that the Γ-conduction band of $Al_{0.48}In_{0.52}As$ has a positive pressure coefficient, whereas the indirect X-conduction band has a smaller negative one. Like many other mixed III-V compounds, the fundamental band gap of $Al_{0.48}In_{0.52}As$ is direct for low pressure, but indirect for high pressure. With increasing pressure, the Γ-band edge increases and the X-band edge decreases relative to the valence band, so it is expected that the direct-indirect crossover takes place at a certain critical pressure value p_c in $Al_{0.48}In_{0.52}As$.

When the X- and the Γ-minima of the conduction band come closer in energy, some electrons begin to occupy the X-like states. This results in a decrease in the emission intensity. Based upon the shifts of the two peaks A and A', revealed by the application of pressure, we identify peak A as direct-band related emission, and peak A' as stemming from indirect-band related recombination.

It is worth noticing that we also observe a new peak labeled B' at the higher energy side of the peak A' when the pressure is greater than 70 kbar. This new peak B' is almost independent of the pressure within the range studied of 45 - 92 kbar. The reason for this phenomenon is not yet clear; we tentatively suggest that it may be associated with DX-like states in the $Al_{0.48}In_{0.52}As$ sample and with a pressure- induced shallow-deep transitions.

3.3.2.   Pressure Dependences and Energy-band Crossover

The spectral peak positions in these spectra and additional spectral not shown in Fig. 3.1 are plotted as a function of pressure in Fig. 3.2 over the 1 bar - 92 kbar pressure range. Since the pressure shifts were found to be essentially linear over this range, a least-squares fit was employed for each set of data using the linear function:

$$E^{\Gamma(X)}(p) = E^{\Gamma(X)}(0) + \alpha^{\Gamma(X)} p \,, \tag{3.2}$$

where energy E is in eV and pressure p is in kbar. The linear fits to the data points and the pressure coefficients obtained from the slopes are shown in Fig. 3.2.
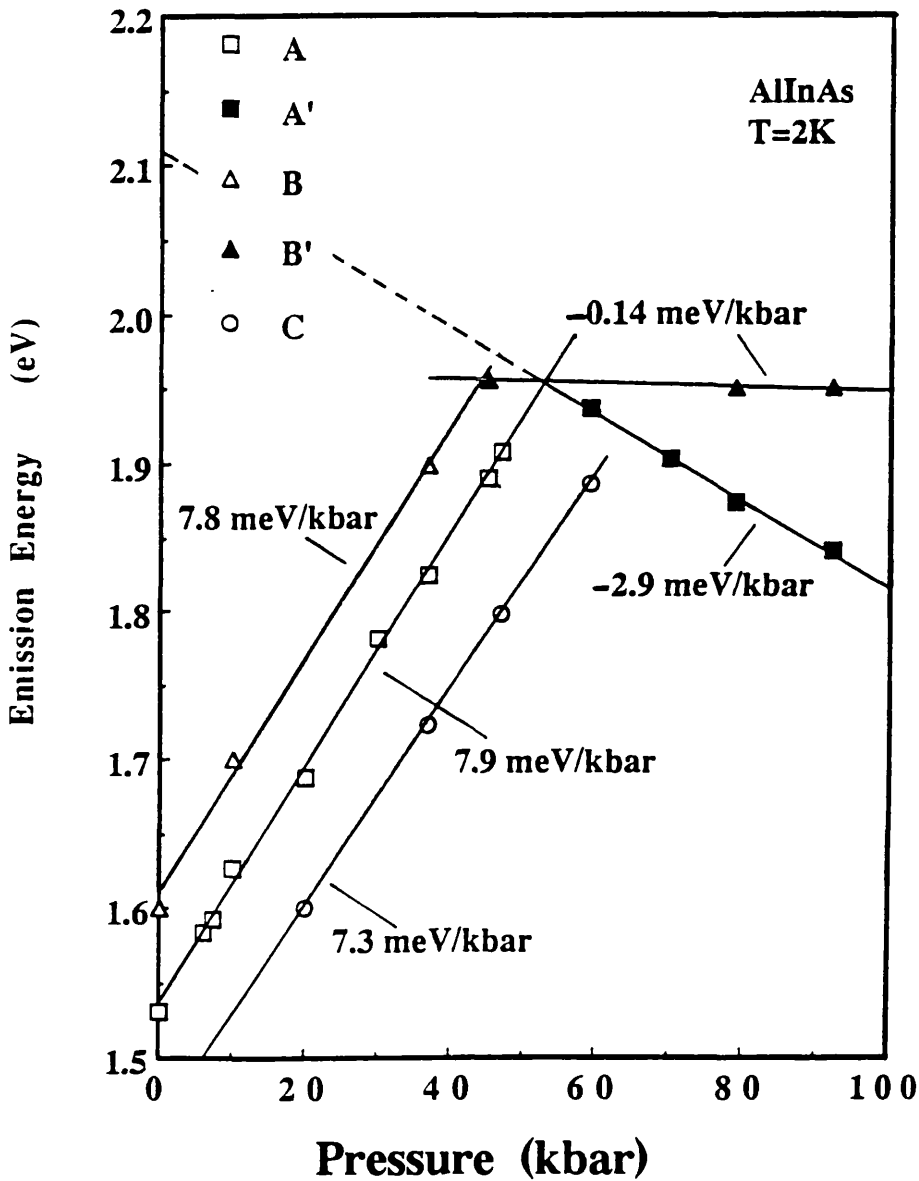
Fig. 3.2.   Photon energy of emissions A, A', B, B' and C as a function of pressure for $Al_{0.48}In_{0.52}As$ at 2 K. The solid lines are least-squares fits to the data. The crossover of the direct-indirect related states occurs at ~ 52.5 ± 0.5 kbar.

The direct-band related emission A of the $Al_{0.48}In_{0.52}As$ shows a linear pressure shift of 7.9 ± 0.1 meV/kbar over this range, parallel to that of emission B. This linear pressure coefficient is almost the same as that of bulk InAs of 8 meV/kbar,[3.9] but significantly lower than that of AlInAs of 10.1 meV/kbar at 80 K.[3.7] One possibility may be related to the pressure dependence of the donor binding energy. The indirect-band related emission A' shifts at a rate of ‐ 2.9 ± 0.1 meV/kbar, which is close, but not equal, to the shift of the X-Γ indirect-band gap of bulk GaAs (‐ 1.8 meV/kbar at 110 K).[3.10] The emission B' almost does not move with pressure and shifts at a very small rate of ‐ 0.14 meV/kbar. The pressure coefficient of the InP emission C seen from the substrate is 7.3 ± 0.1 meV/kbar, which compares well with that obtained by Menoni et al[3.11] at 20 K of 7.5 meV/kbar and by Tozer et al at 5 K of 7 meV/kbar.[3.12]

We find that at low temperature (T = 2 K) the direct-indirect related states crossover occurs at a pressure of p_c = 52.5 ± 0.5 kbar. The PL spectra of $Al_{0.48}In_{0.52}As$ are characteristic of direct-band related processes for p < 52.5 kbar. When the pressure p = p_c, the Γ-related and X-related states are located at the same energy level, the electron wave function of the Γ-related state will have a significant overlap with that of the X-related state. As a result, an additional recombination may appear, shown as E^X in Fig. 3.3.

As the X-related state is pressure shifted below the Γ-related state, electrons are readily scattered into the lowest-energy state, resulting in a reduction of the emission intensity. Thus the PL spectra are characteristic of indirect-related recombination for p > 52.5 kbar, as is schematically shown in Fig. 3.3. This critical pressure, p_c, can be expressed as follows:

$$p_c = \{ E^X(p = 0) - E^\Gamma(p = 0) \} / (\alpha^\Gamma - \alpha^X), \qquad (3.3)$$

where α^Γ and α^X are the pressure coefficients of the Γ- and the X-related states in $Al_{0.48}In_{0.52}As$, respectively, and $E^X(p = 0)$ and $E^\Gamma(p = 0)$ are the photon energies of the transitions from the X- and the Γ-related states to the Γ-related states associated to the Γ point of the valence band at atmospheric pressure, respectively.
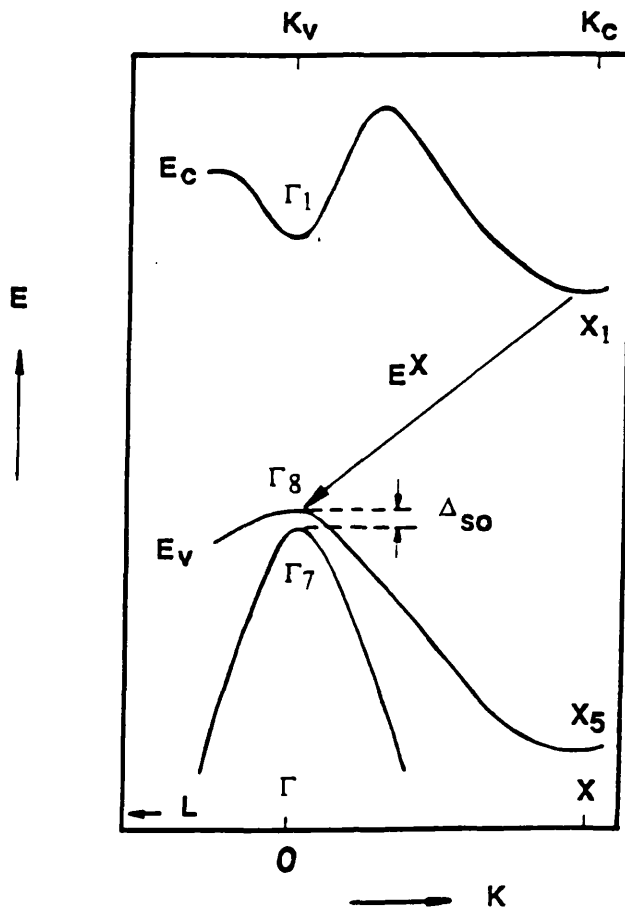
Fig. 3.3.   Schematic diagram of the band structure of the III-V compound semi-conductors with indirect band gap.[3.13]

By extrapolating the E^X line back to atmospheric pressure, as indicated by the

dashed line in Fig. 3.2, the indirect transition energy at atmospheric pressure is deduced to be E^X (p = 0) ~ 2.1 eV. Therefore, the energy difference between the X-like and Γ-like states under atmospheric pressure is ~ 570 meV at low temperature (T = 2K). Considering that at T = 300 K, the energy difference between X- and Γ- conduction band minima of $Al_{0.48}In_{0.52}As$ is ~ 430 meV [3.1] and that the temperature coefficients of X- and Γ- conduction bands are different, (for example, the temperature coefficient of energy difference between X- and Γ- conduction band minima is equal to - 0.37 meV/K for InP[3.14]) our result of ~ 570 meV at 2 K is very reasonable.

Finally, it should be mentioned that we see no evidence of transitions associated with the X-valley when the material is direct. In fact, the change is rather abrupt (see Fig. 3.2) as the sample goes from the direct state to the indirect one.

3.3.3.   Identification of Low Temperature Emission

Previous studies of luminescence processes in $Al_{0.48}In_{0.52}As$ have suggested that the low-temperature emission is due to band-to-band transitions[3.6]   or bound excitons.[3.15]   Other assignments such as free-to-bound and donor-acceptor-pair (D^O, A^O) transitions have also been considered.[3.7]   The correct assignment of the $Al_{0.48}In_{0.52}As$ emission is crucial since an accurate estimate of the lattice matched band-gap energy depends on it.

Our investigations involved the low-temperature luminescence in $Al_{0.48}In_{0.52}As$ under high pressures. It provides, for the first time, sufficient systematic data to lead to definitive conclusions about the nature and the pressure dependence of the low-temperature luminescence in this alloy.
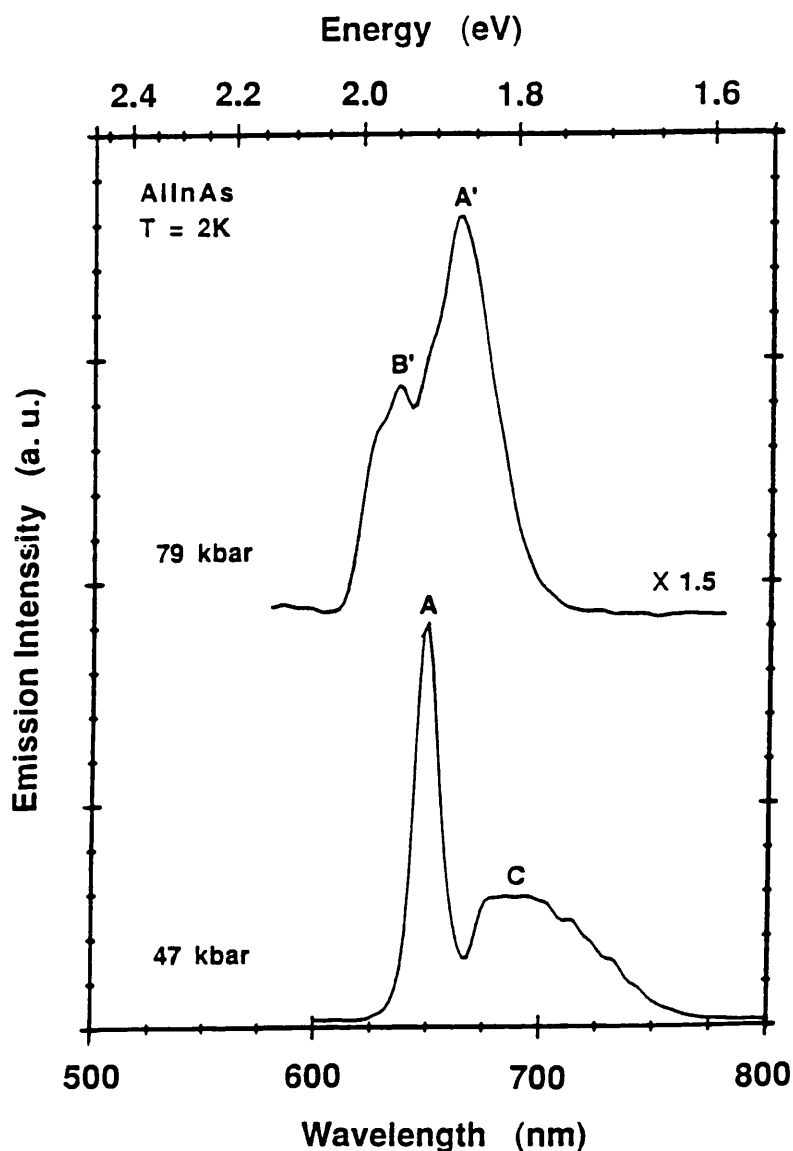
Fig. 3.4.   PL spectra of $Al_{0.48}In_{0.52}As$ at pressures 47 kbar and 79 kbar at 2 K. Emission A is direct (47 kbar < p_c) and emission A' is indirect (79 kbar > p_c). The intensity of indirect-related emission A' is comparable to that of direct-related emission A.

In Fig. 3.4. we show the PL spectra at 2 K and two different pressures, one having a direct-related emission A (47 kbar < p_c) and the other one having an indirect-related

emission A' (79 kbar > p_c). The interesting point to note is that, at low temperature, in contrast to the PL intensity behaviour at higher temperatures, the intensity of indirect-related emission A' is comparable to that of direct-related emission A. The reason for that is discussed later in this chapter. We believe that peaks A and A' are both due to donor-acceptor-pair (D^O, A^O) recombinations, which is consistent with the high impurity densities in all the $Al_{0.48}In_{0.52}As$ samples for this work.

The evidence that emissions A and A' in the $Al_{0.48}In_{0.52}As$ alloy are due to (D^O, A^O) recombinations comes from three sets of experiments: (1) dependence of the spectra on excitation intensity, (2) temperature dependence, (3) photoluminescence excitation. We will discuss the first two in this section and the last in Sec. 3.3.4.

3.3.3.1.   Donor-acceptor-pair Emission

As depicted in Fig. 3.5, free electrons can be captured by positively charged (ionized) donors. Similarly, free holes can be captured by negative (ionized) acceptors. It is usually assumed that since the temperature is low, the electrons and holes will stay bound because there is not enough thermal energy to ionize them into the conduction or valence bands. However, this assumption is only partially valid, since electrons and holes have wave functions that spread out in the crystal away from the impurity atoms. Consequently, even though the donors and acceptors are separated from one another, there is a non-negligible overlap of wave functions which results in a finite probability of recombination of the electron and hole with the generation of a photon (see Fig. 3.5). The emitted photon energy is given by :[3.13]

$$E(r) = E_g - (E_A + E_D) + e^2 / \varepsilon r , \qquad (3.4)$$

here E_g is the band-gap energy, E_A and E_D are the acceptor and donor binding

energies, ε is dielectric constant and r is the actual separation between acceptor and donor.
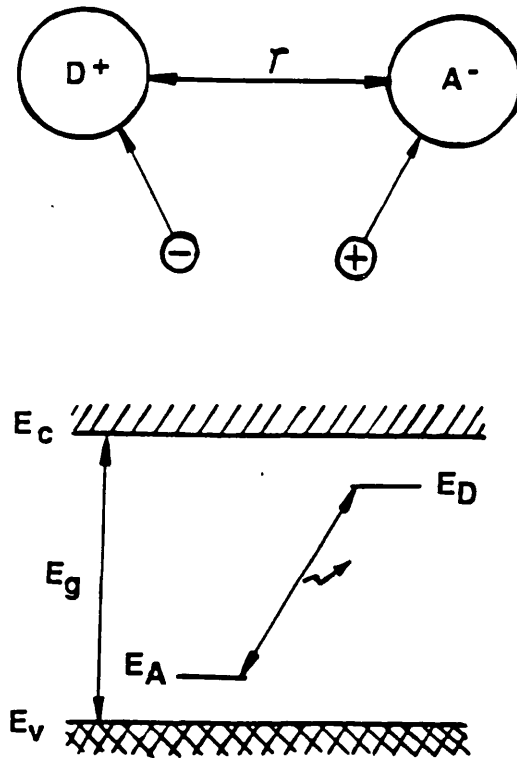
Fig. 3.5.   **Above**: schematic representation of the capture of a free electron-and-hole pair at ionized donor and acceptor atoms respectively.

Below: subsequent radiative recombination of the trapped particles results in donor-acceptor-pair emission. The emitted energy $h\nu$ decreases with increasing r due to coulombic interaction.[3.16]

Since r is discrete, fine structure can be observed in the luminescence but as the donor to acceptor separation increases a continuum of energy states is manifested as broad-band emission. In most III-V compounds, only distant pair luminescence is

observed and since the binding energies of donors and acceptors are small, emission of any fine structure is usually precluded, particularly in semiconductor alloys.

The ground state of the donor-acceptor pairs is composed of an ionized donor and an ionized acceptor state: (D^+, A^-). It will be reasonable to assume that the radiative transition in the recombination process in the pairs occurs between the lowest excited state and the ground state, i.e. { D(1S), A(1S) } → { D^+, A^- }, where D (1S) denotes the state of the electron bound to the donor 1S level. The photons absorbed in the crystal can generate the excited states of the donor-acceptor pair by three types of processes: a) direct transition within the donor-acceptor pair, b) excitation via conduction electrons, c) band-to-band excitation as schematically shown in Fig. 3.6.[3.17]
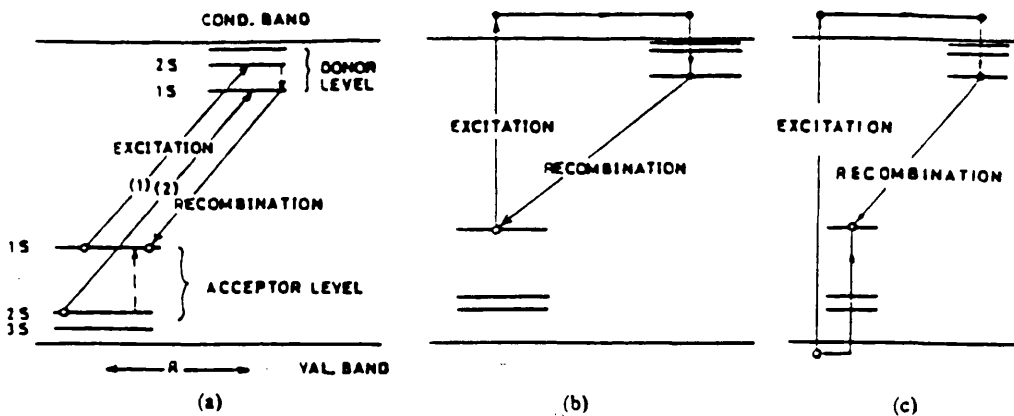
Fig. 3.6. Excitation processes for the (D^0, A^0) in semiconductors:[3.17]

        a) Transition within the pair,

        b) bound-to-free transition,

        c) band-to-band transitions.

3.3.3.2.   Dependence on Excitation Intensity

A simple theoretical analysis shows that the PL integrated intensity PL(I) varies with incident excitation intensity P_{in} according to the relationship[3.18]

$$PL\ (I) = C\ P_{in}{}^s,\qquad\qquad (3.5)$$

where C is a constant and it is assumed that no saturation occurs. The exponent s depends on the mechanism of recombination: for weak excitation the $(D^O,\ A^O)$ transition has s = 1.[3.19] Since the formation of excitons is proportional to the product of the two photocreated populations in the bands, the exciton emission intensity should increase quadratically with excitation density. When s > 1, it indicates a transition that is free-carrier-associated such as free-to-bound or band-to-band.

Fig. 3.7 shows the excitation dependence of the integrated photoluminescence intensity of $Al_{0.48}In_{0.52}As$ at T = 2 K for different pressures. The exponent s in equation (3.5) is also indicated. The direct-related emissions, at p = 10 and 47 kbar, have an excitation intensity dependence with s = 0.93 and 1.07, respectively, which are slightly less and larger than unity. However, the indirect-related emissions, at p = 79 and 92 kbar, have s = 0.82 and 0.77, respectively, which are significantly less than those for the direct-related transitions. It is because there is higher probability of non-radiative recombinations in the X-valley and a slower τ_{rad}.

The exponent s depends on the temperature for different emission mechanisms. In Fig. 3.8 we can see that when the temperature raises only ~ 38 K, the s value drastically increases from 1.07 (2 K) to 1.33 (40 K) at the same pressure 47 kbar. This indicates that the emission at 40 K is free-carrier-associated such as $(e,\ A^O)$. Because of s ~ 1 and s < 1 at low temperature over the pressure range of 1 bar ~ 92 kbar in both direct- and indirect-related transitions, we suggest that the low-temperature emission of

$Al_{0.48}In_{0.52}As$ is not free-carrier-associated since $s > 1$ for them, but due to (D^O, A^O) recombination.
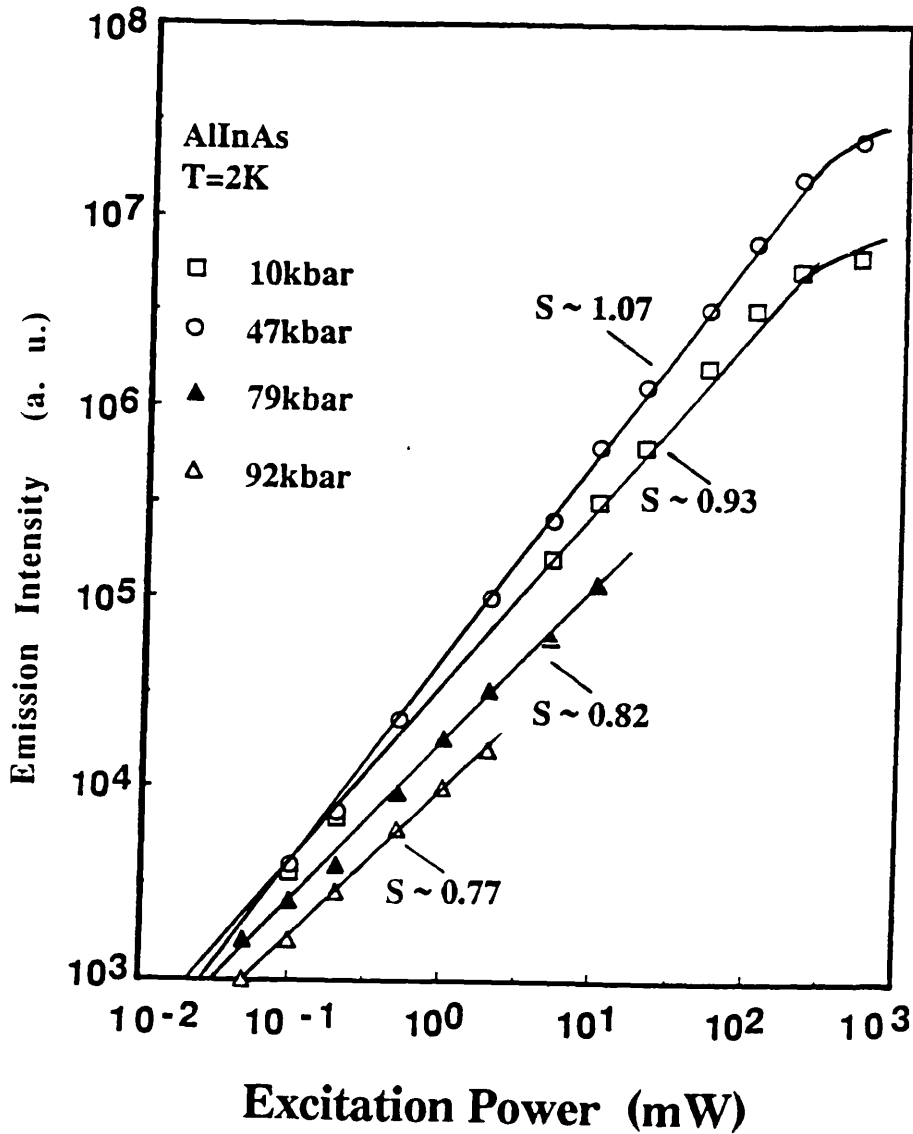
Fig. 3.7. Dependence of the integrated emission intensity of $Al_{0.48}In_{0.52}As$ upon excitation intensity at 2 K. The exponent $s \sim 1$ for direct-related emissions, at $p = 10$ and 47 kbar. However, the exponent $s < 1$ for indirect-related emissions, at $p = 79$ and 92 kbar.
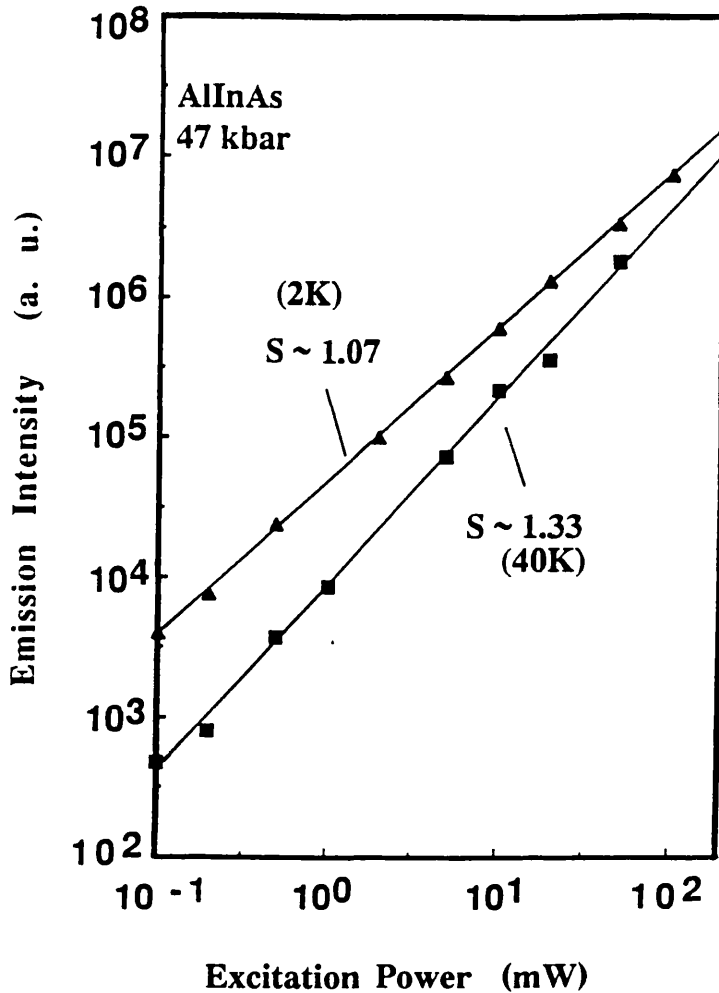
Fig. 3.8. Dependence of the integrated emission intensity upon excitation intensity at p

= 47 kbar. The exponent s increases from 1.07 at 2 K to 1.33 at 40 K

indicating that at 40 K the emission is associated with free carrier.

One of the characteristics of the (D^0, A^0) transition is that the more distant pairs

saturate with increasing excitation intensity. For pairs with large separations, the

overlap between the wave functions of the trapped holes and electrons will be very

small and as a result the radiative lifetime will be long. Consequently, the distant pairs

may become saturated, and the extra holes and electrons will be forced to find the less

likely, more closely spaced pairs. This effectively increases the importance of shorter r

transitions and results in a shift of the emission peak towards higher energy as can be seen from Eq. (3.4). We have observed precisely such shifts of the emission at all the pressures studied here.
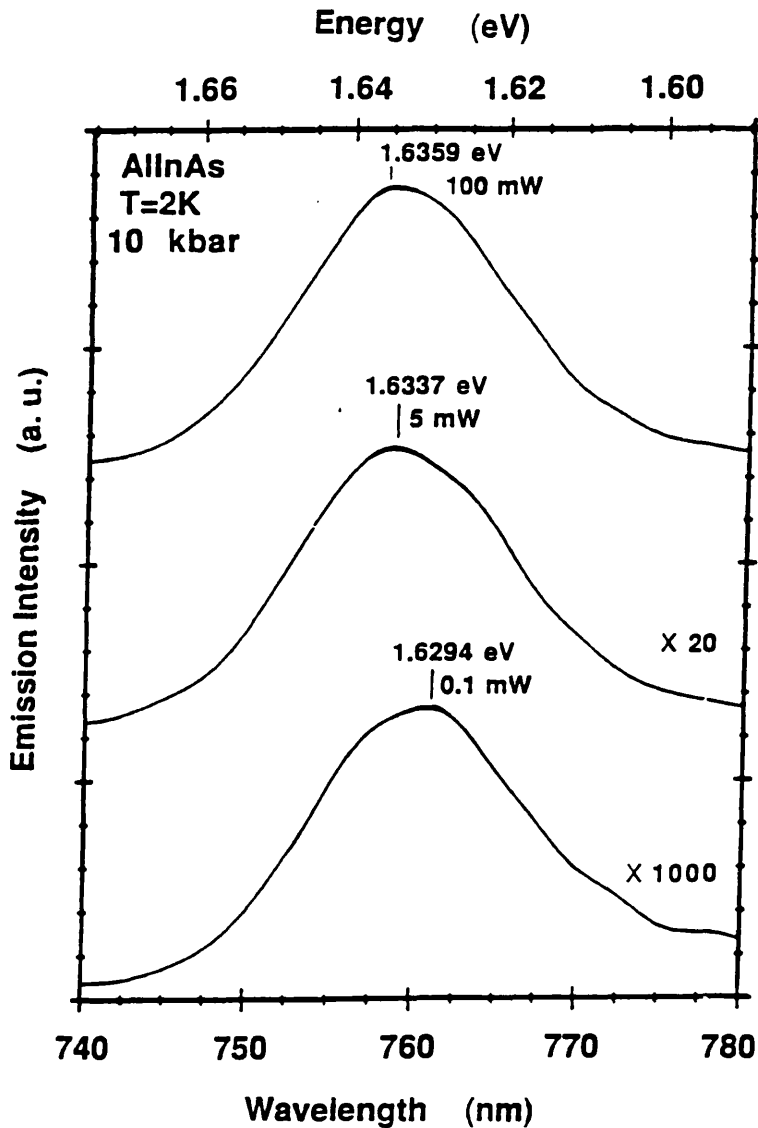
Fig. 3.9.(a).   Shifts in the emission peaks of $Al_{0.48}In_{0.52}As$ to higher energies as the excitation power is increased for the direct-related emission at p = 10 kbar.

Fig. 3.9 (a) and Fig. 3.9 (b) show the emission shifts to higher energies for sample MV402 at pressures p = 10 and 79 kbar, respectively. The (D^O, A^O) transition moves to higher energies as the excitation power is increased for the direct-band gap (Fig. 3.9 (a), p = 10 kbar) and the indirect-band gap (Fig. 3.9 (b), p = 79 kbar).
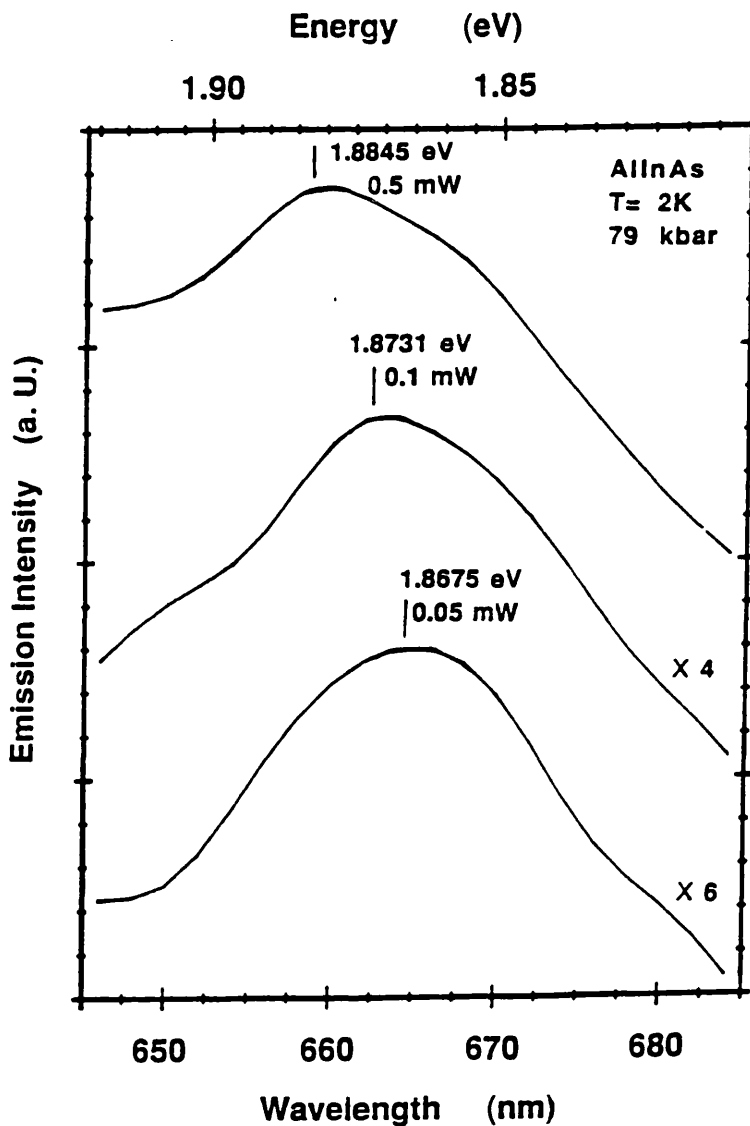
Fig. 3.9.(b).   Shifts in the emission peaks of $Al_{0.48}In_{0.52}As$ to higher energies as the excitation power is increased for indirect emission (p = 79 kbar).

Another characteristic of the (D^O, A^O) spectra is that the (D^O, A^O) emission intensity is expected to saturate with increasing excitation intensity above a certain intensity. Since a limited number of impurities exist within a semiconductor, as the excitation intensity is increased the observed emission intensity should saturate when the photon flux approaches the donor/acceptor density. We have observed a tendency towards this behaviour in our $Al_{0.48}In_{0.52}As$ sample MV402 (see Fig. 3.7) when the excitation power approaches ~ 200 mW: the (D^O, A^O) emission intensity shows the expected bowing in the curves of p = 10 and 47 kbar. This suggests that the saturation starts at ~ 200 mW.

Finally, it should be mentioned that the shift of the emission to higher energy with increasing excitation power is consistent with (D^O, A^O) recombination. However, the same behaviour is expected for localized transitions, as the localized centres are saturated at higher laser power. Therefore, we further studied the temperature dependence of the PL spectra of $Al_{0.48}In_{0.52}As$.

3.3.3.3.   Temperature Dependence

We have studied the PL spectra of the $Al_{0.48}In_{0.52}As$ as a function of temperature between 2 and 120 K. Two features of the data are of interest and are discussed below.

Fig. 3.10 shows the temperature dependence of the direct-related emission of $Al_{0.48}In_{0.52}As$ at 47 kbar (p < p_c). At 2 K two main emissions are observed one (A) peaking at 650 nm and the other (C), a very broad band emission, peaking at 686 nm. They were assigned to the $Al_{0.48}In_{0.52}As$ epitaxial layer and the InP substrate, respectively. The InP substrate luminescence corresponds to the free-to-bound transition (e, A^O) and the $Al_{0.48}In_{0.52}As$ emission is identified as due to donor-acceptor-pair recombination (D^O, A^O).

Energy   (eV)
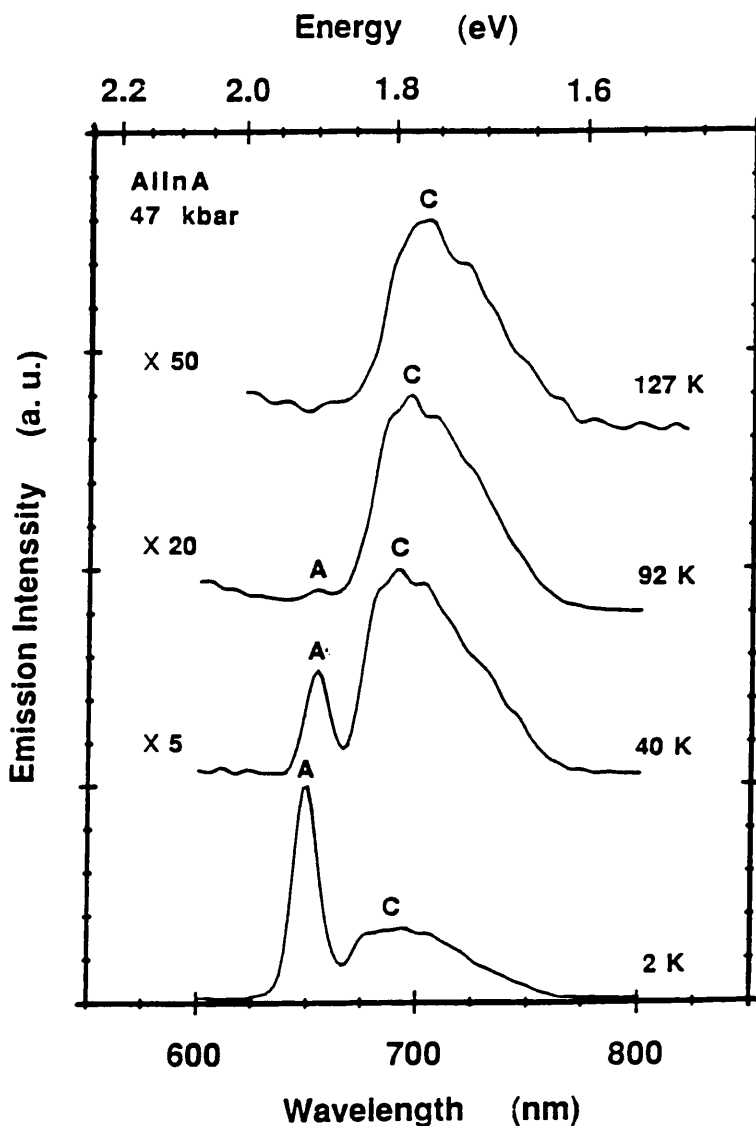
Fig. 3.10.   Temperature dependence of the $Al_{0.48}In_{0.52}As$ emission A at 47 kbar (p <
p_c). With increasing temperature, the intensity of peak A decreases
rapidly. At ~100 K, peak A quenches completely.

With increasing temperature to 40 K, both emissions become weaker and shift
towards lower energies because of a reduction in the band gap. Increasing the tempe-
rature also increases the relative intensity of the (e, A^O) transition over the (D^O, A^O)
since the free carrier population is increased and the number of donors available is

reduced by thermal ionization. At T ~ 92 K, peak A (due to donor-acceptor pairs) becomes very weak. With further increasing temperature, peak A completely disappears. This behaviour is characteristic of (D^O, A^O) recombination[3.20] and comes about due to the thermal ionization of the shallower impurity. However, if peak A is free-carrier-associated, it should not disappear at higher temperatures. Furthermore, if it is due to localized transitions, it should get stronger with temperature because localized electrons will be delocalized gradually. These further confirm the identification of the low-temperature emission of $Al_{0.48}In_{0.52}As$ as (D^O, A^O) recombination.

It is instructive to follow the variation of the $Al_{0.48}In_{0.52}As$ emission with temperature in the indirect-related transition regime $(p > p_c)$. In Fig. 3.11 we show the temperature variation of the luminescence under p = 92 kar. At T = 2 K, we see the narrow emission peak A' and the broad emission peak B'. Emission B' is probably from a DX-like centre since it is insensitive to increasing pressure when $p > p_c$. Peak A' corresponds to (D^O, A^O) recombination in $Al_{0.48}In_{0.52}As$ as discussed earlier. As the temperature is increased only to 24 K, peak A' becomes unobservable. Comparing Fig. 3.11 with Fig. 3.10, we can see that the (D^O, A^O) emission in the indirect-band gap is much more dependent on the temperature than that in the direct-band gap.

This temperature behaviour is characteristic of (D^O, A^O) recombination in an indirect-band transition: For an indirect-gap semiconductor, the intrinsic recombination probability of the electrons and holes is low, because of the restriction on the crystal momentum. However, the recombination of the electrons and holes can be greatly enhanced by addition of impurities which interact strongly with free carriers, enabling crystal momentum to be conserved through an impurity-carrier interaction. Thus we can think of the impurity inducing an efficient luminescence. With increasing temperature to 24 K, the intensity of emission A drastically decreases, which is related to the fact that trapped electrons and holes have an appreciable probability of being thermally released

from acceptors and donors at higher temperatures combined with the relatively low transition probabilities of donor-acceptor-pairs.[3.21] For instance, at 4 K, the efficiency of the (D^0, A^0) transition in GaP is close to 100 %. However, at room temperature (300 K) the quantum efficiency is less than 0.01 %.[3.13]
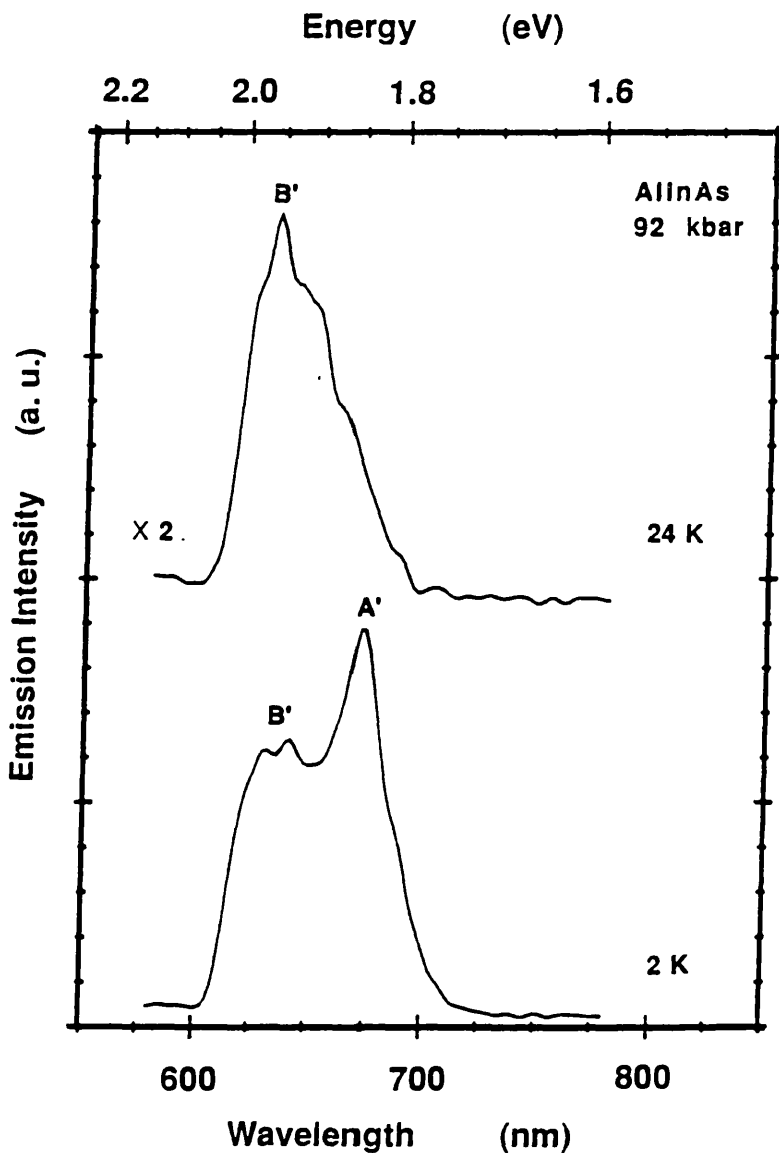
Fig. 3.11. Temperature dependence of the $Al_{0.48}In_{0.52}As$ emission A' at 92 kbar (p > p_c). As the temperature is increased only to 24 K, peak A' becomes unobservable.

Moreover, the (D^O, A^O) recombination mechanism can well explain the experimental results as shown in Fig.3.4: why the emission intensity of the low-temperature PL spectra of $Al_{0.48}In_{0.52}As$ does not decrease rapidly when the emission is changed from the direct-related transition to the indirect-related one by applying high pressure at low temperature. It is just because such an impurity-induced emission produces efficient light generation in the indirect-gap case at low temperature. The recombination mechanism involving simple donors and acceptors can be very efficient at low temperature, though they do not produce efficient light emission at higher temperature.

Therefore, as mentioned above, the observed temperature dependence of the direct-related and the indirect-related emission spectra can be very well explained by the $(D^O,$ $A^O)$ recombination, but not by free-carrier-associated or localized transitions.

3.3.4.   Photoluminescence Excitation

The use of photoluminescence excitation (PLE) is most powerful for (D^O, A^O) transitions in which unresolved emission can then potentially show the fine structure described by equation (3.4). In this work we have examined the PLE spectra of donor-acceptor pairs (D^O, A^O) in $Al_{0.48}In_{0.52}As$ under both pressures $p < p_c$ and $p > p_c$ and found two excitation processes for the (D^O, A^O):

(1) the excitation of an electron to the conduction band, leaving a hole in the 1S state of the acceptor, i.e., $(D^+, A^-) \rightarrow \{D^+, A(1S)\} + e$;

(2) the band-to-band excitation, free holes and electrons are created when the incident photon energy is greater than the band-gap energy. Such electrons and holes are eventually trapped by the donors and acceptors, respectively, and produce the neutral donor-acceptor pairs (D^O, A^O).

In Fig. 3.12 we show the PLE spectrum at 45 kbar ($p < p_c$), compared to the PL spectrum taken at the same pressure. The emission peaking at 1.8902 ± 0.0002 eV is due to (D^O, A^O) recombination, and the transition peaking at 1.9636 ± 0.0002 eV is the band-to-band which gives the band gap E_g. The emission peaking at ~ 20 meV lower than E_g is probably due to bound excitons. A large shift of $\sim 73 \pm 0.2$ meV between the PL and the PLE spectra can be observed. The threshold energy is 1.896 ± 0.0002 eV. The large shift of ~ 73 meV between the PL and the PLE spectra virtually rules out the emission peaking at ~ 1.8902 eV being due to bound excitons.
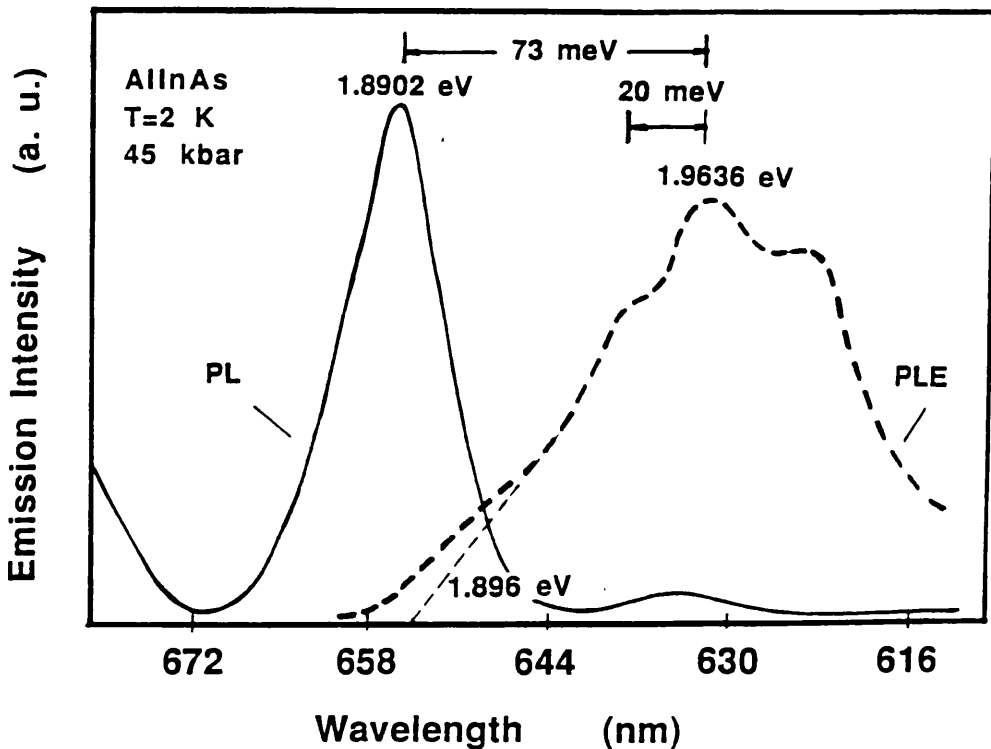
Fig. 3.12.   At 2 K, the PL and PLE spectra of $Al_{0.48}In_{0.52}As$ under 45 kbar ($p < p_c$). The emission peaking at ~ 1.8902 eV is due to (D^O, A^O) recombination, and the band-to-band transition peaking at ~ 1.9636 eV gives band gap E_g at this pressure. The large shift of ~ 73 meV between the PL and the PLE spectra can be observed. The threshold energy is ~ 1.896 eV.

The PLE spectrum shows a broad excitation band peaking at ~ 1.9636 eV. This excitation process is $(D^+, A^-) \rightarrow \{D^+, A(1S)\} + e$, which satisfies the following condition:

$$E_g - E_A + e^2 / \varepsilon r < \hbar \omega_e, \qquad (3.6)$$

where E_g is the band gap, E_A is the acceptor binding energy and $\hbar \omega_e$ is a given photon energy. Here we assume that $E_A > E_D$. Hence, from equation (3.6) the threshold energy of the observed broad excitation band for the very distant pairs $(r \rightarrow \infty)$ corresponds to the energy difference between the bottom of the conduction band and the acceptor ground state $E_g - E_A$ and can be ascribed to (e, A^O) transition. Therefore E_A can be estimated if E_g is known.

In Fig. 3.12 the PLE spectrum shows that the band-to-band transition occurs at 1.9636 ± 0.0002 eV at 45 kbar. The emission threshold of 1.896 ± 0.0002 eV was obtained by extrapolating the curve to zero as previously done by Nakashima et al.[3.17] Then the acceptor binding energy E_A is found to be ~ 67.6 meV. This implies that the emission from our $Al_{0.48}In_{0.52}As$ sample is due to "deep" (D^O, A^O) transitions. This has important implications when estimating E_g from PL spectra and for the magnitude of confinement calculated in superlattice structures.

Because at 45 kbar the acceptor binding energy E_A and the energy difference between the band gap E_g and the (D^O, A^O) emission are ~ 67.6 meV and ~ 73.4 meV, respectively, the donor binding energy E_D is ~ 5.8 meV. Considering that the donor binding energy in the hydrogenic model is given by:

$$E_D = 13.6 \, (1 / \varepsilon)^2 \, (m_e^* / m_o) \quad \text{(eV)}, \qquad (3.7)$$

where ε is the dielectric constant, m_O is the electron mass, m_e^* is the effective mass of the electrons in the Γ-valley. For $Al_{0.48}In_{0.52}As$, m_e^* and ε are 0.0755 m_O and 12.7, respectively. Substituting them into equation (3.7), we get $E_D \sim 6.4$ meV. Therefore, our experimental result (5.8 meV) is compared to the calculated one (6.4 meV).

It is worth noticing that: because emission B and the (D^O, A^O) emission A have almost the same pressure coefficients (see Fig. 3.2), the energy difference between these two emission bands is about constant ~ 70 meV with increasing pressure. This suggests that emission B is very near the band edge in energy (~ 3 meV) for $p < p_c$. Hence, it is reasonable to assume that the pressure dependence of emission B approximately represents that of the direct-band gap. One significant observation is that within experimental uncertainty the donor-acceptor-pair (D^O, A^O) band exhibits the same pressure dependence as the direct-band gap for $p < p_c$.

Considering that the acceptor binding energy does not vary relative to the valence band under pressure,[3.22] we get the simple results that the donor level associated with the (D^O, A^O) emission is quite rigidly attached to the conduction band in this $Al_{0.48}In_{0.52}As$ alloy system and the variation in the donor binding energy with the pressure seems to be minor in the $p < p_c$ region within experimental uncertainty. Our result does not suggest that the relative increase in the effective mass, m^*, is approximately proportional to the relative increase in the direct-band gap E_g.[3.3] This observation is analogous to that reported by Onton et al.[3.23] They found that the (D^O, A^O) band follows the same alloy composition dependence as the band gap.

Fig. 3.13 shows the PLE and PL spectra at 59 kbar ($p > p_c$). The band-to-band transition peaking at 2.0114 $\pm$ 0.0002 eV and the (D^O, A^O) emission peaking at 1.9375

± 0.0002 eV were observed in this indirect transition as those in the direct transition. The emission peaking at 1.9904 ± 0.0002 eV is probably due to bound excitons. However, it is some what surprising that the energy shift, ~ 74 meV, between the PLE and the PL spectra in this indirect case is almost the same as that in the direct one of ~ 73 meV (see Fig. 3.12). The PLE spectrum is found to shift rigidly with the pressure.
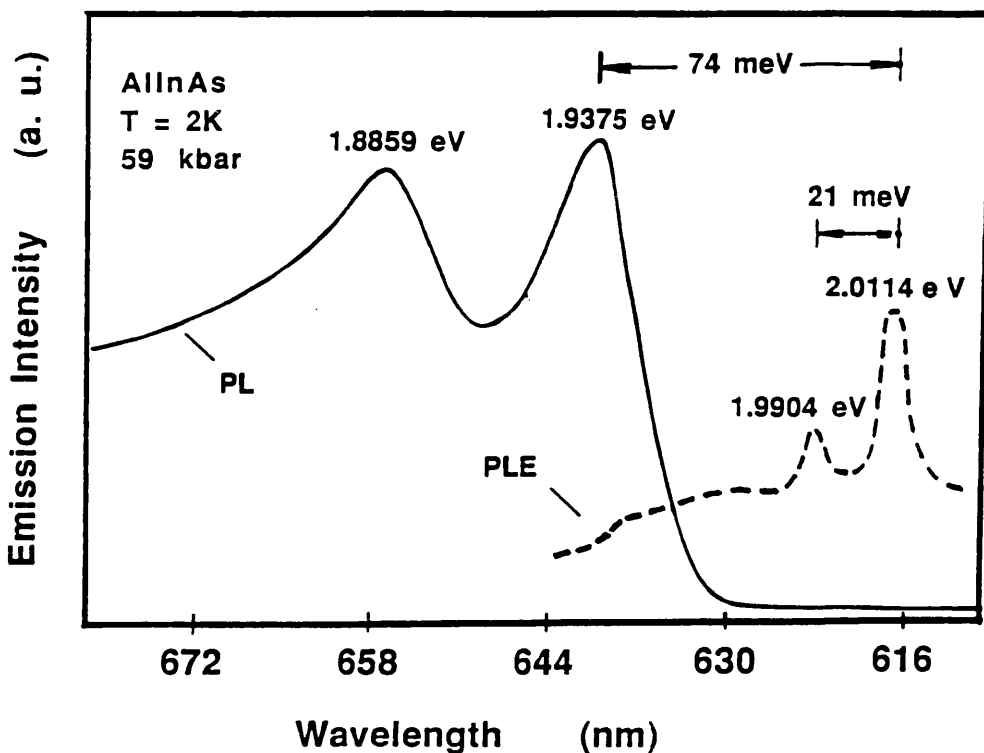
Fig. 3.13.   At 2 K, photoluminescence (D^O, A^O) and PLE of $Al_{0.48}In_{0.52}As$ under 59

kbar ($p > p_c$). The emission peaking at 1.9375 ± 0.0002 eV is due to (D^O,

A^O) recombination, the peak at 1.8859 ± 0.0002 eV is from InP substrate.

The band-to-band transition peaking at 2.0114 ± 0.0002 eV is the band

gap E_g. The emission peaking at 1.9904 ± 0.0002 eV is probably due to

bound excitons. The shift between the PL and the PLE spectra is ~ 74

meV.

Because the effective mass of electrons related to the X-valley is generally larger than that in the Γ-valley, the donors associated with the X-valley should be deeper than those associated with the Γ-valley. Thus, at direct-indirect crossover an abrupt change should occur in the binding energy of the donor participating in (D^O, A^O) transitions.[3.24] Considering that the direct or indirect nature of the (D^O, A^O) recombination involves only the nature of the donor, therefore, the separation between the PL and the PLE spectra should increase abruptly as the material becomes indirect. If considering that the binding energy of the donors are ~ 5 and ~ 50 meV, respectively, for the direct- and the indirect-band gaps, we should observe an increase of ~ 45 meV in the shift between the PLE and the PL spectra. However, it is in contrast to our observations. Our results indicate that the variation of the donor binding energy in going from a direct- to an indirect-conduction band is not noticeable. We therefore suggest that the hydrogen-atom model may need modification to the donor energies in $Al_{0.48}In_{0.52}As$.

3.4. Summary

Until this work was completed no detailed studies of the low-temperature luminescence of $Al_{0.48}In_{0.52}As$ under high pressures were available to the best of our knowledge. We investigated the low-temperature PL and PLE spectra characteristics of $Al_{0.48}In_{0.52}As$ under high pressure from 1 bar up to 92 kbar.

At low temperature, the main change in the appearance of the spectrum, as the sample goes from a direct gap to an indirect gap, is the abrupt variations of the pressure coefficients at ~ 52.5 ± 0.5 kbar. However, the emission intensity does not change drastically. The linear pressure coefficient α^Γ of the (D^O, A^O) band related to the Γ minimum in the conduction band of $Al_{0.48}In_{0.52}As$ was found to be 7.9 ± 0.1 meV/kbar, which is almost the same as that of bulk InAs (8 meV/kbar),[3.9] but

significantly lower than that of $Al_{0.48}In_{0.52}As$ at higher temperature.[3.7]   The linear

pressure coefficient α^X of the (D^O, A^O) band related to the X minimum in the

conduction band was found to be $- 2.9$ meV/kbar, which is close, but not equal to that

of bulk GaAs ($- 1.8$ meV/kbar at 110 K).[3.10]

We observed the band-to-band and the bound-to-free transitions in the PLE spectra

and found a large shift between the PL and the PLE spectra, ~ 74 meV. By investigating

the temperature and excitation-power dependences of the PL spectra together with the

PLE spectra, we suggested that the low-temperature emission of the $Al_{0.48}In_{0.52}As$ is

not from bound exciton, free-carrier-associated and localized transitions, but due to

(D^O, A^O) transition with a relatively deep acceptor of ~ 68 meV in both the direct- and

the indirect-related bands. The transition of the (D^O, A^O) band from a direct-pair band

to an indirect one (i.e., a pair band that follows the indirect-conduction band) occurs

abruptly within the resolution of the present data. In the intermediate range 50 kbar < p

< 55 kbar, direct (D^O, A^O) recombination occurs together with indirect pair

recombination.

We also found that the emission intensity of the indirect (D^O, A^O) transition is more

dependent on the temperature than that of the direct (D^O, A^O) transition in this

$Al_{0.42}In_{0.52}As$ sample, in agreement with previous (D^O, A^O) studies in indirect gap III-

V semiconductors.

Finally, we suggest that the shallow donor ground states associated with the X- and

the Γ-conduction bands seem to be tied quite rigidly to these conduction bands since

variations in the donor binding energies with the pressure and the direct-indirect

crossover seemed to be minor.

- 88 -

Ch. 4. OPTICAL PROPERTIES OF GaAs/GaP

STRAINED-LAYER SUPERLATTICE

page

4.1. Introduction

In 1970 Esaki and Tsu[4.1] first proposed fabricating superlattices (SLs) from alternating layers of semiconducting materials. Since then a variaty of SLs have been grown.[4.2] Because of their technological importance and scientific interest, SLs have been widely investigated both experimentally and theoretically.

Although early work focused on lattice-matched QWs and SLs, recent studies have begun to explore the possibilities offered by the large number of lattice-mismatched superlattice systems that are available.[4.3] These kinds of superlattices are called strained-layer superlattices (SLS), such as GaP/GaAsP and the GeSi/Si SLS.[4.4, 4.5] The flexibility in the choice of SLS layer materials and the interesting effects of the large elastic layer strains allow SLS materials to exhibit a wide range of tailorable properties which are of interest for scientific and device purposes.

Fig. 4.1 shows the schematic of an SLS. In SLS materials the individual layers are under tensile or compressive strain, depending upon the relative size of the lattice constants of the layers. The accumulation of elastic energy in the layers with increasing thickness will eventually result in lattice relaxation, which leads to interface-misfit dislocations.[4.6] For most device applications, it is important that these lattice-mismatched layers are coherently strained, i.e., pseudomorphic with respect to each other.[4.7] Modern crystal-growth techniques have made it possible to grow high quality strained layers,[4.8] which are thin enough so that the mismatch is totally accommodated by built-in coherent strains rather than by misfit dislocations.

One particular case of interest is the GaAs/GaP superlattice. This system is similar to GaAs/AlAs (both AlAs and GaP are indirect gap materials). The principal difference

between both systems is the strain present in the former case because of the much larger lattice mismatch between GaAs and GaP. Therefore, GaAs/GaP is a SLS. Strain distribution in the constituent layers depends on the respective layer thickness. This results, together with the variation in the magnitude of the confinement due to the different thicknesses of the GaAs and GaP layers, in a very large diference in band structure from one sample to another.

STRAINED-LAYER SUPERLATTICE
(SLS)

Thin, mismatched
layers

Superlattice: mismatch
accommodated by
strain

Graded layer

Substrate
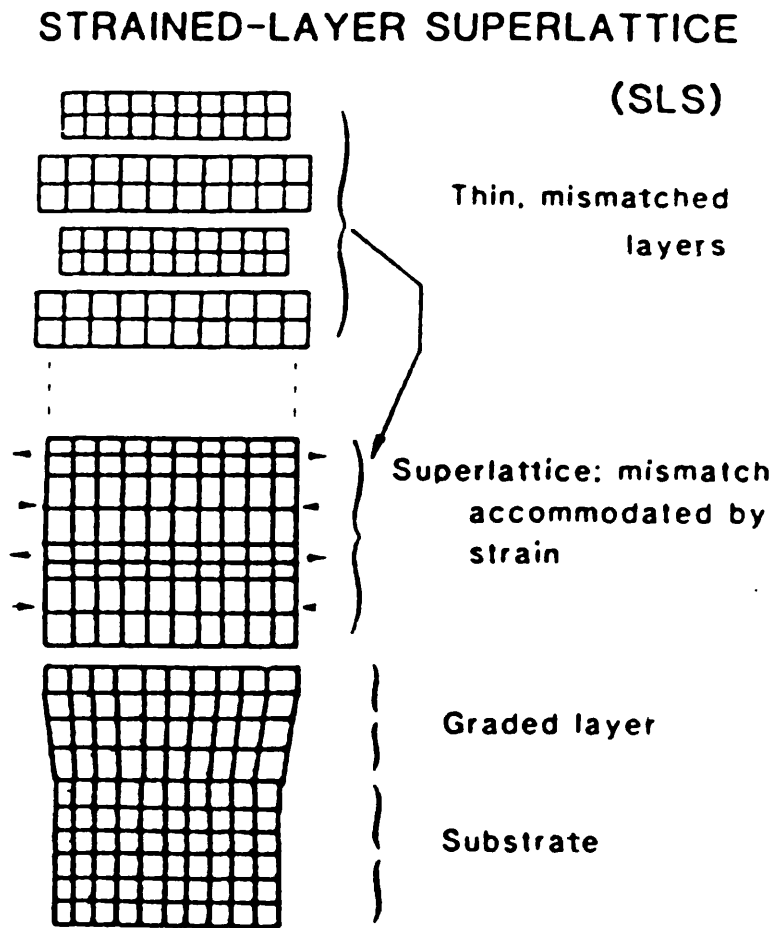
Fig. 4.1. Schematic of an SLS.

In addition, we can think that, for certain layer thicknesses and strain levels, the lowest confined electron state of this system may come from the X minimum of GaP, therefore, electrons will be confined in the GaP layers and holes in the GaAs layers,

which results in indirect (type-II) transitions in real space. On the other hand, electrons and holes at their lowest energy level may be all located in the GaAs layers, which gives rise to direct (type-I) transitions. For this kind of SLS, the combination of an emission-related technique and an absorption-related technique is required in order to identify the origin of the observed transitions. The reason is that, in these type-II SLs, two different kinds of transitions are observed. The lowest energy transition, which is the spatially indirect one (its oscillator strength is very small due to the small overlapping of the electron and hole wave functions), is observed by means of the emission-related technique, while the lowest direct transitions are observed with the absorption-related technique.

GaAs/GaP strained-layer superlattices are the limit case, with x = 1 and thus maximum lattice mismatch, for the system $GaP/GaAs_xP_{1-x}$. Optical studies of this kind of highly strained-layer GaAs/GaP superlattices grown on GaAs substrates have been previously reported.[4.9, 4.10] In this work, we investigated the optical properties of a type-II GaAs/GaP strained-layer superlattice grown by atomic layer molecular-beam epitaxy (ALMBE) on GaAs substrate. Photoluminescence (PL) and photoluminescence excitation (PLE) measurements were carried out. By combining these two techniques and the PL evolution as a function of temperature and excitation power, we attempted to identify the origin of the observed transitions.

4.2. Energy Band Structure of GaAs/GaP SLS

In principle, the electronic structure of GaAs/GaP SLS should be similar to that of GaAs/AlAs ones, because both of them are constituted by one indirect larger-gap and one direct smaller-gap material. However, strain, as a new parameter appearing in these SLSs, will modify substantially the optical properties and band structure. In Fig. 4.2 a schematic description of the effects of the stress in the two constituent bulk materials is presented.[4.10]
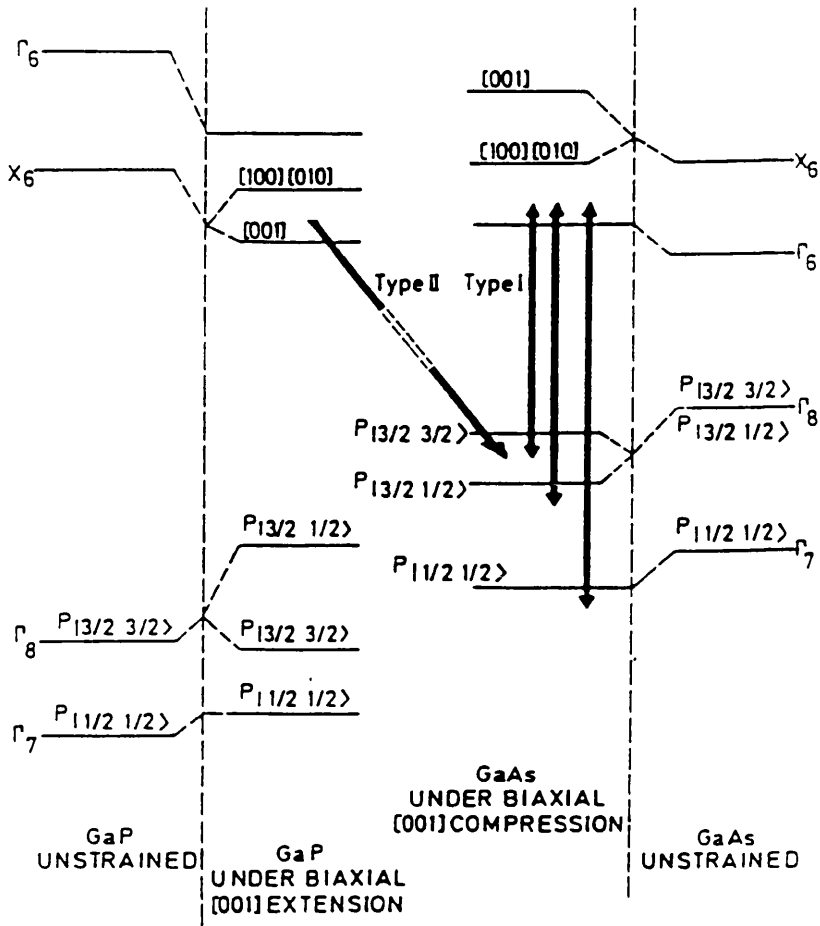
Fig. 4.2. Schematic band diagram of strained and unstrained bulk GaAs and bulk GaP. Arrows indicate the type-I and type-II transitions.[4.10]

In an unstrained zinc-blende semiconductor material, at the Γ point the valence-band states are comprised of a fourfold $P_{3/2}$ multiplet (J = 3/2, m_j = ± 3/2, ±1/2) and a $P_{1/2}$ doublet (J = 1/2, m_j = ± 1/2). Because the lattice constants of GaAs and GaP are 0.5653 nm and 0.5451 nm, respectively, the lattice parameter mismatch can induce biaxial stresses that can be resolved into two parts:

i) a hydrostatic pressure component, which increases or decreases the band gap for compression or extension, respectively;

ii) a shear strain component, which removes the valence band degeneracy at k = 0 by including a split in the heavy and light hole energy states.

The application of a biaxial stress shifts $P_{3/2}$ and $P_{1/2}$ in energy with respect to the conduction band, splits the $P_{3/2}$ multiplet in two doublets (J = 3/2, m_j = ± 3/2 and J = 3/2, m_j = ± 1/2), and couples light-hole and split-off bands. Strain effects in the X-states have to be taken into account for the type-II SLS. Under a biaxial stress in the (001) plane the degeneracy of the three equivalent X-minima in the [001], [010], and [100] directions is lifted and the band is shifted as a whole.

The GaP X-level lies at lower energy than the GaAs X point. Therefore, the GaP layers will be a well for X-type states and the GaAs layers will be a well for Γ-type states. Because the strain levels depend on the relative and absolute thicknesses of GaAs and GaP layers, the lowest exciton state can originate either from Γ electron states of GaAs wells or from X-point electron states of GaP barriers.

Hence, one may expect that for certain values of period, composition and strain level, these SLS will be type-I (lowest gap is spatially direct with electrons and holes at Γ-point in GaAs layers), and those for other values will be type-II (lowest gap spatially indirect with electrons confined in GaP layers at states coming from the folding of the bulk X-states and holes at Γ-point in GaAs layers).

Due to the anisotropy of the X-minima in GaP, two different subbands are obtained for the lowest GaP conduction-band states. In structures grown in the [001] direction, the heavy longitudinal mass m_l is the quantization mass for the minima aligned along this growth direction (X_z), whereas the light transversal mass m_t is the quantization mass for the X_x- and X_y- minima aligned along the [100] and [010] directions, respectively. Thus the lowest confined X sublevel located in the GaP layer should be an X_z-state. Because of the mixing of X_z-states with Γ-states by the SL potential the quasi-direct transition without the participation of momentum-conserving phonons becomes partially allowed for X_z excitons.[4.11, 4.12]

The coupling between bands related to two different points in the Brillouin zone can be experimentally studied using optical spectroscopy. Optical studies are interesting because for indirect superlattices the transitions are not only indirect in momentum space (k-space, Γ-X transitions) but also in real space. The lowest-energy band gap of these type-II superlattices is determined by transitions involving the spatially separated Γ valence band states of the GaAs and the confined X-conduction band states of the GaP, as schematically depicted in Figure 4.2. The respective oscillator strengths of these Γ-X or type-II transitions, however, are very small compared to those of the direct Γ-Γ or type-I transitions at higher energy because they are indirect in real and k-space.

4.3. Experimental Details

4.3.1. Samples

The samples used in this work are $(GaAs)_6/(GaP)_n$ (n = 2, 4, 6) strained-layer superlattices grown on n-doped (001) GaAs substrate by atomic layer molecular beam epitaxy (ALMBE)[4.13] at the National Centre for Micro-electronics at Madrid, Spain. The substrate temperature was 425 $^{\circ}$C. X-ray diffraction and Auger electron spectroscopy measurements provided structural characterization of the samples. Raman scattering gave the strain level accommodated in the GaAs and GaP layers. Table 4.1 shows the parameters of the samples, here d_{GaAs} and d_{GaP} are the slab thicknesses, ε_{GaAs} and ε_{GaP} the strains accommodated in the GaAs and GaP layers, respectively. The total thickness of the samples is ~ 0.4 μm.[4.10] Because $(GaAs)_6/(GaP)_n$ (n = 2, 4) showed optical emissions only from bulk GaAs and bulk GaP, othet than from SL stuctures, we mainly studied sample $(GaAs)_6/(GaP)_6$. The schematic diagram of (GaAs)/(GaP) is plotted in Fig. 4.3.

Table   4.1 Sample parameters.

Sample	Period (A)	d_{GaAs} (A)	d_{GaP} (A)	ε_{GaAs} (%)	ε_{GaP} (%)
$(GaAs)_6/(GaP)_2$	22.3	16.7	5.6	0	3.7
$(GaAs)_6/(GaP)_4$	27.2	16.2	11.0	0.7	3.0
$(GaAs)_6/(GaP)_6$	32.4	18.4	14.0	1.4	2.3
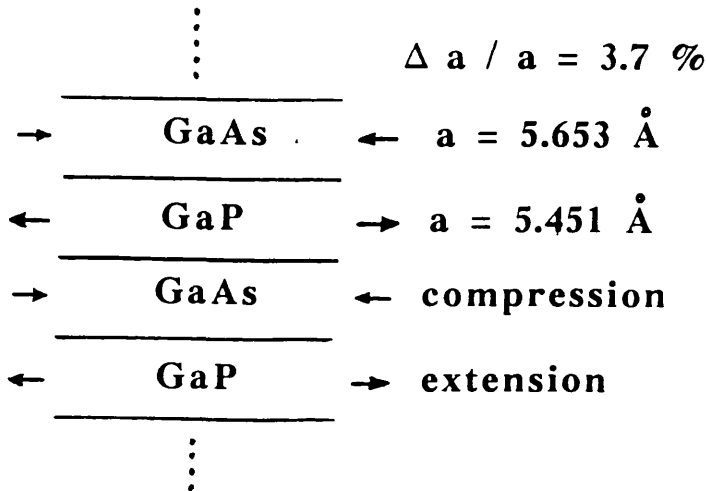
Fig. 4.3. Schematic diagram of $(GaAs)_6/(GaP)_6$.

4.3.2   Experiments

The sample was characterized by PL and PLE. For PL measurements, the sample was placed in a variable-temperature cryostat cooled by liquid helium, using as an excitation beam the 488.0 nm line of an Argon ion laser. Emitted light was analyzed with a 1m double monochromator and a cooled GaAs photomultiplier, coupled to a photon-counting system. PLE measurements were obtained at 75 K using a dye DCM: 610 -720 nm in the dye laser pumped by the Argon ion laser.

4.4. Optical Properties of GaAs/GaP

4.4.1. PL and PLE Spectra of GaAs/GaP

Fig. 4.4 shows the PL spectrum of sample $(GaAs)_6/(GaP)_6$ and the corresponding PLE spectrum at the same excitation power and temperature of 75 K. The detector for the PLE spectrum was set at the energy of peak A.
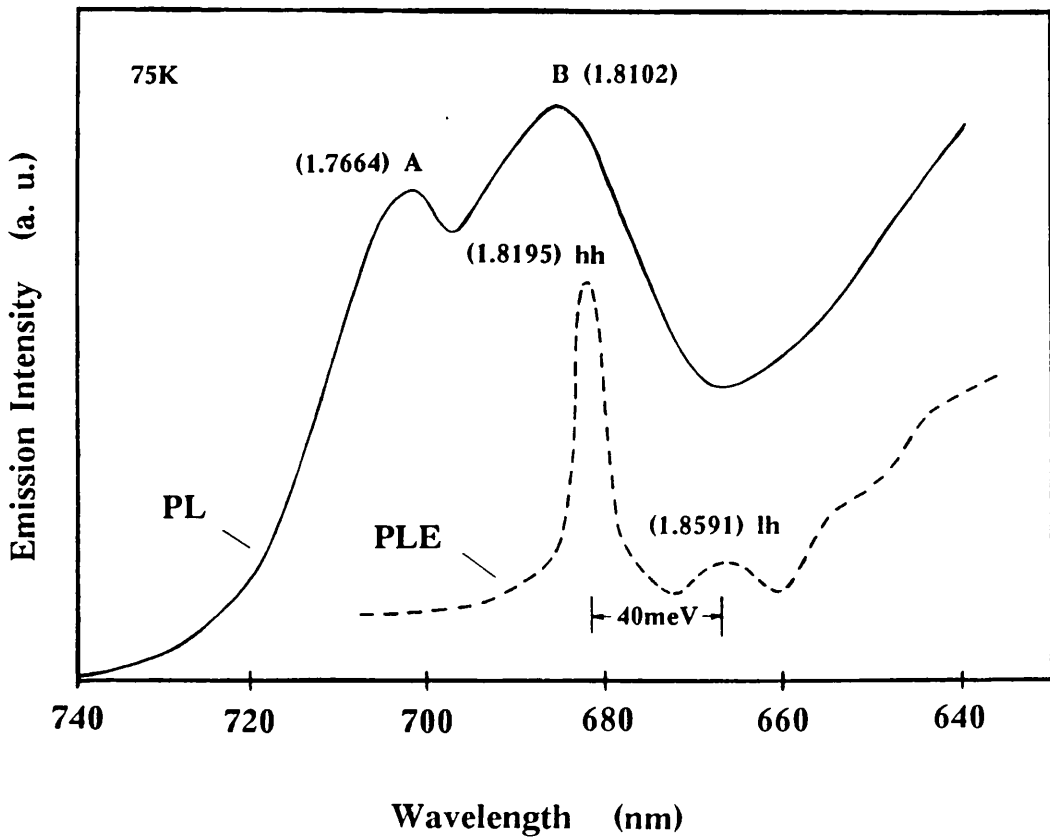
Fig. 4.4. The PL spectrum of sample $(GaAs)_6/(GaP)_6$ and the corresponding PLE spectrum at 75 K. The PLE spectrum was detected at the energy of peak A and shows the direct transition which coincides with the higher energy peak B. The numbers in brackets are the energy peak positions in eV.

In the PL spectrum, two peaks A (1.7664 eV) and B (1.8102 eV) are observed at 75 K. Their line widths have an inhomogeneous nature and most likely result from layer thickness fluctuations. As a result, localization of excitons or carriers can be expected for this short-period SLS at low temperatures. The localization of excitons is confirmed by the temperature dependence of the line shift discussed later in Section 4.4.3.

The PLE spectrum detected at the energy of peak A shows a sharp increase at higher energy with a maximum at ~ 1.8195 eV. We can assign the sharp increase in PLE to the onset of the allowed transition into the Γ-electron state of the SLS. The PLE spectrum shows the direct transitions involving Γ-electrons and holes and reveals the n = 1 heavy- and light-hole excitons at ~1.82 and ~1.86 eV, respectively. The main emission B (1.8102 eV) in the PL is Stokes-shifted by ~ 9 meV with respect to the sharp peak (1.8195 eV) in the PLE and can be attributed to the Γ-related transition. Such an interpretation of the emission spectrum is confirmed by the study of the excitation power and temperature dependences of luminescence, which will be presented later in Sections 4.4.2 and 4.4.3, respectively.

After photoexcitation of electrons and holes in the Γ-related conduction- and valence-band states, some electrons relax down to the lowest confined Γ-state of the GaAs layer. Recombination with heavy holes leads to the broad type-I luminescence peak B in Figure 4.4. Since this transition has a large oscillator strength it is dominant in the absorption spectrum and is visible in emission even though the conduction Γ-subband in GaAs is only weakly populated with photocreated carriers.[4.14]

However, some of the photocreated hot Γ-electrons may also scatter to the X-

related states before they relax down to the lowest confined Γ-state. This competing relaxation channel becomes important if the Γ-X transfer rate and the intravalley relaxation rate are comparable.[4.15]   In Fig. 4.4 the luminescence peak A at lower energy corresponds to indirect Γ-X transition. This indirect transition is not observable in the quasi-absorption (excitation) experiment because of the weak oscillator strength, but it is detectable in emission since the X-subband in GaP is the lowest energy state and thereby mostly populated under optical excitation. The energy distance between the Γ-related states in GaAs layers and the X-related states in GaP layers is ~ 44 meV. Therefore, $(GaAs)_6/(GaP)_6$ is a type-II SLS.

We would like to point out that the strength of the indirect type-II luminescence compared to the direct type-I luminescence provides strong evidence for an efficient spatial transfer of electrons from the Γ-related states in the GaAs layer to the X-related states in the GaP layers. A remarkable feature of the luminescence spectra is their evolution with the excitation intensity and temperature. In the following, we focus on the experimental investigation of this feature.

4.4.2.   Excitation Power Dependence

Figure 4.5 shows the evolution of the PL spectrum with increasing excitation power at constant temperature 75 K from the type-II $(GaAs)_6/(GaP)_6$ strained-layer superlattice. The high-energy luminescence peak B represents the Γ-Γ transition and the low-energy peak A is the X-Γ transition. The relative intensity of the two peaks depends on the temperature and excitation power. At low excitation power, peaks A and B have about the same emission intensity. However, with increasing excitation power the emission intensity of peak B becomes stronger. When the power is high enough, peak A saturates and only peak B is observed.

This excitation power dependence of the PL spectra can be adequately explained by considering saturation of the X-state. In the type-II SLS system, the Γ-electron state in the GaAs layers has higher energy than the X-electron state in the GaP layers, so that the Γ-electrons in the GaAs are scattered to the X-electron states across the interface. Real-space charge transfer takes place in the ultrafast, subpicosecond or picosecond time domain depending on the penetration depth of the Γ-electron wavefunction into the barrier layers.[4.16]
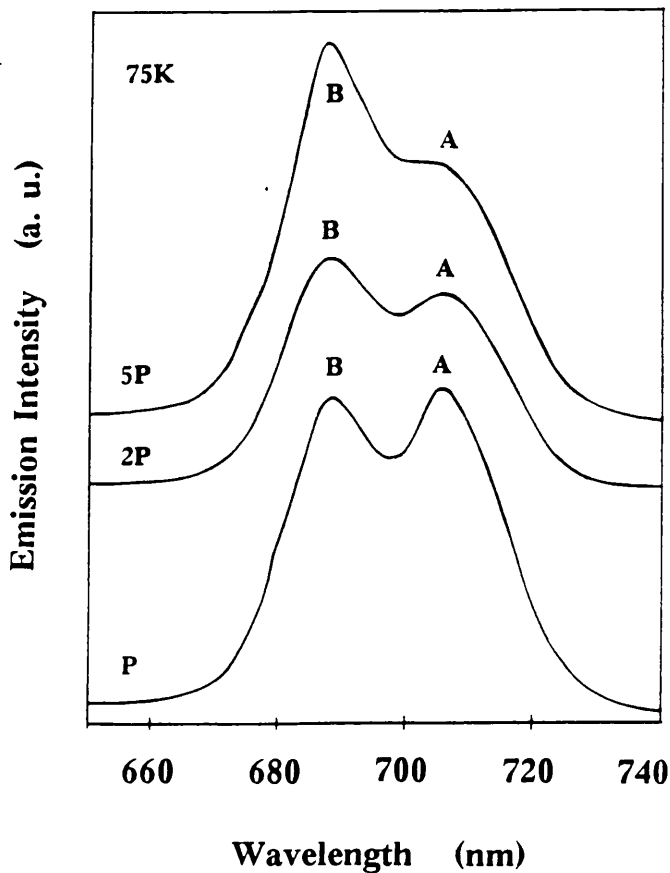
Fig. 4.5. Photoluminescence spectra from the superlattice of $(GaAs)_6/(GaP)_6$ at constant temperature 75 K, for three different excitation levels. The high-energy peak B represents the Γ-Γ transition and the low-energy peak A the X-Γ transition.

The scattered X electrons in the GaP layers recombine with the Γ heavy holes in the GaAs layers. The lifetime of the indirect emission ranges from submicrosecond to millisecond depending on the degree of the Γ-X mixing, bath temperature and sample quality.[4.17-4.19] On the other hand, the Γ-Γ luminescence lifetime is comparable to the Γ-X scattering time.[4.16, 4.20]

Therefore, after a considerable amount of real-space charge transfer takes place, some electrons distribute themselves in the GaP layers and holes in the GaAs layers. Because the lifetime of the Γ-Γ luminescence is much shorter than that of the X-Γ luminescence, the X-Γ luminescence is saturated and the Γ-Γ luminescence increases above certain excitation power. In this case, the Γ-Γ recombination is the main relaxation process of the photo-excited carriers and the lifetime of the Γ-Γ recombination increases. The saturation of the X-Γ luminescence intensity suggests that an upper limit of the carrier density at the X-point exists.

4.4.3. Temperature Dependence

Now we consider the effect of temperature variation upon the PL intensity in this type-II SLS. In Figure 4.6, we present the evolution of the PL spectra with temperature at a constant excitation power for the same sample used in Figure 4.5. In the PL spectra of the type-II $(GaAs)_6/(GaP)_6$ SLS, the higher energy peak B is assigned to the type-I recombination because the peak energy is very close to that of the main PLE peak at 75 K (Figure 4.4), while the lower energy peak A corresponds to the type-II recombination.

As shown in Figure 4.6, at 4 K only peak B is clearly observed and peak A is

almost unobservable. However, when we increase the temperature up to ~ 50 K, peak A becomes distinguishable on the low energy side of peak B. If the temperature is raised further, the two peaks become almost equally intense, and at 100 K the low-energy peak A dominates.
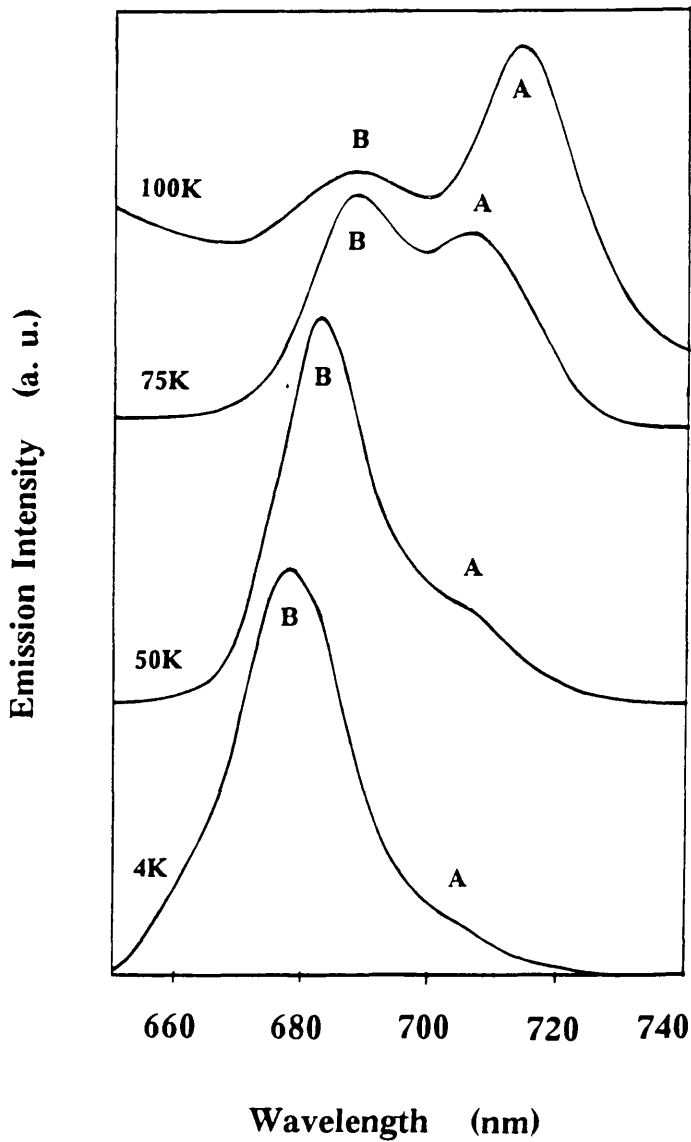
Fig. 4.6. PL spectra from the superlattice of $(GaAs)_6/(GaP)_6$ under a constant excitation power and four different temperatures. The higher energy peak B represents the Γ-Γ transition and the lower energy peak A the X-Γ transition.

In Fig. 4.6, it is also clear that the energy of peak B decreases with increasing temperature, which follows the normal temperature shift of the band gap. However, the energy of peak A shifts only slightly with increasing temperature, and only at temperatures higher than 75 K follows the expected temperature dependence of the band gap. The anomalous temperature shift of the X-related emission indicates that the X excitons are localized at low temperature.[4.21] Furthermore, the increase of emission intensity of peak A with the increase of the temperature reflects the thermal delocalization of X-states.[4.22]

From Fig. 4.6 we find that the ratio of the integrated type-I-PL intensity $I(\Gamma-\Gamma)$ to the type-II-PL one $I(\Gamma-X)$ decreases with increasing temperature. This temperature dependence of the PL intensity from this type-II SLS is opposite to that observed by other researchers. For example, Recio et al (1990)[4.10] reported that for the type-II GaAs/GaP strained-layer superlattices the type-II transition is dominant below ~ 100 K, but the type-I transition becomes dominant when the temperature raises to ~ 130 K. Accordingly, the value of $I(\Gamma-\Gamma)]$ / $[I(\Gamma-X)$ would increase with temperature. The assignment of their PL peaks was aided by photoreflectance and calculations. Similar results have also been reported for the unstrained type-II GaAs/AlAs superlattices.[4.23] Nakayama et al (1990)[4.23] assumed that the temperature dependence of the emission intensity followed the relation:

$$I\,(\Gamma-\Gamma)\,/\,I\,(\Gamma-X)\,\,\propto\,\,\exp\,(-\,E_T/k_B T), \qquad\qquad (4.1)$$

where E_T is the characteristic energy of the temperature dependence and k_B is the Boltzmann's constant. They explained that the temperature dependence resulted from the population increase of the Γ-electrons in GaAs layers with raising the temperature because of the thermal distribution.

We now discuss the temperature dependence of the PL intensity from this type-II $(GaAs)_6/(GaP)_6$ SLS. In order to find an explanation for the observed decrease of the value of I ($\Gamma-\Gamma$) / I ($\Gamma-X$) with increasing temperature, we discuss in the following different mechanisms with regard to their temperature dependence.

The type-I and type-II PL intensities are functions of the carrier concentrations and the radiative recombination rate. Therefore, the $\Gamma-X$ luminescence intensity I ($\Gamma-X$) is simply related to the concentration (n_X) of photocreated carriers (electrons accumulated in the X-subband of conduction band) and the recombination time $\tau_{\Gamma X}$:[4.24]

$$I\ (\Gamma-X) = n_X\ /\ \tau_{\Gamma X}. \tag{4.2}$$

Hence, the observed results can be explained by a reduction in the lifetime $\tau_{\Gamma X}$ of photocreated carrier or an increase in the photocreated carrier density n_X with raising temperature.

It is important to keep in mind that on the one hand, the X electrons n_X in GaP layers come from the Γ-electrons in GaAs layers, because some of the photocreated hot Γ-electrons may scatter to the X-related states before they relax down to the lowest confined Γ-state. The scattering rate depends on the spatial overlap of the electron wave functions of the Γ-minimum in the GaAs layer and of the X-minima in GaP layer. With increasing temperature, the spacial overlap of the electron wavefunctions becomes more significant due to the increased electron kinetic energies. Therefore, this causes the scattering rate to increase with temperature. Hence, the $\Gamma-X$ transfer time exhibits a pronounced decrease with increasing temperature.

On the other hand, considering that the defect states related to the X-level are much

deeper than those related to the Γ-level, most of the X-electrons n_X may be captured by the strain induced defect states at low temperatures. With increasing temperature, more and more electrons which are localized at those defect states will be thermalized to the X-states in GaP layers. Therefore, it is expected that the concentration n_X increases with raising temperature.

The reduction in the recombination lifetime $\tau_{\Gamma X}$ can be interpreted as an increase of the optical matrix element. This element is proportional to the overlap integral between the Γ-related valence subband and the X-related conduction subband. Without mixing between Γ-X states, this overlap integral would be zero, therefore the observation of an optically active Γ–X transition is already indicative for such mixing. The reduction in lifetime $\tau_{\Gamma X}$ could be explained as increased Γ–X mixing, which occurs as subbands come close in energy with increasing temperature. At low temperature, the much longer recombination time $\tau_{\Gamma X}$ and the much smaller concentration n_X seem to be the reason for the type-II emission A being undetectable at 4 K.

We speculate on why the observed temperature dependence in this work is different from that reported by Recio et al (1990).[4.10] Considering that the GaAs/GaP material is a highly strained-layer SL and the lattice mismatch is 3.7 % between GaAs and GaP layers, this means that strain relaxation is a crucial problem in this kind of SLS.

Fig. 4.7 shows the PL spectra of this type-II $(GaAs)_6/(GaP)_6$ SLS measured at start and at about five months later under the same excitation power and temperature. We can see that in Fig. 4.7, the energy difference between the Γ-level of GaAs layer and X-level of GaP layer changes from ~ 51 meV to ~ 44 meV as time goes on. The inhomogeneous relaxation of strain with time and non-uniform Γ-X mixing across the

sample probably account for this. The experimental results indicate that this type-II $(GaAs)_6/(GaP)_6$ SLS is mechanically unstable. Therefore, we probably observed the strain relaxation induced optical transitions, which would be associated with defects or impurities, which may in turn be related to Γ- and X-states.

High pressure optical measurements were attempted but were not reproducible and the signals were very weak. The poor intensity may indicate again the very important role of strain-induced defects acting as non-radiative traps.
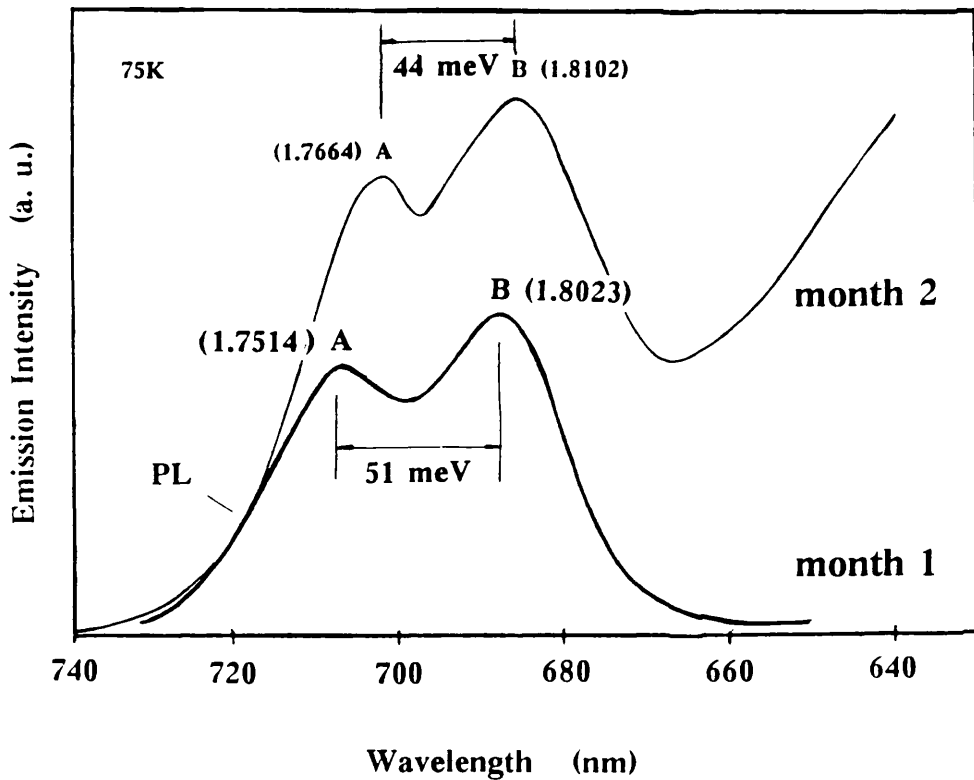
Fig. 4.7. PL spectra of $(GaAs)_6/(GaP)_6$ under the same excitation power and temperature but at different time.

4.5   Summary

We have studied the optical properties of a new mismatched system, the GaAs/GaP strained-layer superlattice, in which the lattice mismatch is 3.7%. Although the strain level induced by lattice mismatch causes large variations in the electronic band structure, type-I and type-II behaviours are still expected to take place as for GaAs/AlAs systems when the period and composition of the superlattice are varied.

The temperature and excitation density dependence of the PL spectra confirmed the assignment of the origin of the different emissions. For $(GaAs)_6/(GaP)_6$, the lowest conduction band is an X-level in GaP layers. The energy distance between the X-level in GaP layers and the Γ-level in GaAs layers is ~ 44 meV. This sample is spatially indirect (type-II) SLS. Electron transfer effects between states confined in GaAs and GaP layers were observed under suitable excitation powers and temperatures.

The temperature dependence of the PL spectrum for this type-II $(GaAs)_6/(GaP)_6$ SLS is different from previously reported results,[4.10] we probably observed, for the first time, the strain relaxation induced optical transitions, which would be associated with defects or impurities, probably related to Γ- and X-states.

Because the large lattice mismatch in GaAs/GaP systems, the systems are highly strained structures. We found that the type-II $(GaAs)_6/(GaP)_6$ SLS is mechanically unstable since the energy separation between X- and Γ-levels changed with time. The strain relaxation with time is potentially a crucial problem in this kind of highly strained systems.

Ch.5. MAGNETO-OPTICAL STUDIES OF CdTe/CdMnTe QWs UNDER HIGH PRESSURES

Page

5.1 Introduction

The field of wide-gap II-VI compound semiconductors is both old and new. Scientific research in II-VI compounds has a very long history dating back to the nineteenth century. On the other hand, from the point of view of recent optoelectronics, wide-gap II-VI compounds are quite new materials, especially as materials for light emitting diodes (LEDs) and semiconductor lasers operating in short wavelength regions.

In the late 1970's, novel technologies in crystal growth, such as molecular beam epitaxy (MBE) and metalorganic vapour phase epitaxy (MOVPE), which were developed mostly in the field of III-V compounds, were introduced to the field of I-VI compounds. As a result, crystals of high quality and purity were grown. This strongly promoted both basic and applied research and brought about a new era, what one might call a "Renaissance" in II-VI compounds. Without doubt, the recent scientific and technical developments in II-VI compounds are due to the growth techniques of MBE, MOVPE and MOMBE.

Motives for this new development came from the demand for LEDs, semiconductor lasers and other optoelectronic devices operating in the short-wavelength visible region. To fabricate such optoelectronic devices, III-V alloys (such as GaInAlP) appear to be difficult to grow, and one has to turn to II-VI compounds.

Another important point is the new, attractive physics of superlattices (SLs), quantum wells (QWs) and quantum dots (QDs) since the visible light wavelength (450 nm) approaches the size of nano-structures ~ 100 nm. The introduction of novel crystal growth technology made it possible to prepare various types of II-VI SLs and QWs.

The quest for a visible light source has culminated in the realization of the ZnSe-based diode laser in 1991 (see References. 5.1, 5.2). Therefore, it is clear that much of

the work of the II-VI community will be closely involved in the development of laser-compatible devices based on II-VI quantum structures.

From the standpoint of electronic properties, SLs and QWs based on $Cd_{1-x}Mn_xTe$ appear attractive because of the rather strong dependence of the direct optical gap on Mn concentration in this zinc-blende cubic semiconductor. At the same time, the dependence of the lattice constant of $Cd_{1-x}Mn_xTe$ on composition implies that substantial strain will exist in the structures. Thus we have a strained layer SL analogous to those already fruitfully studied in the III-V systems.

A unique aspect of $CdTe/Cd_{1-x}Mn_xTe$ and related II-VI SLs and QWs is the magnetic contribution by the Mn-ion to their electronic and optical properties. This manifests itself in "giant" spin splittings of the valence and conduction bands in external magnetic fields at low temperatures within the Mn-containing regions.[5.3] The effects originate from spin coupling between the Mn-ion d-electrons and those of the carriers.

In addition, these materials are particularly attractive candidates in which to examine the effects of changes in dimensionality (to 1- and 0-dimension) on magnetic phenomena and of quantum-confined carriers on the magnetic properties of the system. Therefore, $CdTe/Cd_{1-x}Mn_xTe$ and related II-VI SLs and QWs provide an opportunity to study quantum phenomena in a new manner.

Although the optical and electronic properties of $CdTe/Cd_{1-x}Mn_xTe$ SLs and QWs have been studied in some detail, a substantial number of questions remain concerning the basic electronic structure and properties of the systems. Compared with the more widely studied III-V SLs and QWs, notably the GaAs/(GaAl)As systems, few of the fundamental parameters necessary for the engineering of CdTe-based devices are yet known. Such parameters are particularly important in the strained layer SLs and QWs.

This chapter focuses on the optical properties of the $CdTe/Cd_{1-x}Mn_xTe$ under

hydrostatic pressures and magnetic fields. The rest of this chapter is organized as follows. In the next section we introduce the band structure of $Cd_{1-x}Mn_xTe$ alloy. In section 3 the growth of $CdTe/Cd_{1-x}Mn_xTe$ QWs is described. In section 4 we discuss the luminescence of $CdTe/Cd_{1-x}Mn_xTe$ at atmospheric pressure. In section 5 the first investigation, to our knowledge, of the pressure coefficient as a function of the QW width L_w is presented. In section 6 we report for the first time the magneto-optical spectra of $CdTe/Cd_{1-x}Mn_xTe$ QWs under high pressures. Summary remarks are contained in section 7.

5.2   Band Structure of the Wide-Gap $Cd_{1-x}Mn_xTe$ Alloy

There has been much interest recently in the diluted magnetic (or semimagnetic) semiconductors (DMS) based on the II-VI compounds. In the $A^{II}_{1-x}Mn_xB^{VI}$ alloys, manganese substitutes for the cation in $A^{II}B^{VI}$ semiconducting compounds, and is in the $Mn^{2+}3d^5$ configuration. At very low values of x (typically well below 1 atomic percent), the influence of Mn on the band structure can be disregarded, and Mn interactions with carriers can be neglected. However, when larger mole fractions of Mn (of the order of a few atomic percent or more) are alloyed with the $A^{II}B^{VI}$ host material, the situation is drastically altered. For example, the intrinsic edge may move through the visible region in wide-gap DMS.

The presence of such Mn concentrations leads to new and interesting electrical and optical behaviour due to spin-spin exchange interactions between band electrons and localized moments of the magnetic ions. $Cd_{1-x}Mn_xTe$ has been particularly widely studied and is probably the best understood of the wide-gap DMS because of its important properties which are not encountered in usual semiconductors.

5.2.1   Basic Features at Zero Magnetic Field

For wide-gap DMS $Cd_{1-x}Mn_xTe$, crystallographic studies indicate that a single phase region -- zinc blende -- exists over wide ranges of x. All results to date suggest that in this region of solid solution, the band gap is always direct. Therefore, the zone centre band structure of this material should be characteristic of zinc blende crystals. In the $A^{II}B^{VI}$ compounds, the two valence electrons of the group II element and the six electrons of the group VI elements are distribute according to the so-called s-p^3 orbital bonding configuration. In this picture, the highest-lying valence band is triply degenerate in the absence of spin-orbit splitting, and the states at the centre of the Brillouin zone are bonding combinations of functions which are p-like about the nuclei. The lowest conduction band is s-like. The introduction of the spin-orbit interaction alters the bands, principally by splitting certain degeneracies. At $k = 0$ in the zinc blende structure, the six-fold degenerate (three-fold not counting the two spin states) Γ_{15v} state splits into a four-fold Γ_8 ($J = 3/2$) state and a lower, two-fold Γ_7 ($J = 1/2$) state, with the splitting indicated in Fig. 5.1 by Δ_{so}, the spin-orbit splitting energy.[5.4]
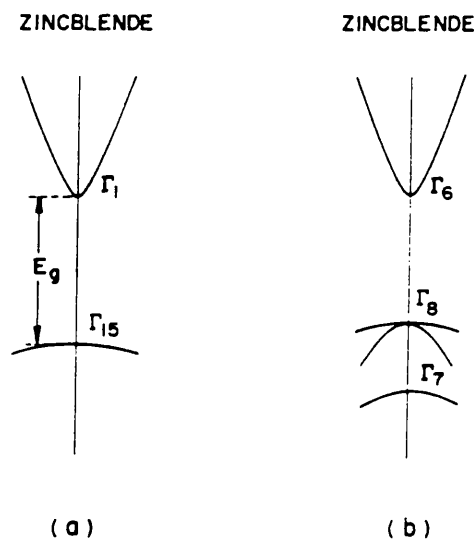
Fig. 5.1. Zinc-blende band structure for (a) $\Delta_{so} = 0$, and (b) $\Delta_{so} \neq 0$.

A review of the literature reveals distinct trends in the behaviour of the fundamental gap in DMS. There are, (1) a general increase in gap energy with Mn mole fraction x at a fixed temperature T, and (2) approximate agreement of gap energies when results are extrapolated to the same hypothetical x = 1 zinc blende MnB^{VI} compounds. This behaviour is illustrated in Fig. 5.2 for the two ternaries involving Cd and Zn and the common anion Te, and for intermediate quaternary alloys in the $Cd_xZn_yMn_zTe$ (x + y + z = 1) system.[5.5]
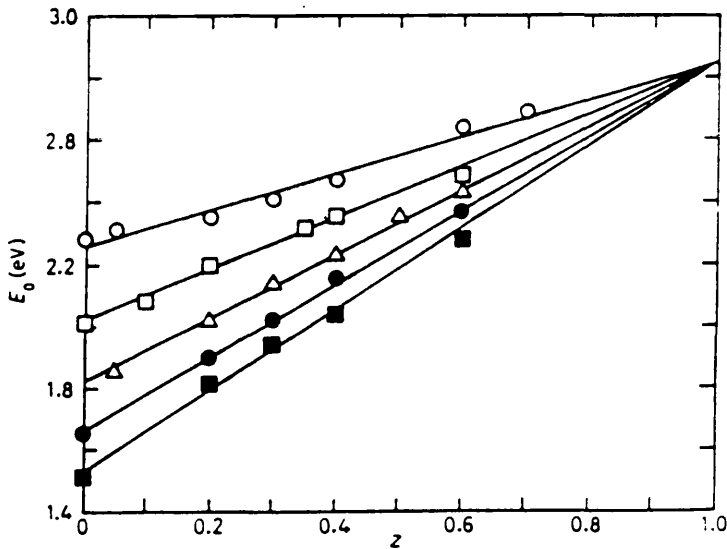
Fig. 5.2. Variation of the energy gap in $Cd_xZn_yMn_zTe$ (x + y + z = 1) with manganese concentration z for fixed x : y ratios. Experimental values: from the top line to the bottom line x = 0, 3x = y, x = y, x = 3y and y = 0, respectively.[5.5]

The linear behaviour exhibited in Fig. 5.2 is only a first order guideline to what may be expected in the various DMS alloys. Based on results for many semiconductor ternary alloy systems, a nonlinear dependence of the band gap, namely a downward "bowing" in E_g against x, would be anticipated with refined measurements on crystals of good quality.[5.6] Such bowing is thought to arise from the nonlinear dependence of the band gap on the crystal potential, and on short range fluctuations of the potential in

a random substitutional alloy.[5.7] Surprisingly, such nonlinearities, a characteristic of the complete alloy range, are noticeably absent in the wide-gap DMS.

The present experimental knowledge of the band structure of wide-gap DMS alloys is nearly gleaned from investigation of optical effects, e.g., absorption, reflectivity, photoluminescence and excitation spectroscopy. Here we review a variety of such experimental results that reveal the dependence of band structure features of $Cd_{1-x}Mn_xTe$ on Mn concentration.

Table   5.1. Summary of E_g versus mole fraction x in $Cd_{1-x}Mn_xTe$ alloy.[5.4]

E_t in eV	$T(K)$	Range of x	Measurement Methods[†]	Reference
$1.585 + 1.51x$	77	$0 < x < 0.5$	R.	Gaj et al. (1978)
$1.595 + 1.587x$	LHe	$0 < x < 0.2$	E.M.	Twardowski et al. (1979)
$1.50 + 1.44x$	300	$0 < x \leq 0.6$	E.R.	Bottka et al. (1981)
$1.586 + 1.393x$	76	$0 < x \leq 0.7$	P.	Vecchi et al. (1981)
$1.53 + 1.26x$	300	$0 < x < 0.7$	E.L.	Lautenschlager et al. (1985)
$1.528 + 1.316x$	300	$0 < x \leq 0.7$	P.R.	Lee and Ramdas (1984)
$1.586 + 1.50x$	80	$0 < x \leq 0.7$		Lee and Ramdas (1984)
$1.595 + 1.592x$	10	$0 < x \leq 0.7$		Lee and Ramdas (1984)

Measurement methods:

   R. = Reflectivity; E.M. = Excitonic Magnetoabsorption; E.R. = Electroreflectance;

   P. = Photoluminescence; E.L. = Ellipsometry; P.R. = Piezomodulated Reflectivity.

The first quantitative results on $E_g(x)$ were published by Gaj et al. (1978)[5.8] using reflectivity data. Linear increases in E_g against x were recorded by Twardowski et al. (1979)[5.9] using magnetoabsorption measurements with data confined to low x values, $0 < x < 0.2$. Modulated electroreflectance results by Bottka et al. (1981) provided a survey of $E_g(x, T)$ over nearly the complete single phase region of $Cd_{1-x}Mn_xTe$, and confirmed the linear increase of E_g with x seen by previous investigators.[5.10]

Photoluminescence results by Vecchi et al. (1981) demonstrated that crystal quality was sufficiently good to give band edge emissions for all x.[5.11] Finally, Lee and Ramdas (1984), using piezo-modulated reflectivity, were able to separate band edge features from spectra due to the presence of Mn^{2+} intra-ion transitions.[5.12] A summary of measured variations of E_g with x is given in Table 5.1.

5.2.2   Basic Theory of Magneto-Optical Properties of DMS

A unique aspect of $CdTe/Cd_{1-x}Mn_xTe$ and related II-VI SLs and QWs is the magnetic contribution by the Mn-ion to their electronic and optical properties. This manifests itself in "giant" spin splittings of the valence and conduction bands in external magnetic fields at low temperatures within the Mn-containing regions. The effects originate from spin coupling between the Mn-ion d-electrons and those of the Bloch-like band states.

5.2.2.1   Hamiltonian of the Problem

For a DMS system in an external magnetic field, the Hamiltonian for a band electron will have the form,[5.13]

$$H = H_o + H_B + H_C + H_{ex} + H_{eh} ,$$ (5.1)

where the five terms in the Hamiltonian correspond to various interactions influencing the band electron state. Relative contributions of each of the terms may vary depending on the crystal in question and on experimental conditions. Here H_o is a (one electron) Hamiltonian of the electron in a perfect crystal:

$$H_o = p^2 / 2m + V(r) .$$ (5.2)

The term

$$H_B = - (e/mc) \, \mathbf{p} \cdot \mathbf{A} + g \, \mu_B \, \sigma \cdot \mathbf{B} \qquad (5.3)$$

describes (in a linear approximation) the direct influence of the magnetic field on the carrier state. Here the symbols have their usual meaning. This term is responsible for Landau quantization and spin splitting of Landau levels (this gives only a small fraction of the total spin splitting in DMS).

The Coulomb term H_C represents energy of the carrier interacting with an impurity or with another carrier (e.g., electron-hole interaction producing exciton states).

The term H_{ex} represents the fundamental interaction in a semimagnetic semiconductor: the carrier-ion exchange. Following Bastard et al. (1978) we shall express it in a Heisenberg form:[5.14]

$$H_{ex} = - \Sigma_n \, J \, (\mathbf{r} - \mathbf{R}_n) \, \sigma \cdot \mathbf{S}_n , \qquad (5.4)$$

where $\mathbf{r}$ and $\mathbf{R}_n$ are the position vectors of the carrier and the magnetic Mn^{2+} ion; $J \, (\mathbf{r} - \mathbf{R}_n)$ is the position-dependent electron-ion exchange constant which falls off rapidly with the distance from a Mn site; σ and $\mathbf{S}_n$ are the carrier and the magnetic Mn^{2+} ion spins, respectively. The index n runs over all the magnetic ions.

Because the electronic wave function, in general, spans a large number of lattice sites, we can replace $J \, (\mathbf{r} - \mathbf{R}_n)$ by $xJ \, (\mathbf{r} - \mathbf{R}_i)$, where x is the Mn mole fraction in the material and $\mathbf{R}_i$ spans every site of the fcc sublattice occupied partially by Mn ions, so that the summation is now carried out over all $\mathbf{R}_i$. Because the spatial extent of the electron wave function is large enough to cover many Mn^{2+} ions, all the manganese spin operators $\mathbf{S}_n$ in the exchange Hamiltonian (Eq. (5.4)) can be replaced by $<\mathbf{S}_n>$, the thermal average of the Mn^{2+} spin. Considering a magnetically isotropic crystal

placed in a magnetic field (taken along the z-axis), we have $<S_x> = <S_y> = 0$ and $<S>$ $= <S_z>$, then Eq. (5.4) becomes

$$H_{ex} = - \sum_I xJ (r - R_i) \, \sigma_z <S_z> ,$$

(5.5)

here

$$<S_z> = S_0 \, B_{5/2} [(5/2 \, g \, \mu_B \, B) / k \, (T + T_0)] ,$$

(5.6)

where $B_{5/2}$ is the Brillouin function for the magnetization of the 5/2 Mn^{2+} spins located

in the $Cd_{1-x}Mn_xTe$ layers; an electronic spin S = 5/2 and Lande' factor g = 2; μ_B is the

Bohr magneton and k is the Boltzmann constant; S_0 and T_0 are phenomenological

parameters. S_0 characterizes the saturated magnetization of the material and, as a result

of the formation of antiferromagnetically coupled pairs, decreases as x increases; T_0

reflects the effect of long range magnetic coupling.[5.15]

The term H_{eh} represents the electron-hole exchange interaction and may be of

importance in exciton problems. The difference between the present case and a non-

magnetic semiconductor lies in the presence of the ion-carrier exchange Hamiltonian

H_{ex} in equation (5.1).

In wide-gap DMS, we may neglect the term H_B, if the temperature is not exces-

sively high, i.e., when the magnetic field effects due to carrier-ion exchange are strong

compared to "nonmagnetic" effects described by H_B.

5.2.2.2   Band Splitting by Exchange Interaction

Under the above assumptions, we can treat separately the conduction band and each

component of the valence band.[5.16] The basis vectors for the conduction (Γ_6) band:

$$|\tfrac{1}{2}, \tfrac{1}{2}\rangle_c = s\uparrow$$
$$|\tfrac{1}{2}, -\tfrac{1}{2}\rangle_c = s\downarrow,$$

(5.7)

for the Γ_8 valence band:

$$\left|\tfrac{3}{2}, \tfrac{3}{2}\right\rangle = \frac{1}{\sqrt{2}}(X + iY)\uparrow$$

$$\left|\tfrac{3}{2}, \tfrac{1}{2}\right\rangle = \frac{i}{\sqrt{6}}[(X + iY)\downarrow - 2Z\uparrow]$$

$$\left|\tfrac{3}{2}, -\tfrac{1}{2}\right\rangle = \frac{1}{\sqrt{6}}[(X - iY)\uparrow + 2Z\uparrow]$$ (5.8)

$$\left|\tfrac{3}{2}, -\tfrac{3}{2}\right\rangle = \frac{i}{\sqrt{2}}(X - iY)\downarrow,$$

and for the Γ_7 valence band:

$$\left|\tfrac{1}{2}, \tfrac{1}{2}\right\rangle_v = \frac{1}{\sqrt{3}}[(X + iY)\downarrow + Z\uparrow]$$

$$\left|\tfrac{1}{2}, -\tfrac{1}{2}\right\rangle_v = -\frac{i}{\sqrt{3}}[(X - iY)\uparrow - Z\downarrow]$$ (5.9)

In the chosen bases, matrices of H_{ex} are diagonal:

$$\langle \psi_c | H_{ex} | \psi_c \rangle = \begin{Vmatrix} 3A & 0 \\ 0 & -3A \end{Vmatrix}$$ (5.10)

$$\langle \psi_{v3/2} | H_{ex} | \psi_{v3/2} \rangle = \begin{Vmatrix} 3B & 0 & 0 & 0 \\ 0 & B & 0 & 0 \\ 0 & 0 & -B & 0 \\ 0 & 0 & 0 & -3B \end{Vmatrix}$$ (5.11)

$$\langle \psi_{v1/2} | H_{ex} | \psi_{v1/2} \rangle = \begin{Vmatrix} -B & 0 \\ 0 & B \end{Vmatrix}$$ (5.12)

where

$$A = -\tfrac{1}{6}N_0\alpha\langle S_z \rangle x \quad \text{and} \quad B = -\tfrac{1}{6}N_0\beta\langle S_z \rangle x.$$ (5.13)

Here N_0 denotes the number of unit cells per unit volume, and $\alpha = \langle s | J | s \rangle$ and $\beta = \langle X | J | X \rangle$ are exchange integrals for the conduction and valence bands, respectively.

A Zeeman scheme in a zinc-blende DMS is presented in Fig. 5.3 and in Table 5.2.
The relative intensities are proportional to the corresponding interband matrix elements.
The data of Table 5.2 are in good agreement with the experimental results obtained in
$Cd_{1-x}Mn_xTe$ if the exchange parameters are $N_0\alpha = 0.22$ eV and $N_0\beta = -0.88$ eV.
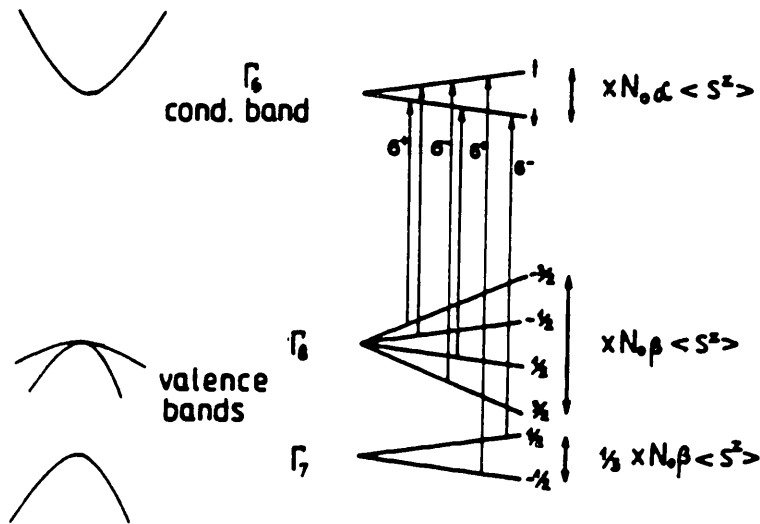
Fig. 5.3.   A schematic representation of band splittings in a cubic (zinc-blende)
semimagnetic semiconductor. Transitions allowed in the Faraday configu-
ration are marked by arrows.[5.13]

The exciton ground state in the DMS alloys splits in six components: four (denoted
A through D) visible in the σ polarization (electric field of light perpendicular to the
external magnetic field) and two (E and F) visible in the π polarization (electric field of
light parallel to the external magnetic field). In the Faraday configuration (light
propagation along the external magnetic field), the four σ-components exhibit σ^+ (A
and B) or σ^- (C and D) circular polarizations (see Fig. 5.3). The whole splitting pattern
is approximately symmetric relative to the zero field position.

Table   5.2.   Calculated energies and relative intensities of the Zeeman components of the free exciton in a zinc-blende semimagnetic semiconductor.[5.13]

States		Energy (Relative to zero field position)	Polarization	Relative intensity	Symbol
Valence	Conduction				
$\lvert \frac{3}{2} - \frac{3}{2}\rangle$	↓	$3B - 3A$	σ^+	3	A
$\lvert \frac{3}{2} - \frac{1}{2}\rangle$	↑	$B + 3A$	σ^+	1	B
$\lvert \frac{3}{2} - \frac{1}{2}\rangle$	↓	$B - 3A$	π	2	E
$\lvert \frac{3}{2} - \frac{1}{2}\rangle$	↑	$-B + 3A$	π	2	F
$\lvert \frac{3}{2} - \frac{1}{2}\rangle$	↓	$-B - 3A$	σ^-	1	C
$\lvert \frac{3}{2} - \frac{3}{2}\rangle$	↑	$-3B + 3A$	σ^-	3	D
$\lvert \frac{1}{2} - \frac{1}{2}\rangle$	↑	$-B + 3A$	σ^+	2	
$\lvert \frac{1}{2} - \frac{1}{2}\rangle$	↓	$-B - 3A$	π	1	
$\lvert \frac{1}{2} - \frac{1}{2}\rangle$	↑	$B + 3A$	π	1	
$\lvert \frac{1}{2} - \frac{1}{2}\rangle$	↓	$B - 3A$	σ^-	2	

$$A = -\tfrac{1}{6}xN_o\alpha\langle S^z\rangle \qquad B = -\tfrac{1}{6}xN_o\beta\langle S^z\rangle$$
Attention: $\langle S^z\rangle$ is normally negative!

For a given semiconductor in a given magnetic field and temperature, the Zeeman pattern can be characterized by splitting values of two pairs of σ-components: strong (A and D) and weak ones (B and C). The splitting of the two π components, E and F, is not independent. It equals one half of the difference between splittings A-D and B-C.

Fig. 5.4. shows the positions of the Zeeman components of the free exciton ground state of $Cd_{1-x}Mn_xTe$ as a function of magnetic field for various compositions. In crystals of low Mn mole fraction x, the splitting increases with x and the saturation is clearly visible, while at higher x values the curves show only a slight deviation from linearity. At higher temperatures the splittings showing as a function of field becomes smaller and the tendency to saturate is weaker.[5.17]
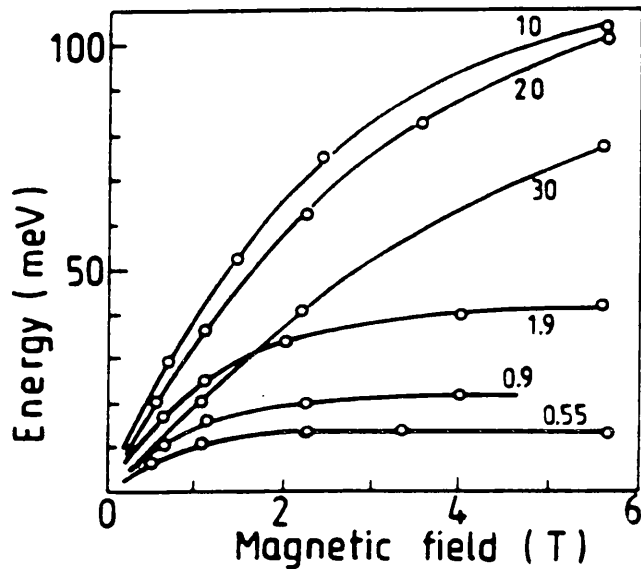
Fig. 5.4.   Splitting of the two strong σ-components of the exciton Zeeman structure of $Cd_{1-x}Mn_xTe$ versus magnetic field at 1.4 K. Manganese concentration values are given in percentage. [After Gaj et al. (1979).][5.17]

5.2.2.3   Exciton Luminescence

Most of the luminescence measurements on DMS have been performed in order to study bound magnetic polaron (BMP) effects. There is abundant evidence that carriers localized at impurities can induce sizeable magnetizations in their vicinity. These ferromagnetic complexes are termed bound magnetic polarons (BMP).

BMP control many properties of semimagnetic semiconductors; they are responsible for prominent features in the luminescence spectra of semimagnetics and for the increase in exciton binding energy at low temperatures. A study of the temperature, composition, and magnetic field variation of the luminescence features gives information concerning BMP interactions in such complexes as the acceptor, the

acceptor-bound exciton (A^0, X), and the donor-bound exciton (D^0, X).

At zero field, the (A^0, X) energy is lower than the energy of a dissociated system $(A^0 + X)$ by a binding energy that consists of a Coulomb part and an exchange (magnetic polaron) part. Application of a magnetic field, lowers the energy of the ground hole of both the bound and the dissociated systems by affecting the exchange contributions.

Now, the $(A^0 + X)$ system is affected more strongly by that additional energy, since both its holes are free to adjust the direction of their spins to the magnetic field direction, the orbital parts of their wavefunctions being different. The two holes in (A^0, X) have a symmetrical orbital wavefunction and the Pauli principle makes such a free adjustment impossible. In addition, the presence of an external magnetic field reduces magnetic polaron effects. Therefore, if the exchange effects are strong enough, at a certain field value the net binding energy will vanish and the bound state will disappear. Detailed studies of this phenomenon can supply information on excitonic wavefunctions, on the values of the exchange constant for bound states and on the magnetic polaron effects.

5.3   Growth of $CdTe/Cd_{1-x}Mn_xTe$ QWs

The application of MBE techniques has to date yielded a substantial number of $CdTe/Cd_{1-x}Mn_xTe$ SLs and QWs over a range of Mn-ion concentrations (x) and layer thicknesses, so far mostly grown on GaAs substrates. For the reproducible growth of high quality structures, much care is needed in both the choice of substrate material and preparation of the substrate surface.

For this investigation InSb ($a = 0.64782$ nm) was chosen as the substrate material.

The reason for this choice is that it is readily available as large area single crystals of good structural quality and, in particular, it is very well lattice matched to CdTe (a = 0.64810 nm). Because the lattice mismatch between InSb and CdTe is < 0.05 % at 25 °C, strain effects on the epitaxial layers are expected to be significantly smaller than those grown on the more commonly used GaAs substrate.[5.18] However, for $Cd_{1-x}Mn_xTe$ layers, the lattice match becomes less satisfactory as x increases. The lattice mismatch between InSb and $Cd_{1-x}Mn_xTe$ is ~ 0.44 % at 25 °C for the value of x = 0.2. Another important factor in its selection is that the layer growth temperatures are relatively low (< 240 °C), which results in minimizing interdiffusion. Growth of similar heterostructures on GaAs substrates using conventional MBE has so far required temperatures of > 300 °C.

The structures were grown at the University of Hull, using a computer-controlled VG Semicon V80H MBE system. The Cd and Te_2 fluxes were provided by a single source of high-purity polycrystalline CdTe (MCP Ltd., UK), a second evaporation source being loaded with 4N grade Mn (Johnson-Matthey Puratronic), which had previously been vacuum distilled. The (001) p-type InSb substrates were chemically etched and the surface oxide then removed in vacuo using 500 eV argon ion etching and thermal annealing cycles. This is a crucial step in the preparing of InSb. Because the air cleaving procedure causes damage. The substrate temperature was typically set in the range 200 - 250 °C for growth. Multilayer structures were deposited at a growth rate of 0.5 μm / h throughout and consisted of a buffer layer of 0.1 μm CdTe followed by a 0.2 μm $Cd_{1-x}Mn_xTe$ alloy layer, on which the MQWs and SQWs were grown. The structure was finally capped with a 0.2 μm $Cd_{1-x}Mn_xTe$ layer. The purpose of the capping layer was to enable the concentration x to be determined by comparing the photoluminescence from this layer with that from standard bulk specimens.[5.18]

In this work a series of CdTe/Cd$_{1-x}$Mn$_x$Te multiple quantum wells (MQWs) and single quantum wells (SQWs) was investigated. The sample parameters are given in table 5.3.

Table   5.3.   CdTe/Cd$_{1-x}$Mn$_x$Te MQW and SQW parameters. L_w and L_B are the widths of the CdTe and Cd$_{1-x}$Mn$_x$Te layers, x is the Mn ion concentration.

QWs	CdTe L (Å)	CdMnTe L (Å)	x
M145	150	150	0.063
M154	75	75	0.065
M157	100	100	0.063
M230	20 50 80 150	2000 2000 2000 2000	0.125 0.125 0.125 0.125

The MQWs structures contained five CdTe wells with the same widths, separated by Cd$_{1-x}$Mn$_x$Te barriers. The QW width ranged from 75 to 150 Å for the three different samples. In each sample, the CdTe thickness L_w was made nominally equal to the Cd$_{1-x}$Mn$_x$Te thickness L_B, so that the strains in corresponding layers of the different samples were the same.[5.18]

The SQWs structure consisted of four CdTe wells with widths of 20, 50, 80, 150 Å, respectively, separated by Cd$_{1-x}$Mn$_x$Te (x = 0.125) barriers of 2000 Å width. The wells were grown sequentially from 150 Å to 20 Å with the well 20 Å closest to the surface. The wide barriers ensured that each quantum well was independent, both electronically and structrually, of its neighbours. The CdTe/Cd$_{1-x}$Mn$_x$Te MQW and SQW parameters are given in table 5.3.

5.4   Luminescence of CdTe/Cd$_{1-x}$Mn$_x$Te QWs

Photoluminescence (PL) spectra were excited using the 488 nm line from an Argon-ion laser. The emitted light was dispersed by a 1m double-grating spectrometer and detected with a cooled GaAs photomultiplier tube using photon-counting technique. The resolution was 0.2 Å. The relative intensities of the PL spectra are not corrected for the spectral response of the monochromator and detector since it is flat in this region of the spectrum over the range of interest. The spectra were recorded at 4 ± 0.2 K.

Fig. 5.5 (a) shows such a spectrum for sample M157 in zero magnetic field and atmospheric pressure. Also shown in the figure is a schematic of the conduction band in the quantum wells. The energy of the lowest level (n = 1) is indicated by the dashed line inside the wells. The spectrum consists of three peaks A (1.688 eV), B (1.606 eV) and C (1.554 eV). The highest energy peak A is recombination from the Cd$_{1-x}$Mn$_x$Te (x = 0.063) capping layer and the very weak peak C is probably from the CdTe buffer layer emission. The very sharp peak B is attributed to free exciton recombination from the five quantum wells, all of the same well width (L$_w$ = 100 Å).

The spectrum of sample M145 is shown in Fig. 5.5 (b).The three peaks A' (1.680 eV), B' (1.600 eV) and C' (1.557 eV) are emissions from the Cd$_{1-x}$Mn$_x$Te (x = 0.063) capping layer, the five quantum wells (L$_w$ = 150 Å) and the CdTe buffer layer, respectively.

In Fig. 5.5 (c), the spectrum of sample M154 is similar to that of M145. The three peaks A'' (1.718 eV), B'' (1.627 eV) and C'' (1.552 eV) are attributed to the Cd$_{1-x}$Mn$_x$Te (x = 0.065) capping layer, the five quantum wells (L$_w$ = 75 Å) and the CdTe buffer layer, respectively.

The PL spectra from the MQW structures differ markedly from those of the single layers. The most prominent feature of the spectra is the shift to shorter wavelength in

the thinner layers, which is clear indication of quantum confinement effects. It is clear that in Fig. 5.5 (b) and (c) the exciton energies of peaks A" and B" are much (~ 38 and ~ 27 meV) higher than those of peaks A' and B' due to their different x values and well widths.
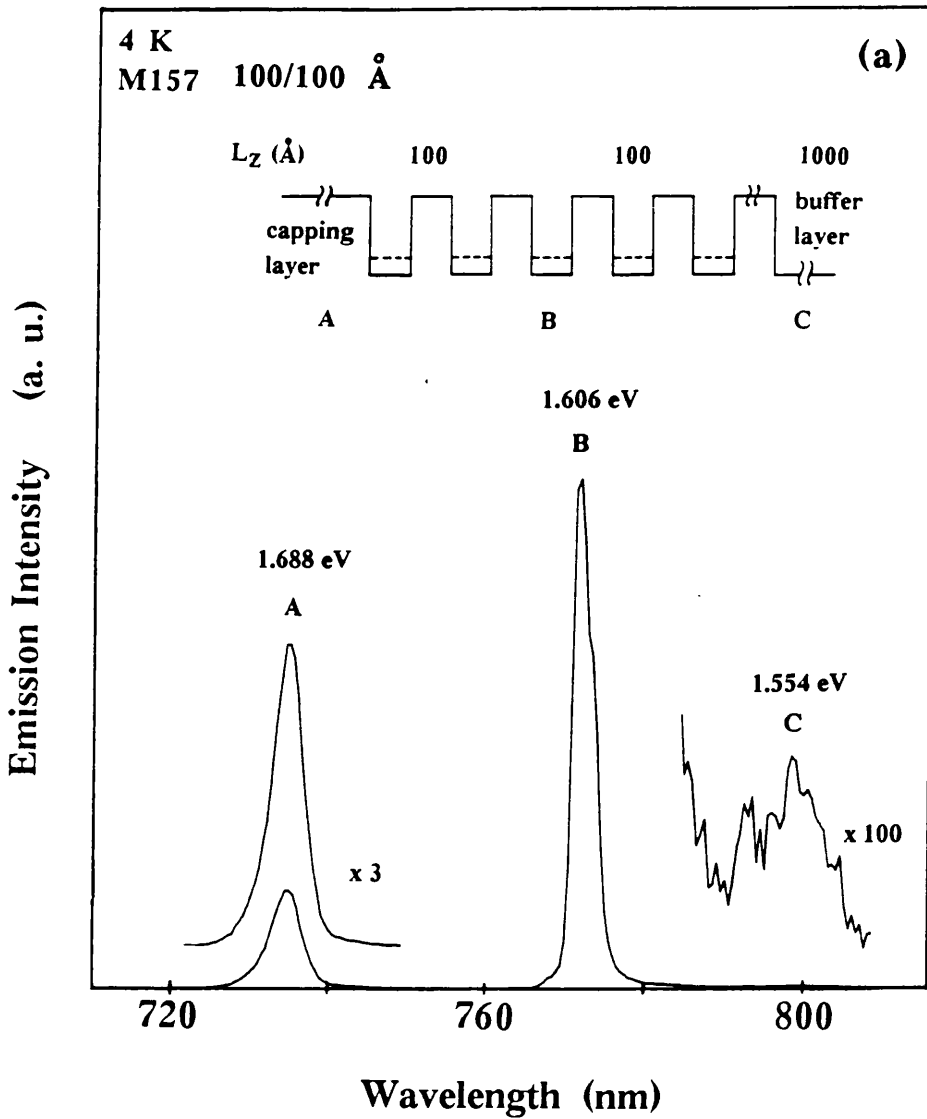
Fig. 5.5 (a). PL spectrum of sample M157 at zero magnetic field and atmospheric pressure and at 4 K. The MQWs had well width L_w 100 Å separated by 100 Å wide $Cd_{1-x}Mn_xTe$ barriers (x = 0.063).
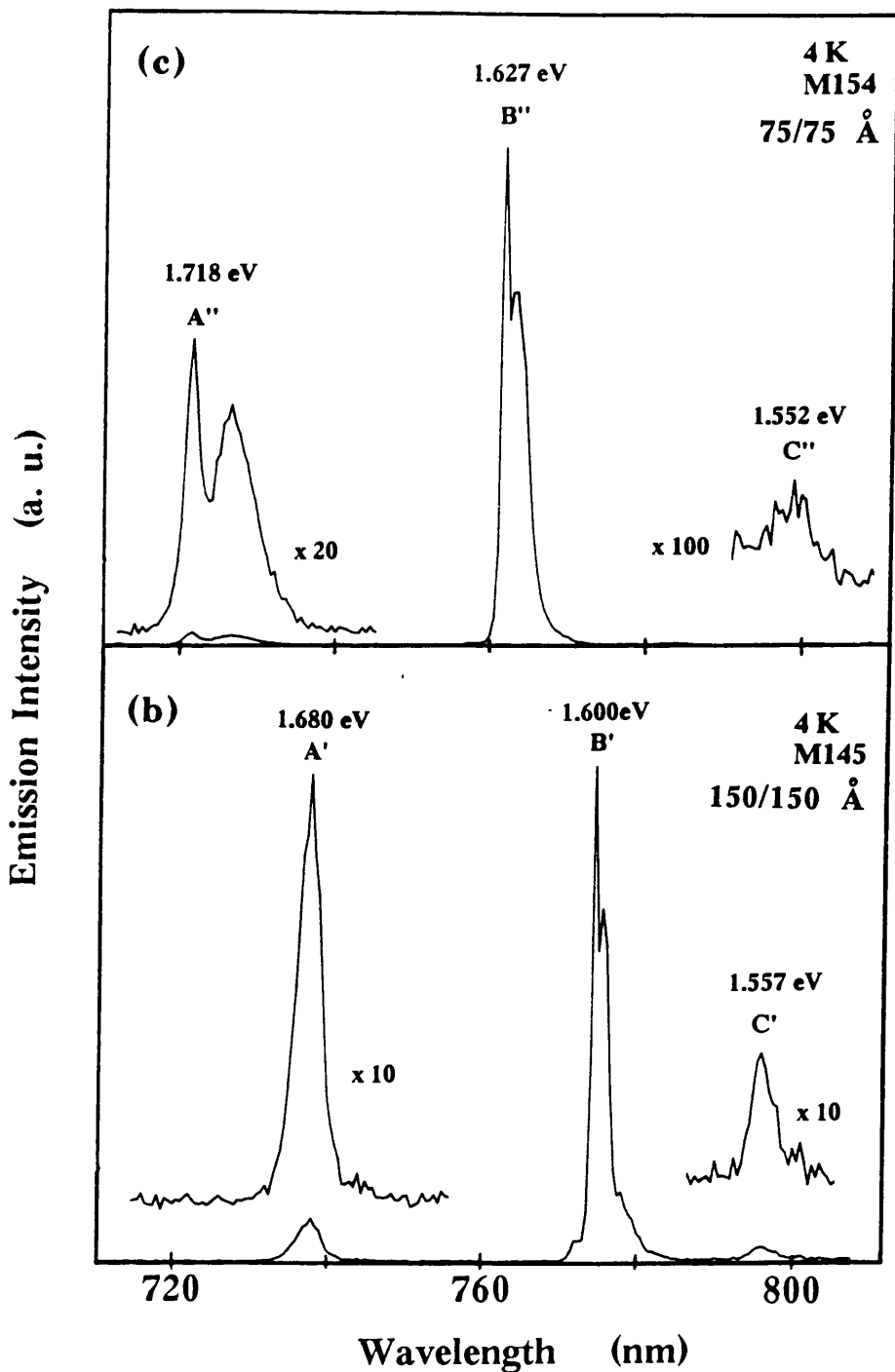
Fig. 5.5 (b)-(c). PL spectra at zero magnetic field, 1 bar and 4 K. (b) MQWs M145 had

well width L_w 150 Å separated by 150 Å wide $Cd_{1-x}Mn_xTe$ barriers

(x = 0.063); (c) MQWs M154 had well width L_w 75 Å separated by

75 Å wide $Cd_{1-x}Mn_xTe$ barriers (x = 0.065).

In studies of bulk $Cd_{1-x}Mn_xTe$ at various laboratories,[5.19] it has been shown that the main PL is from excitons bound by the statistical fluctuations in alloy composition (L2 emission), from excitons bound at neutral acceptors (L1 emission) and from excitons bound at neutral donors. All of these emission energies depend on the composition parameter x. For high values of x ($> \sim 0.1$) the L2 emission dominates, whilst at lower x ($< \sim 0.1$), the emission from excitons bound at defects or impurities is found to be the strongest. Therefore, the barrier layer emission of the three samples is identified as that of excitons bound at neutral impurities.

The PL linewidths of peaks A and A' are ~ 10 and ~ 6 meV. Because the capping layer emission is very sensitive to x, a depth or lateral variation in x will cause broadening, these results suggest that the Mn concentrations are quite uniform across these samples.

Fig. 5.6 shows the spectrum of SQWs (sample M230) at zero magnetic field and atmospheric pressure and at T = 4 K. A schematic of the conduction band in the quantum wells is also shown in the figure. The energy of the lowest level (n = 1) is indicated by the dashed line inside the wells. Peak D (1.778 eV) comes from the $Cd_{1-x}Mn_xTe$ (x = 0.125) capping layer. Peaks E (1.725 eV), F (1.655 eV), G (1.624 eV), H (1.602 eV) are related to the free exciton emissions from the four single quantum wells, of width, 20, 50, 80 and 150 Å, respectively. Peak K (1.590 eV) is probably from the CdTe buffer layer.

In this sample, the wells were grown sequentially from H to E with well E closest to the surface and well H furthest from the sample surface. Hence the intensities of peaks farther from the surface of the sample are smaller. However, we should notice that the intensity of peak G is much weaker than that of peak H. This is probably due to the poorer quality of quantum well G. In Fig. 5.6, it is clear that the emission energies for the wells increase with decreasing well width.
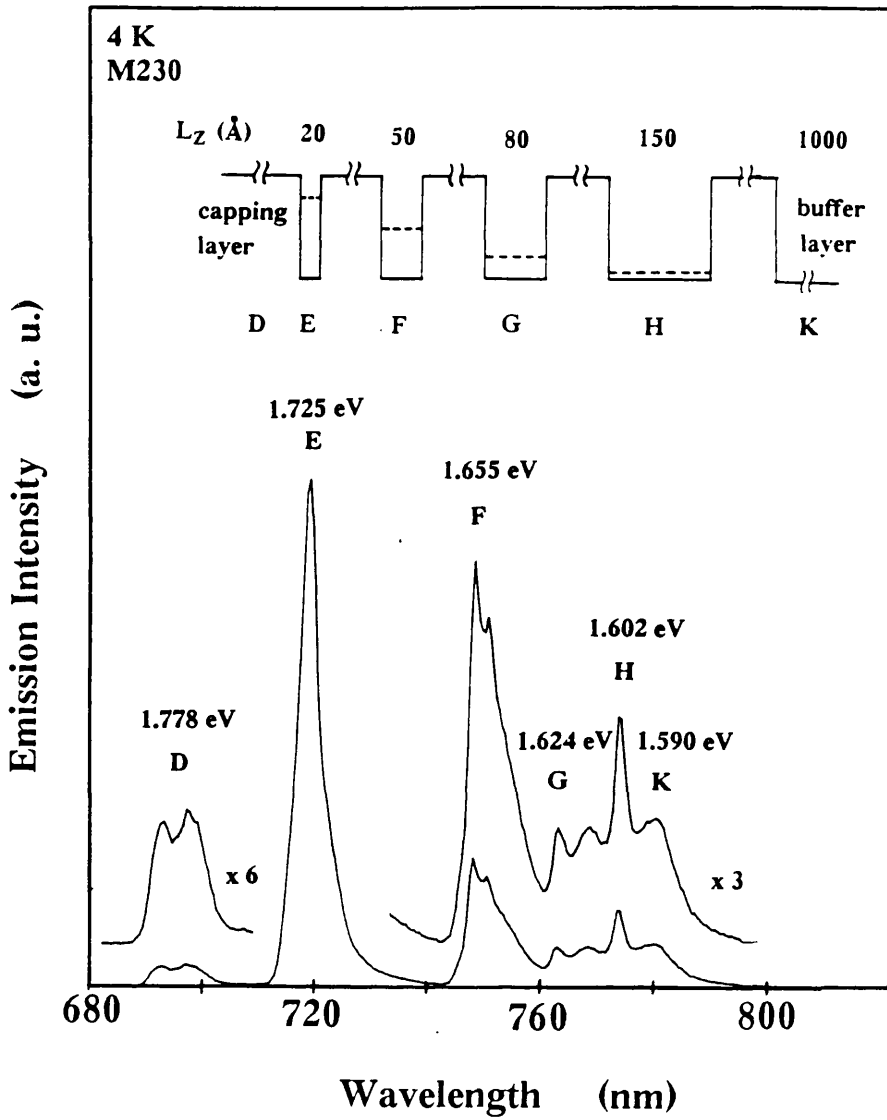
Fig. 5.6. PL spectrum of SQW sample M230 at zero magnetic field and atmospheric pressure and at 4 K. The quantum wells E — H had well widths L_w of 20, 50, 80 and 150 Å, separated by 2000 Å wide $Cd_{1-x}Mn_xTe$ barriers (x = 0.125).

Fig. 5.7 shows the band edges of a CdTe/Cd$_{1-x}$Mn$_x$Te QW. Here E$_g$ is the band

gap of CdTe, ΔE_C and ΔE_V are the conduction and valence band discontunities,

E$^e_{Conf.}$ and E$^h_{Conf.}$ are the electron and hole confinement energies, respectively.
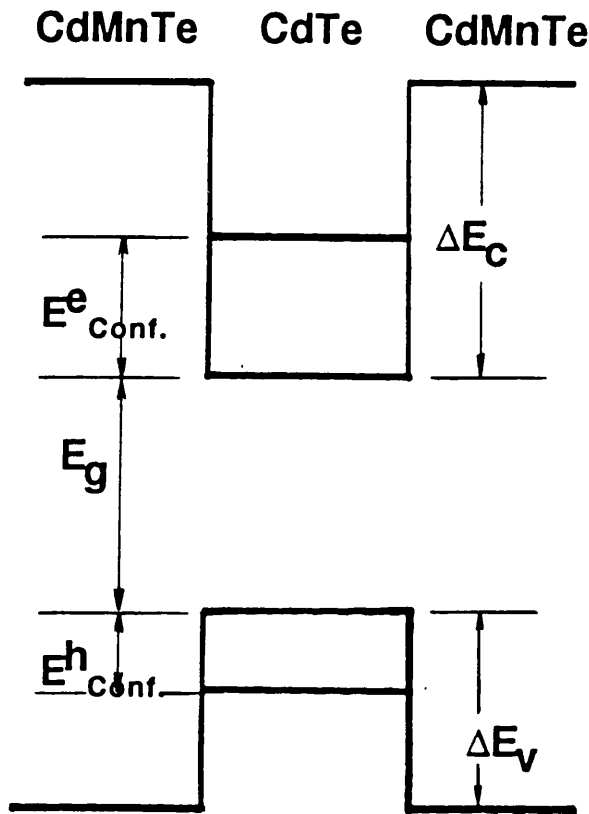
Fig. 5.7. Schematic of the band edges of a CdTe/Cd$_{1-x}$Mn$_x$Te quantum well at zero
magnetic field.

The free exciton emission energy E$_x$ is given by

$$E_x = E_g + E^e_{Conf.} + E^h_{Conf.} - E_B, \qquad (5.14\ a)$$

where E$_B$ is the exciton binding energy. For the infinite square well (ideal case):

$$E^{e,h}_{Conf.} = (h\,n)^2 / (8\,m^*_{e,h}\,L_w{}^2), \quad n = 1, 2, 3.... \qquad (5.14\ b)$$

From equation. (5.14), we can see that E_x increases with increasing $E^e_{Conf.}$ and $E^h_{Conf.}$. Therefore, when the well width is narrower, the exciton emission energy is larger due to the quantum confinement effect.

Fig. 5.8 shows the measured energy dependence of the quantum well emission for sample M230 as a function of well width. The calculated result of infinite well is shown in the dashed curve. Considering that the confinement energies for finite well are lower than those of infinite well, our experimental results compared well to the theoretical one.
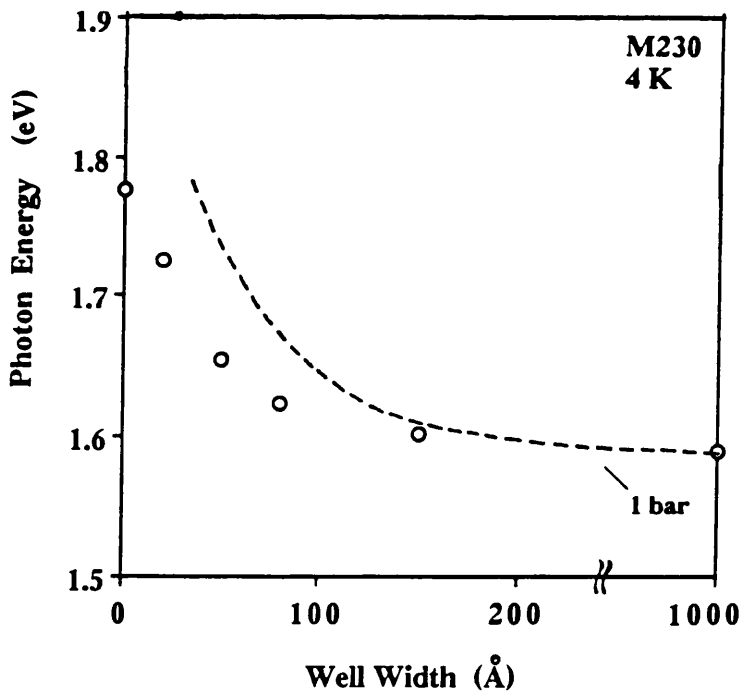
Fig. 5.8. The measured energy dependence of the quantum well emission for SQWs M230 as a function of well width. The dashed curve shows the calculated result of infinite well.

5.5. CdTe/Cd$_{1-x}$Mn$_x$Te QWs under Hydrostatic Pressures

Interest in the behaviour of SLs and QWs under hydrostatic pressure[5.20] and the rapid development of II-VI strained-layer SLs and QWs[5.21] have given rise to optical studies of such new system under pressure in order to explore the electronic levels and to test a number of bulk and SL parameters of the layer components.[5.22]

High pressure enables the lattice constants to be varied in a controlled way, over a variation of a few percent, while keeping other factors controlled or changing in a known way. Since the compressibilities of different semiconductors vary, there can be pressure-induced biaxial strains between semiconductors that share a common interface. Then, applied pressure can allow sufficient tuning of mismatch in a single sample to simulate a wide range of materials at atmospheric pressure (1 bar). Therefore, measurements of photoluminescence (PL) under high pressure can provide a direct determination of some of the important material parameters.

So far there have been few reports on the pressure dependence of luminescence in CdTe/CdMnTe strained-layer structures[5.23] limited to SLs and QWs with one well width only. In this part we report new values for the hydrostatic pressure coefficients of CdTe/Cd$_{1-x}$Mn$_x$Te MQWs and SQWs with different well width.

5.5.1 Experimental Considerations

For high pressure measurements, the substrates were thinned mechanically to a thickness of about 30 μm. The samples were cleaved to about 100 μm x 100 μm for loading in the pressure cell. A single sample and a fine ruby particle were placed in a gasketed Diacoll diamond anvil cell (DAC). A 4 : 1 mixture of methanol and ethanol

was used as the pressure transmitting fluid. The pressure was determined using the pressure dependence of ruby luminescence.[5.24] The DAC was inserted in a variable temperature cryostat cooled by liquid helium. In order to achieve optimal hydrostatic conditions, the pressure was changed at room temperature.

Two kinds of samples were investigated by PL experiments under hydrostatic pressures. The first sample is SQWs (M230), which consists of four QWs with different well width from 20 - 150 Å, separated by 2000 Å $Cd_{1-x}Mn_xTe$ (x = 0.125) barriers. The second sample is MQWs (M157), which consists of five QWs with the same well width 100 Å, separated by 100 Å $Cd_{1-x}Mn_xTe$ (x = 0.063) barriers.

5.5.2 Pressure Dependence of the Emission from $CdTe/Cd_{1-x}Mn_xTe$

Typical behaviour of the PL spectra of $CdTe/Cd_{1-x}Mn_xTe$ SQWs at 4 K and under hydrostatic pressures up to 21 kbar is shown in Fig. 5.9 (a) - (d). Each of the spectra is normalized to its maximum intensity. Fig. 5.9 (a) shows the spectrum at p = 1 bar. Peak D comes from the $Cd_{1-x}Mn_xTe$ capping layer. Peaks E, F, G and H are related to the free exciton emissions from the four single quantum wells, of width, 20, 50, 80 and 150 Å, respectively. Peak K is emission from CdTe buffer layer. The wells were grown sequentially from H to E with the well E closest to the surface. The emission energies for the wells increase with decreasing well width.

As pressure is applied, all the peaks move to higher energies at about the same rate without significant spectral broadening and their relative intensities do not change very much at higher pressures. In Fig.5.9 (c) and (d), the six peaks can be seen very clearly, which rapidly shift to higher energies with increasing pressure from 12 kbar to 21 kbar. When the pressure was raised about 35 kbar, all peaks dramatically decrease in intensity. The quenching means that a crystallographic phase transition of CdTe occurs from the zincblende to the NaCl structure, which destroys the PL irremediably.[5.25]
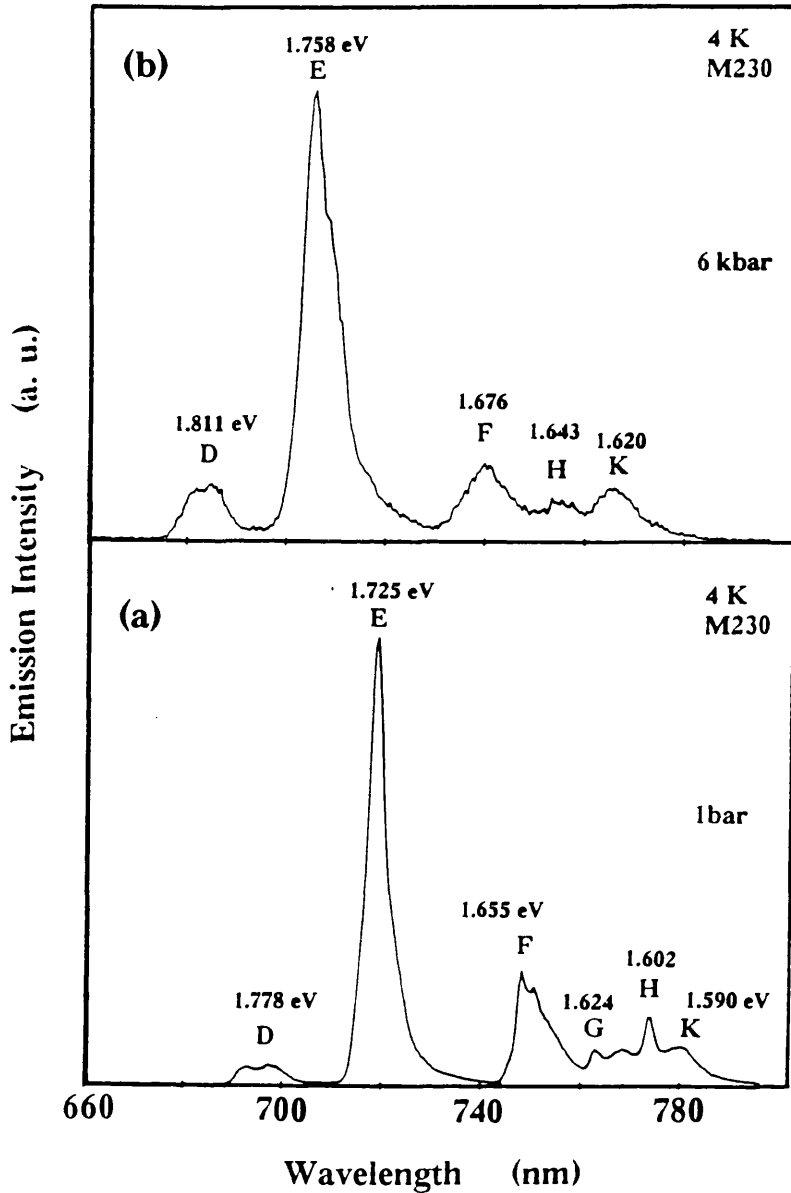
Fig. 5.9 (a) - (b). PL spectra of SQWs (M230) at p = 1 bar and 6 kbar and 4 K. Peak
D comes from the $Cd_{1-x}Mn_xTe$ capping layer. Peaks E, F, G and H
are related to the free exciton emissions from the four QWs, of
width, 20, 50, 80 and 150 Å, respectively. Peak K is emission from
CdTe buffer layer. With increasing pressure , all the peaks shift to
higher energies.
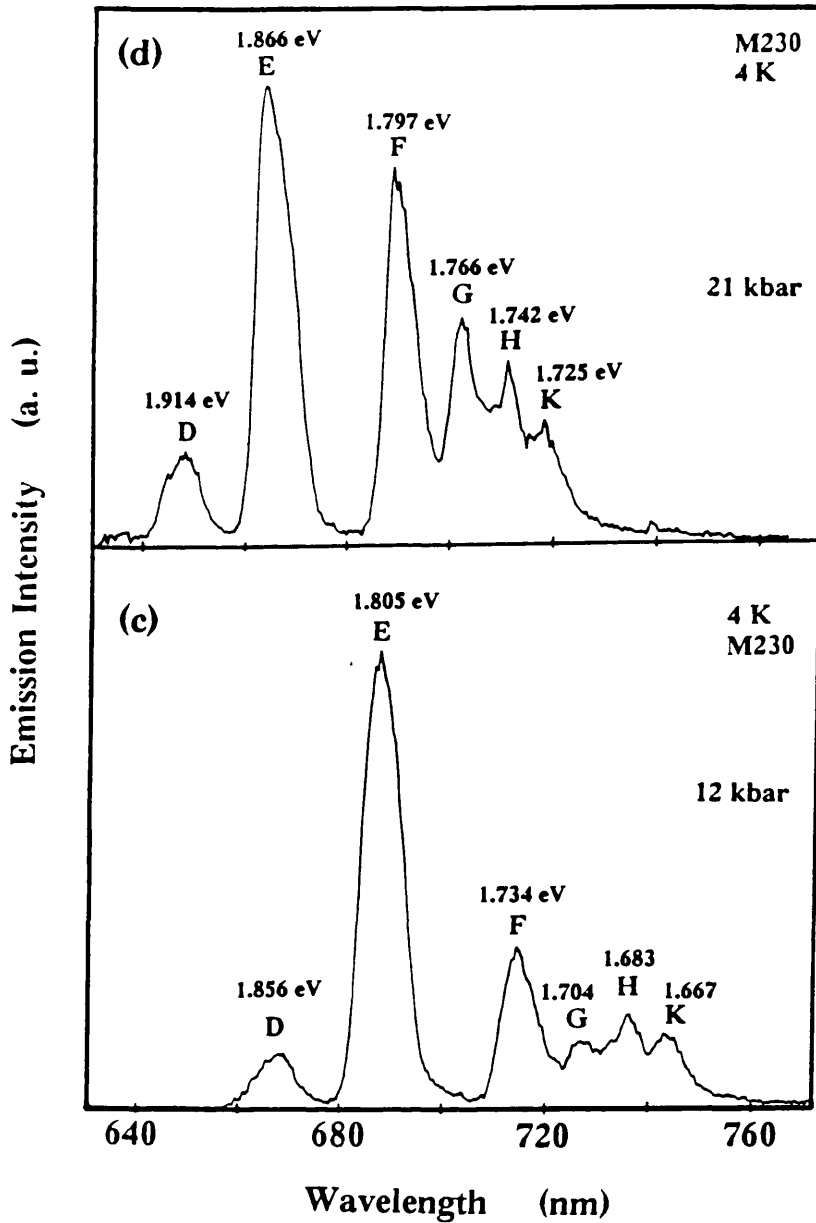
Fig. 5.9 (c) - (d). PL spectra of SQWs (M230) at p = 12 and 21 kbar and 4 K. Peak D comes from the $Cd_{1-x}Mn_xTe$ capping layer. Peaks E, F, G and H are related to the free exciton emissions from the four QWs, of width, 20, 50, 80 and 150 Å, peak K is emission from CdTe buffer layer, respectively. With increasing pressure , all the peaks shift to higher energies.

These structures differ from the well-established III-V structures in remaining direct gap up to their phase transition pressures, limiting the scope for obtaining information on the band line-up near Γ-X crossovers.

The PL spectra of CdTe/$Cd_{1-x}Mn_xTe$ MQWs (M157) at 4 K and under hydrostatic pressures up to 25 kbar are shown in Fig. 5.10 (a) - (d). Each of the spectra is normalized to its maximum intensity. The p = 1 bar spectrum consists of three peaks A, B, and C, which are identified as the $Cd_{1-x}Mn_xTe$ (x = 0.063) capping layer emission, free exciton recombination from the five QWs (L_w = 100 Å) and the CdTe buffer layer, respectively.

With increasing pressures, we can see that all the peaks move to higher energies at about the same rate without significant spectral broadening. As the pressure was raised about 35 kbar, all peaks dramatically decrease in intensity, in the same way as that exhibited by sample M230.
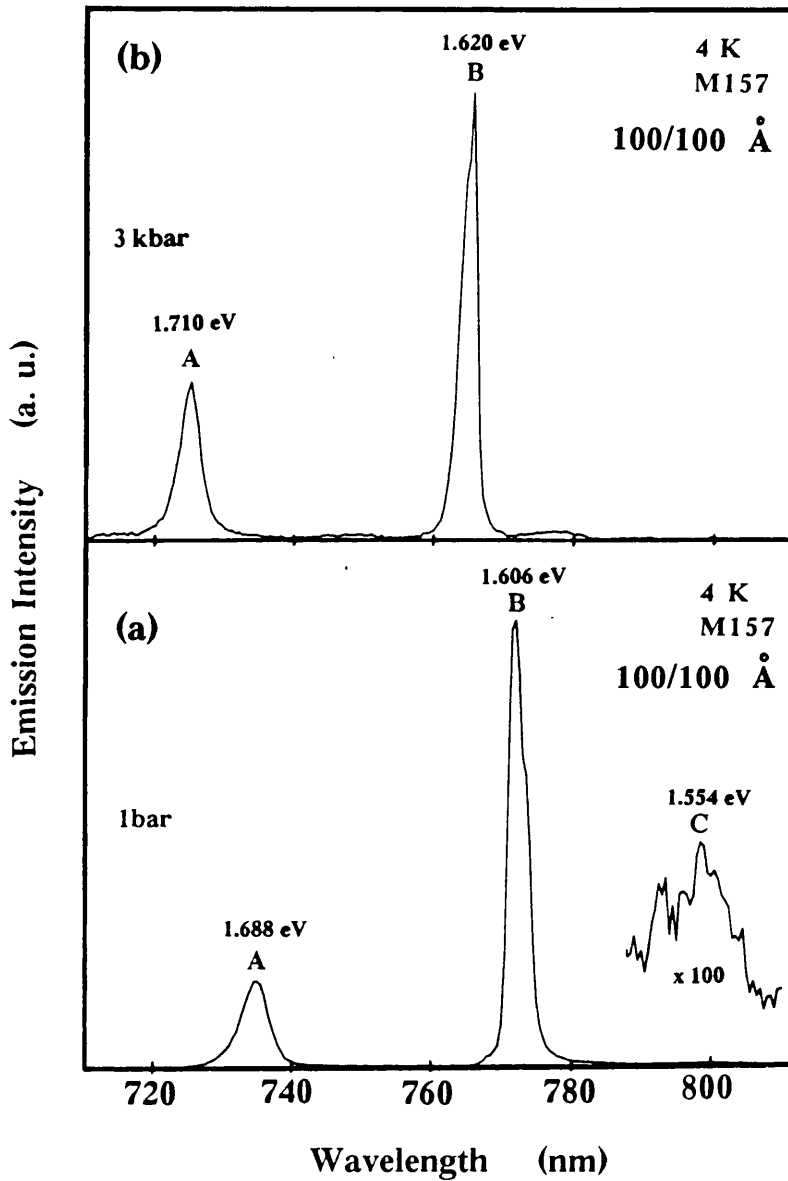
Fig. 5.10 (a) - (b). PL spectra of MQWs M157 at p = 1 bar and 3 kbar and 4 K. Peaks A, B and C are the emissions from the $Cd_{1-x}Mn_xTe$ (x = 0.063) capping layer, CdTe QWs (L_w = 100 Å) and CdTe (1000 Å) buffer layer, respectively. With increasing pressure , all the peaks move to higher energies.
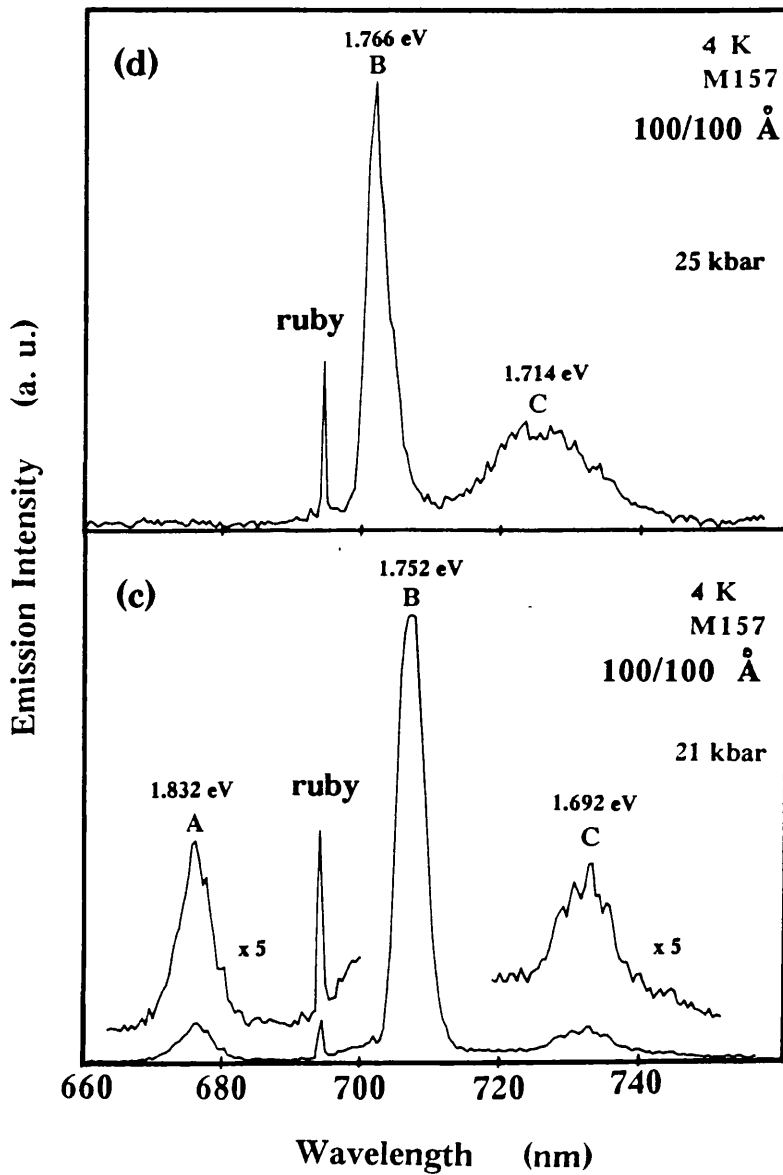
Fig. 5.10 (c) - (d). PL spectra of MQWs M157 at p = 21 and 25 kbar and 4 K. Peaks A, B and C are the emissions from the $Cd_{1-x}Mn_xTe$ (x = 0.063) capping layer, CdTe quantum wells (L_w = 100 Å) and CdTe (1000 Å) buffer layer, respectively. With increasing pressure , all the peaks move to higher energies.

Fig. 5.11 shows the effect of pressure on the emission energies of SQWs (sample M230) at 4 K for different well widths. Also shown in Fig. 5.11 are the pressure dependences of the PL from the $Cd_{1-x}Mn_xTe$ capping layer and CdTe buffer layer.
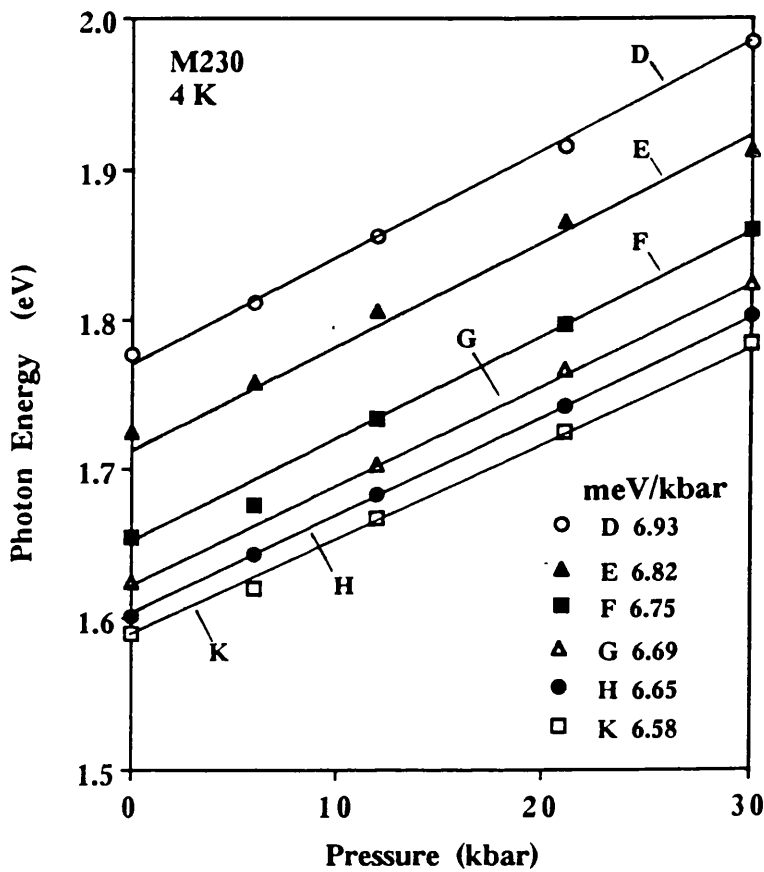
Fig. 5.11. Photon energy of emissions D ($Cd_{1-x}Mn_xTe$ capping layer, x = 0.125), E (20 Å), F (50 Å), G (80 Å), H (150 Å) and K (1000 Å CdTe buffer layer) as a function of pressure for SQWs (M230) at 4 K. The solid lines are least-squares fits to the data. The pressure coefficient decreases with increasing well width, as can be seen from the slopes of each line in the inset.

Since the pressure shifts were found to be essentially linear over the 1 bar ~ 30 kbar pressure range, a least-squares fit was employed for each set of data using the linear function:

$$E(p) = E(p = 0) + \alpha\, p, \qquad\qquad (5.15)$$

where energy E is in eV and pressure p is in kbar.

In Fig. 5.11 we can see that the pressure coefficients α of the four single QWs (20, 50, 80 and 150 Å) are 6.82 ± 0.05, 6.75 ± 0.05, 6.69 ± 0.05 and 6.65 ± 0.05 meV/kbar, respectively. It is clear that narrower wells have larger pressure coefficients. The well-width dependence of the pressure coefficients, though small, is a real effect outside the experimental uncertainty. Therefore our results show a weak but distinguishable decrease in the pressure coefficient of the transition energy as the well width is increased. We can also see that the pressure coefficients α of the four QWs are smaller than that (6.93 ± 0.05 meV/kbar) of the $Cd_{1-x}Mn_xTe$ capping layer (x = 0.125), but larger than that (6.58 ± 0.05 meV/kbar) of CdTe buffer layer (1000 Å). The pressure coefficients obtained from the slopes of this sample are listed in Table 5.4.

Fig. 5.12 shows the effect of pressure on the emission energy for MQWs (sample M157) at 4 K. Also shown in Fig. 5-12 are the pressure dependences of the PL from the $Cd_{1-x}Mn_xTe$ capping layer (x = 0.063) and CdTe buffer layer (1000 Å).

For sample M157 (see Fig. 5.12), emission A of $Cd_{1-x}Mn_xTe$ capping layer (x = 0.063) shows a linear pressure shift of 6.83 ± 0.05 meV/kbar, which is similar to, but somewhat smaller than that of the $Cd_{1-x}Mn_xTe$ emission (D line) of sample M230 (x = 0.125). This is probably due to the different manganese concentrations in the barriers between the two samples. Peak C of the buffer layer shifts at a rate of 6.54 ± 0.05 meV/kbar, which is very close to that of emission K of sample M230. The pressure coefficient α of emission B from the five quantum wells of 100 Å width is 6.60 ± 0.05

meV/kbar, which is smaller than that (6.65 ± 0.05 meV/kbar) of 150 Å QW of sample M230, probably due to the different manganese concentrations in the barriers. However, this value is smaller than that of emission A and larger than that of emission C. This trend is the same as that of sample M230. The pressure coefficients obtained from the slopes of this sample are also listed in Table 5.4.
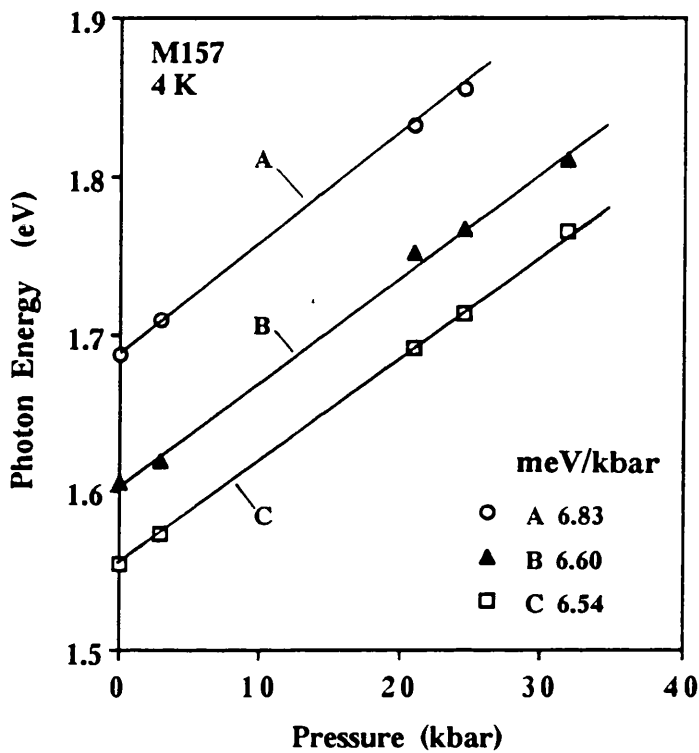
Fig. 5.12. Photon energy of emissions A ($Cd_{1-x}Mn_xTe$ capping layer, x = 0.063), B (quantum wells, L_w = 100 Å) and C (1000 Å CdTe buffer layer) as a function of pressure for MQWs (M157) at 4 K. The solid lines are least-squares fits to the data.

The pressure coefficient α for $Cd_{1-x}Mn_xTe$ is known to depend[5.4] on x. At 300 K, the values of α for bulk $Cd_{1-x}Mn_xTe$ range from 8 - 4.6 meV/kbar between x = 0 to

0.7. We have measured the α for the capping layers in samples M230 and M157 at 4 K to be 6.93 ± 0.05 and 6.83 ± 0.05 meV/kbar, in reasonable agreement with Ref. 5.4. Our measurement of α for CdTe buffer layers at 4 K is 6.58 ± 0.05 and 6.54 ± 0.05 meV/kbar, respectively, consistent with 6.5 ± 0.05 meV/kbar in bulk CdTe obtained by Dunstan et al.[5.26] The pressure coefficient α of the quantum wells of 100 A width is 6.60 ± 0.05 meV/kbar. Within experimental accuracy, this value compares well to 6.4 meV/kbar in a CdTe/CdMnTe quantum well structure reported by Wilkinson et al.[5.27]

Table 5.4. CdTe/$Cd_{1-x}Mn_xTe$ SQWs (M230) and MQWs (M157) parameters and pressure coefficients α. x is the Mn ion concentration.

	CdMnTe (capping layer)	CdTe (well width Å)	α meV/kbar
(SQWs) M230	(x = 0.125) 2000 Å		6.93 ± 0.05
		20	6.82 ± 0.05
		50	6.75 ± 0.05
		80	6.69 ± 0.05
		150	6.65 ± 0.05
		1000 (buffer layer)	6.58 ± 0.05
(MQWs) M157	(x = 0.063) 2000 Å		6.83 ± 0.05
		100	6.60 ± 0.05
		1000 (buffer layer)	6.54 ± 0.05

Fig. 5.13 shows the measured pressure dependence of the quantum well emission for sample M230 as a function of well width. Here the point at zero well width is obtained from the pressure coefficient α of the $Cd_{1-x}Mn_xTe$ (x = 0.125) capping layer (peak D), the point at 1000 Å well width is obtained from that of the CdTe buffer layer (peak K). A systematic decrease in α is seen with increasing the well width. The statistical error in each value of α is about ± 1%. We also observe that the wide well PL pressure coefficient α is significantly higher than that of bulk CdTe.
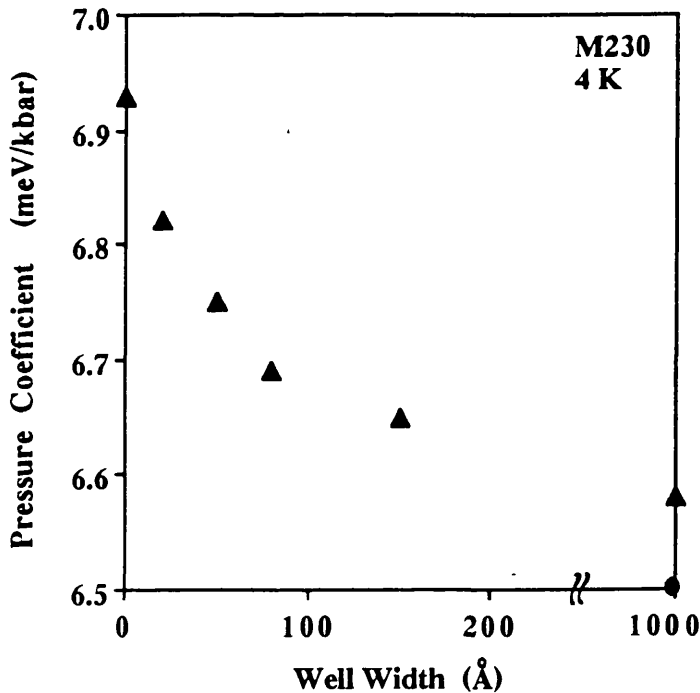
Fig. 5.13. Pressure coefficient of the quantum well emission as a function of well width (sample M230). Here the point at zero well width is obtained from the pressure coefficient α of the $Cd_{1-x}Mn_xTe$ (x = 0.125) capping layer (peak D), the point at 1000 Å well width is obtained from that of the CdTe buffer layer (peak K). The full circle is the value for bulk CdTe from Dunstan et al.[5.26]

Venkateswaran et al[5.28] have observed that the pressure coefficient from a narrow GaAs/$Al_x Ga_{1-x}$As QW has a smaller value than that of a wide well, which is the opposite of the results presented here. However, in InGaAs/GaAs strained QWs the pressure coefficient is found to increase with decreasing well width ,[5.29, 5.30] which is similar to our results observed in CdTe/$Cd_{1-x}Mn_x$Te strained layer SQWs.

The pressure coefficient of the emission from a quantum well can vary with well width due to effects related to the confinement energy. When the quantum well width is very wide and approaches the bulk limit, the confinement energy vanishes, the confined states behave exactly as the band edge in the bulk matarial, and the pressure coefficient should be that of the equivalent bulk crystal. In our experiments, we observed a pressure coefficient for the CdTe 1000 Å buffer layer of 6.58 ± 0.05 meV/kbar and as the well width increases, α approaches that of the buffer layer with α = 6.65 ± 0.05 meV/kbar. The bulk limit is not reached probably due to strain remaining in the CdTe buffer layer.

For very narrow quantum wells, most of the confined-state wave function is in the $Cd_{1-x}Mn_x$Te barrier layers. Therefore, as $L_w \to 0$, the pressure coefficient should approach that of $Cd_{1-x}Mn_x$Te as shown in Fig. 5.13. Thus the wider well has a smaller α since the pressure coefficient of the CdTe well layer has a smaller value than that of the $Cd_{1-x}Mn_x$Te barrier layer. In GaAs/$Al_x Ga_{1-x}$As heterostructures, α in the well layer (GaAs) is larger than that in the barrier layer ($Al_x Ga_{1-x}$As),[5.31] and the dependence of α on L_w is in the opposite direction.

There are several effects that may account for the well-width dependence of α. Pressure decreases the lattice constant and therefore narrows the well width in a hete-

rostructure. In addition, the effect of different pressure coefficients in the well and barrier layer may change the barrier height with pressure. Moreover, the conduction-band effective mass is increased by the application of pressure due to the nonparabolicity effect,[5.32]   which affects both the subband energies and exciton binding energies in the quantum wells. The observed increase in a narrower wells is a combined effect of these factors. The work on InGaAs/GaAs systems could have had an uncontrollable parameter of alloy disorder in the well affecting the pressure coefficients for thin wells. Our experiments confirm the trend of the pressure coefficient dependence on the well width for strained layer systems without the influence of alloy disorder in the well.

We have measured the pressure coefficient of CdTe/Cd$_{1-x}$Mn$_x$Te SQWs with the same Mn content in the barriers for various well widths at 4 K. The pressure coefficient α is seen to depend on well width, which decreases for increasing well width in a similar way to strained InGaAs/GaAs systems but in contrast to the lattice matched GaAs/AlGaAs structures.

5.6   CdTe/Cd$_{1-x}$Mn$_x$Te QWs in a Magnetic Field

Perhaps the most interesting and unique property of the diluted magnetic semi-conductors (DMS) is the strong exchange interaction between the charge carriers and the magnetic ions. In bulk DMS, with increasing magnetic field the band gap decreases and the excitonic emission shifts to lower energies through Zeeman splitting of the localized levels. The tuning range depends on the magnetic concentration x and the magnetic splitting of the exciton energy is found to be a maximum for x ~ 0.2. The net total spin in bulk DMS decreases at higher concentrations by the formation of anti-ferromagnetic ordered clusters among the ions.[5.33] At temperatures below about 10 K (dependent upon the magnetic concentration), the charge carriers successfully orient

their magnetic spins around themselves forming the complexes known as bound magnetic polarons (BMP). Therefore, DMS systems are very sensitive to magnetic fields and their electronic structures are magnetically tunable.

CdTe/Cd$_{1-x}$Mn$_x$Te SLS and QWs correspond to type-I heterostructures. Through exchange interactions between the carriers and the magnetic ions, it is possible to tune the band gap of the magnetic layers, and hence the conduction band and valence band offsets, by applying a magnetic field. Thus the applied field can induce large changes of the carrier confinement energies and the exciton binding energies. Eventually if the changes of the band offset are large enough, a field induced transition of a superlattice from type I to type II may take place. Therefore, one has a useful magnetic control, after fabrication, of the barrier height in diluted magnetic semiconductor superlattices and quantum wells.

In semimagnetic materials, an important effect will be the dependence of the magnetic interactions on the mean Mn-Mn atomic separation in the Cd$_{1-x}$Mn$_x$Te layers. While this can be changed extensively by alloying different proportions of Mn, other factors will vary in an uncontrolled way from sample to sample. High pressure enables the Mn-Mn separation to be varied in a controlled way, over a few percent, while controlling and changing other factors in a known way.

Since the compressibilities of different semiconductors vary, there can be pressure-induced biaxial strains between semiconductors that share a common interface. Then, the applied pressure can allow sufficient tuning of mismatch in a single sample to simulate a wide range of materials at atmospheric pressure (1 atm.). Given these factors, magneto-optical spectroscopy under high pressures in CdTe/Cd$_{1-x}$Mn$_x$Te systems will greatly help in the analysis of electrical and optical processes occuring at atmospheric pressure and provide a direct determination of some of the important material parameters.

So far there have been few reports on the pressure dependence of the luminescence in CdTe/Cd$_{1-x}$Mn$_x$Te strained-layer structures,[5.23] and no reports on the magneto-optical studies of high pressure spectroscopy in DMS systems. Here we report for the first time the influence of hydrostatic pressure on the magneto-optical spectra of CdTe/Cd$_{1-x}$Mn$_x$Te multiple QWs and single QW structures with different x values.

5.6.1 Experimental Considerations

For high pressure measurements in magnetic field, the micro-diamond anvil cell (DAC) described in Section 2.3 was inserted in a cryostat equipped with a super-conducting magnet providing magnetic fields up to 8 Tesla at 4.2 K. In order to achieve optimal hydrostatic conditions, the pressure was changed at room temperature.

The magneto-optical investigations of high pressure spectroscopy were performed with two optical fibres which guide the ingoing laser beam and return the outgoing photoluminescence. All measurements were carried out with the magnetic fields parallel to the growth axis of the samples. The photoluminescence (PL) spectra were excited using the 488 nm line from an Argon-ion laser. The emitted light was dispersed by a 1m double-grating spectrometer and detected with a cooled GaAs photomultiplier tube using photon-counting technique. The spectra were recorded at liquid helium temperature.

The samples used were the same ones described in Section 5.4 and 5.5: M157 and M230. The first sample consists of five QWs with the same well width 100 Å, separated by 100 Å Cd$_{1-x}$Mn$_x$Te (x = 0.063) barriers. The second sample consists of four QWs with different well width from 20 − 150 Å, separated by 2000 Å Cd$_{1-x}$Mn$_x$Te (x = 0.125) barriers.

5.6.2 Magneto-Optical Spectra at Atmospheric Pressure

In this section we discuss the results of magneto-optical studies which yield information about the CdTe/Cd$_{1-x}$Mn$_x$Te MQWs (x = 0.063, L$_w$ = 100 Å) under atmospheric pressure (p = 1 bar).

Typical luminescence spectra for CdTe/Cd$_{1-x}$Mn$_x$Te MQWs (sample M157) with varying magnetic fields under atmospheric pressure and T = 4.2 K are shown in Fig. 5.14. Each of the spectra is normalized to its maximum intensity. The B = 0 T spectrum consists of two peaks A and B. The weak higher energy peak A is identified as the cap layer emission (x = 0.063). The very sharp peak B is attributed to free exciton recombination from the five quantum wells, all of the same well width (L$_w$ = 100 Å). In order to characterize the barrier layer material, a detailed optical study was made of the capping layer, grown with the same alloy composition.

In bulk Cd$_{1-x}$Mn$_x$Te, the Mn substitution leads to a component of the energy gap linear in x and increasing with x. From the energy of the heavy hole exciton at zero field, and the empirical relationship

$$E_x \text{ (meV)} = 1595 + 1587\,x \tag{5.16}$$

of Twardowski et al for Cd$_{1-x}$Mn$_x$Te at 2 K,[9] we find the manganese concentration to be about 6%. Therefore, the total band offset ΔE_g is about ~ 90 meV for MQWs M157. It is not precisely known how the band offsets in these quantum wells are shared between the conduction and valence bands, because a wide range of values for the relative valence-band offset $Q_v = \Delta E_v / \Delta E_g$ of the CdTe/Cd$_{1-x}$Mn$_x$Te systems is found in the literature ranging from 7 %[5.34] to 40 %.[5.35]
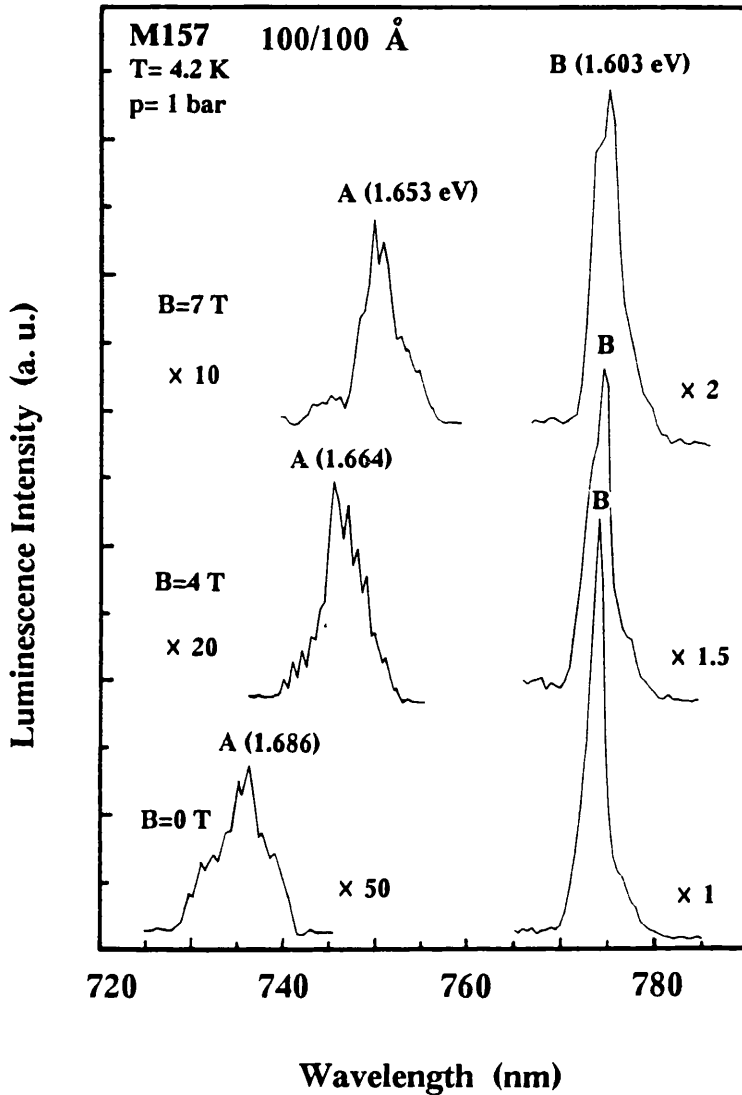
Fig. 5.14. The magnetic field dependence of the luminescence spectrum at atmospheric pressure 1 bar and T = 4.2 K for MQWs M157. Peaks A and B are the emissions from the $Cd_{1-x}Mn_xTe$ cap layer (x = 0.063) and the CdTe MQWs (L_W = 100 Å), respectively. The magnetic field is parallel to the growth axis of the sample.

An important feature of the data of Fig. 5.14 is the magnetic tunability of the exciton energy which arises through the Zeeman splitting. With increasing magnetic field

from 0 to 7 T, we can see the rapid evolution of peak A from the $Cd_{1-x}Mn_xTe$ cap layer containing 6.3 % Mn. The shift of the excitonic emission is of order ~ 33 meV at a field of 7 T. This result is easily understood through the magnetic field dependence of the exchange interaction. We also can see that peak B from the CdTe QWs has split into two components at 7 T. The spin splitting is enhanced by the presence of the magnetic Mn^{2+} ions in the $Cd_{1-x}Mn_xTe$ barrier layers, but is much smaller in magnitude than that of $Cd_{1-x}Mn_xTe$ as a result of the fact that the exciton is mainly confined within the CdTe quantum wells.

Fig. 5.15 depicts the influence of an applied magnetic field on a rectangular CdTe/ $Cd_{1-x}Mn_xTe$ QW. We emphasize here the role of the heavy-hole valence states while noting that the light-hole states are initially split from these at the Γ-point due to the uniaxial component of the lattice mismatch strain in both the CdTe well and $Cd_{1-x}Mn_xTe$ barrier layers (signs of strain are opposite). The field alters the quantum well potentials due to the spin splittings in the $Cd_{1-x}Mn_xTe$ barrier layers. The ability to magnetically "tune" the quantum well potentials provides a range of experimental data for accurate quantitative determination of the valence band offset in this system.

The Zeeman splitting of the ±3/2 heavy-hole exciton in the $Cd_{1-x}Mn_xTe$ layer for a manganese concentration x is given by[5.33]

$$\Delta E_{\pm 3/2}(B) = \pm 1/2 \, N_0 \, (\alpha - \beta) \, x <S_z>, \qquad (5.17)$$

where $<S_z>$ is given in equation (5.6); $N_0\alpha$ and $N_0\beta$ are the exchange interactions of electrons and holes with Mn ions, each with an electronic spin S = 5/2 and Lande' factor g = 2.

To a first approximation, the shift is proportional to the manganese magnetisation, which eventually saturates at high field. In addition, the electron-hole binding energy in

the exciton may also decrease with magnetic field and there may be contributions to the overall shift because of magnetic polaron formation in the barriers.
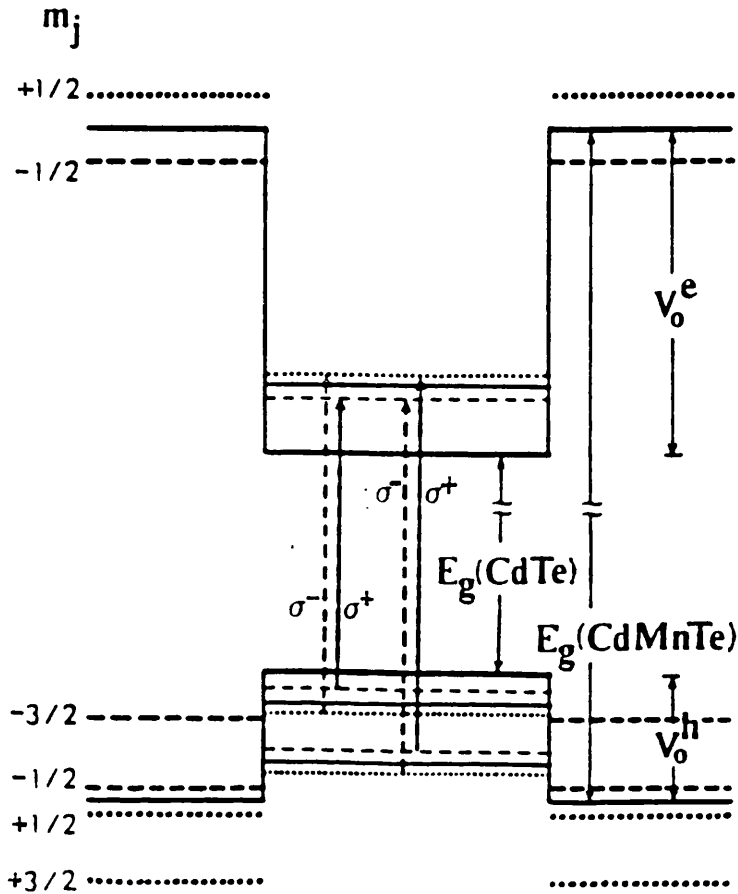
Fig. 5.15. Effect of a magnetic field on the band edges of a $CdTe/Cd_{1-x}Mn_xTe$ QW. The solid lines show the band edges in zero magnetic field, the dotted and dashed lines show the effect of applying a magnetic field. The σ^+ and σ^- optical transitions are shown by the vertical arrows. (After Nurmikko, 1988).[5.36]

Therefore, the magnetic field causes large exchange splittings in both the valence and the conduction bands of $Cd_{1-x}Mn_xTe$ layers which in turn result in changes of both the carrier confinement energies and the exciton binding energies in CdTe quan-

tum wells. From the capping layer data of MQWs M157, the change in the band offsets is about ~ 33 meV at 7 T. Because 80% of the total band gap variation of the heavy hole exciton is in the valence band,[5.33] the − 3/2 barrier band edge is found to change by about − 26 meV at 7 T. This is a large fraction, ~ 29%, of the band gap difference, $\Delta E_g \approx 90$ meV, between CdTe and $Cd_{1-x}Mn_xTe$. Thus we expect a type-I → type-II transition if

$$\Delta E_{-3/2}(B) - \Delta E_V = 0, \qquad\qquad (5.18)$$

when a magnetic field is applied and $Q_V = \Delta E_V / \Delta E_g$ is less than about 0.29. However, we did not observe the type-I → type-II transition up to magnetic fields of 7T. This also shows that the actual value of $\Delta E_V / \Delta E_g$ is larger than 0.29 for this sample.

It is clear that in Fig. 5.14, peak B from CdTe wells (L_w = 100 Å), in contrast to peak A from $Cd_{1-x}Mn_xTe$ layer, has no detectable exciton energy shift with the magnetic field over 7 T range. Although we expected to observe some spectral shifts from considering the finite penetration of the exciton wavefunction into the $Cd_{1-x}Mn_xTe$ layers, they were unexpectedly small. This result supports that reported by Awschalom et al (1989).[5.37, 5.38] Therefore, it is clear that both electrons and holes are mostly localized in the CdTe quantum wells, rather than in the $Cd_{1-x}Mn_xTe$ barrier layers, i.e. that the structure is of type-I.

It is not always the case that nonmagnetic well samples show this insensitivity to field. Other experiments have found large energetic shifts with field, using CdTe/$Cd_{1-x}Mn_xTe$ SL samples (x = 0.06 − 0.28, L_w = 16 − 97 Å) grown on (111) GaAs substrates and performing at 1.8 K and 5 T.[5.39]

Furthermore, we note that the exciton cannot be localized at the interfaces, since the shifts are much smaller (undetectable) than those reported for excitons trapped at such interfaces in certain CdTe/Cd$_{1-x}$Mn$_x$Te structures grown on GaAs.[5.40] The formation of interface states at the heterointerfaces of CdTe/Cd$_{1-x}$Mn$_x$Te structures may be related to the parameters employed during MBE film growth (substrate temperature, film growth rate, vapour flux ratios, etc.). In addition, strain effects are also expected to play a significant role in interface state formation.[5.39] However, it is not completely clear what sample characteristic is dominant in modifying the variation of the exciton energy with field.

Another important feature of Fig. 5.14 is that the capping layer (x = 0.063) peak A rapidly increases in intensity with increasing magnetic fields from 0 T to 7 T. The dominant contribution to the increase of the luminescence intensity with magnetic field arises from the increased electron-hole overlap, which results from the decrease of the excitonic Bohr radius in a magnetic field and from the increase of the exchange interaction between carrier spins and those of the magnetic ions.

In contrast, the well emission (peak B) decreases in intensity with magnetic field. This behaviour can be understood by considering the following: the external field reduces the quantum well confinement, since the barriers have now lower energies, and the holes in the wells move further into the barrier layers. The electrons, on the other hand, remain located near the well centre, because they experience a much higher barrier height in the conduction band. The electron-hole overlap is thus significantly reduced by applying a magnetic field. The relative displacement of the electron and the hole will decrease the binding energy with increasing magnetic field resulting in the decrease of the luminescence intensity of peak B.

5.6.3 Magneto-Optical Spectra under High Pressures

In figure 5.16 (a) we show the luminescence spectra for $CdTe/Cd_{1-x}Mn_xTe$ MQWs (sample M157) with varying magnetic fields under a hydrostatic pressure of ~ 7 kbar at T = 4.2 K. We observe that with varying magnetic field at ~ 7 kbar peak A, from $Cd_{1-x}Mn_xTe$ (x = 0.063) capping layer, shifts to a lower energy without significant spectral broadening and peak B, from CdTe quantum wells (L_w = 100 Å), has no detectable energy shift. The magnetic field dependences of the emission energies of peaks A and B are very similar to those at atmospheric pressure shown in Fig. 5.14.

Figure 5.16 (b) shows the variations of peak B from the CdTe QWs with field and pressure. It is very clear that peak B splits into two peaks with increasing field at 1.5 kbar and 7 kbar. The spin splitting (~ 3 meV at 7 T) is enhanced by the presence of the magnetic Mn^{2+} ions in the $Cd_{1-x}Mn_xTe$ barrier layers, but is much smaller in magnitude than that of $Cd_{1-x}Mn_xTe$ as a result of the fact that the exciton is mainly confined within the CdTe quantum wells.

Figure 5.17 shows the energy shifts of the luminescence peak A from $Cd_{1-x}Mn_xTe$ (x = 0.063) capping layer as a function of magnetic field at four different pressures and T = 4.2 K for sample M157. The luminescence energies decrease linearly at low fields and tend to saturate at higher magnetic field values. The external magnetic field leads to a destruction of the magnetic polaron due to an alignment of the Mn^{2+} spins. In a saturation regime the electron and hole spins are aligned with those of the Mn^{2+} ions. The overall PL energy decrease between 0 and 7 T is 33 ± 1 meV at atmospheric pressure compared to 35 ± 1 meV at 1.5 kbar. The smaller energy shift under atmospheric pressure is probably due to the fact that the exchange constant at atmospheric pressure is smaller than that at higher pressure, for example, ~ 1.5 kbar. It is clear that the top three curves remain essentially parallel in the main linear region, as a function of magnetic field at the pressures studied.
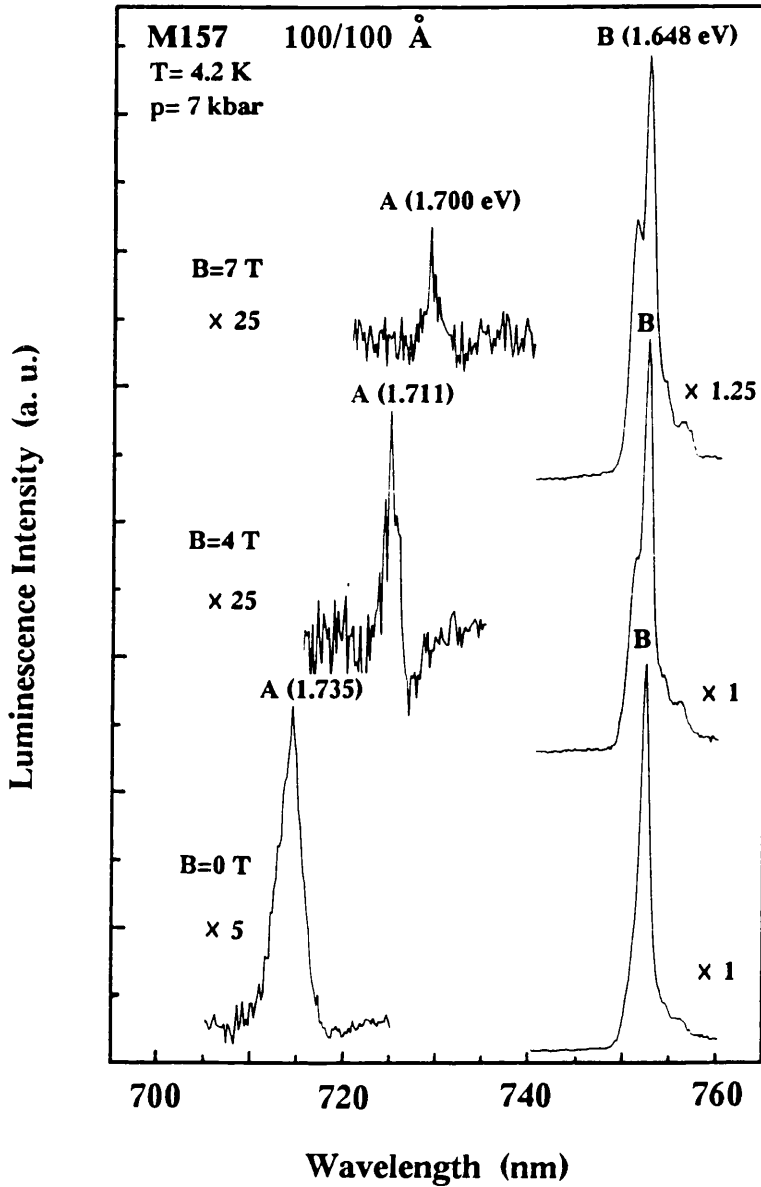
Fig. 5.16 (a). The magnetic field dependence of the luminescence spectrum under hydrostatic pressure (~ 7 kbar) at 4.2 K for MQWs (sample M157). Peaks A and B are the emissions from the $Cd_{1-x}Mn_xTe$ capping layer (x = 0.063) and the CdTe QWs (L_w = 100 Å), respectively. The magnetic field is parallel to the growth axis of the sample.
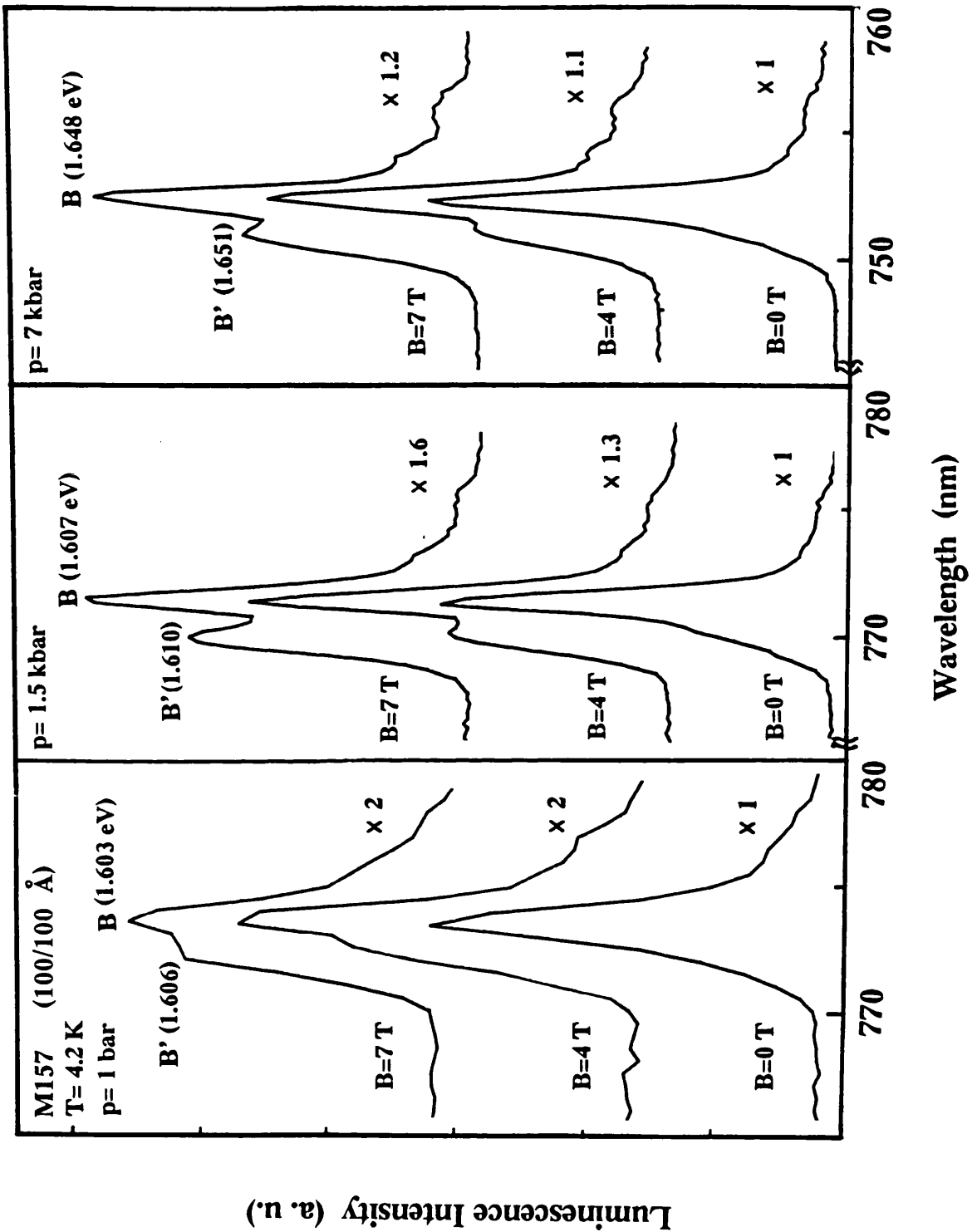
Fig. 5.16 (b)   The variations of peak B from the CdTe QWs with field and pressure.
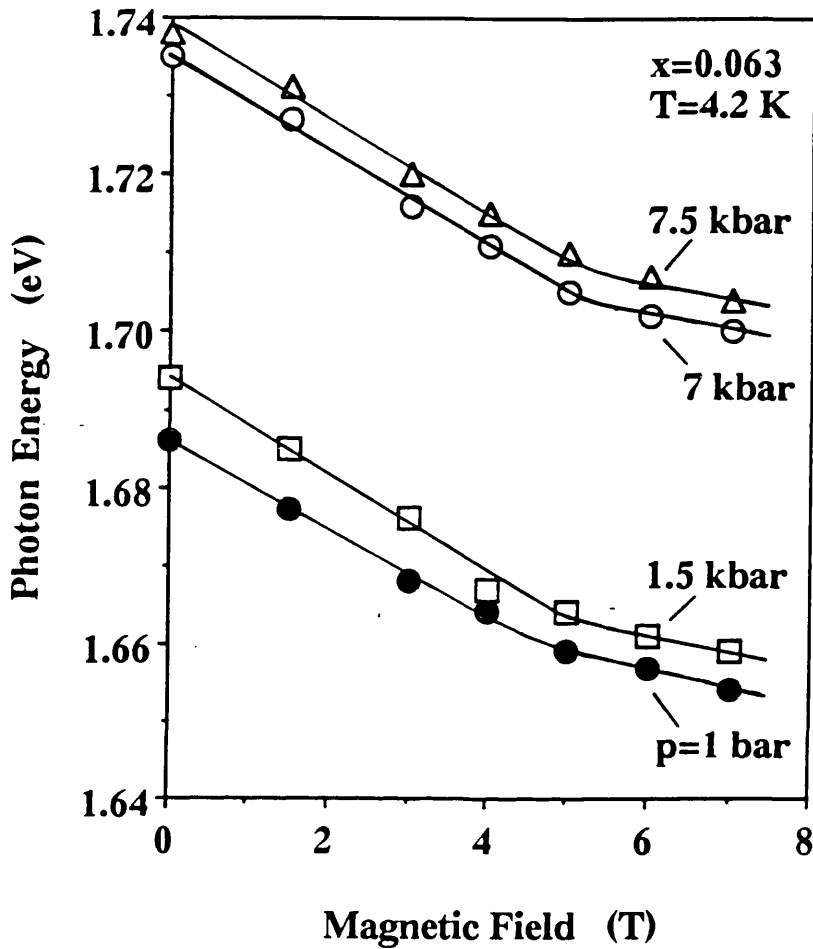
Fig. 5.17. The energy shift of the emission from the $Cd_{1-x}Mn_xTe$ (x = 0.063) capping layer (peak A) as a function of magnetic field at four different pressures 1 bar, ~ 1.5, ~ 7 and ~ 7.5 kbar and 4.2 K for sample M157. The solid lines are a guide to the eyes.

We now discuss the intensity changes in the emission from the cap layer (peak A) with magnetic field. With increasing magnetic field there is a drastic reduction in the luminescence intensity from the cap (barrier) layers (peak A) under hydrostatic pressure ~ 7 kbar. Compared with peak A in Fig. 5.14, the most important observation that can be made from Fig. 5.16 (a) is the striking contrast of the magnetic field dependence of

the luminescence intensity of peak A at two different pressures 1 bar and 7 kbar: at 1 bar the emission from the cap/barrier layer is much weaker at 0 T than at 7 T, but at 7 kbar it is much stronger at 0 T than at 7 T. This is somewhat puzzling but the same dependence as that under ~ 7 kbar was also observed at pressure ~ 7.5 kbar.

In Fig. 5.18. we show the variations of the relative emission intensity of peak A from $Cd_{1-x}Mn_xTe$ (x = 0.063) capping layer with magnetic field at four different pressures and T = 4.2 K for sample M157. For atmospheric pressure 1 bar and lower pressure ~ 1.5 kbar, the luminescence intensities increase with the field (see Fig. 5.18 (a)), but for higher pressures ~ 7 and ~ 7.5 kbar, then decrease with the field (see Fig. 5.18 (b)).

It is important to discuss why the magnetic field dependences of the relative emission intensity are so different in the two different pressure ranges. For the DMS systems, the usual exciton equation is augmented by a spin exchange term H_{ex} (see equation (5.5)). Considering that the application of high pressures reduces the inter-atomic separation, this will also be ture for the distance between the carrier and the magnetic ion. J ($r - R_n$) is the position-dependent electron-ion exchange constant which falls off rapidly with the distance from a Mn site. Therefore, under high pressures the exchange constant J ($r - R_n$) is larger than that at zero pressure. The sp-d hybridization is expected to increase on applying pressure. This can very well explain why at B = 0 T the relative emission intensity of peak A at ~ 7 kbar (see Fig. 5.16. a) is much stronger than that at 1 bar (see Fig. 5.14).

In addition, the presence of an external magnetic field reduces magnetic polaron effects. Thus, if the exchange effects are strong enough, at a certain field the net binding energy will vanish. This will then result in a rapid decrease of the emission intensity with the magnetic field, which is similar to what we observed in Fig. 5.18 (b).
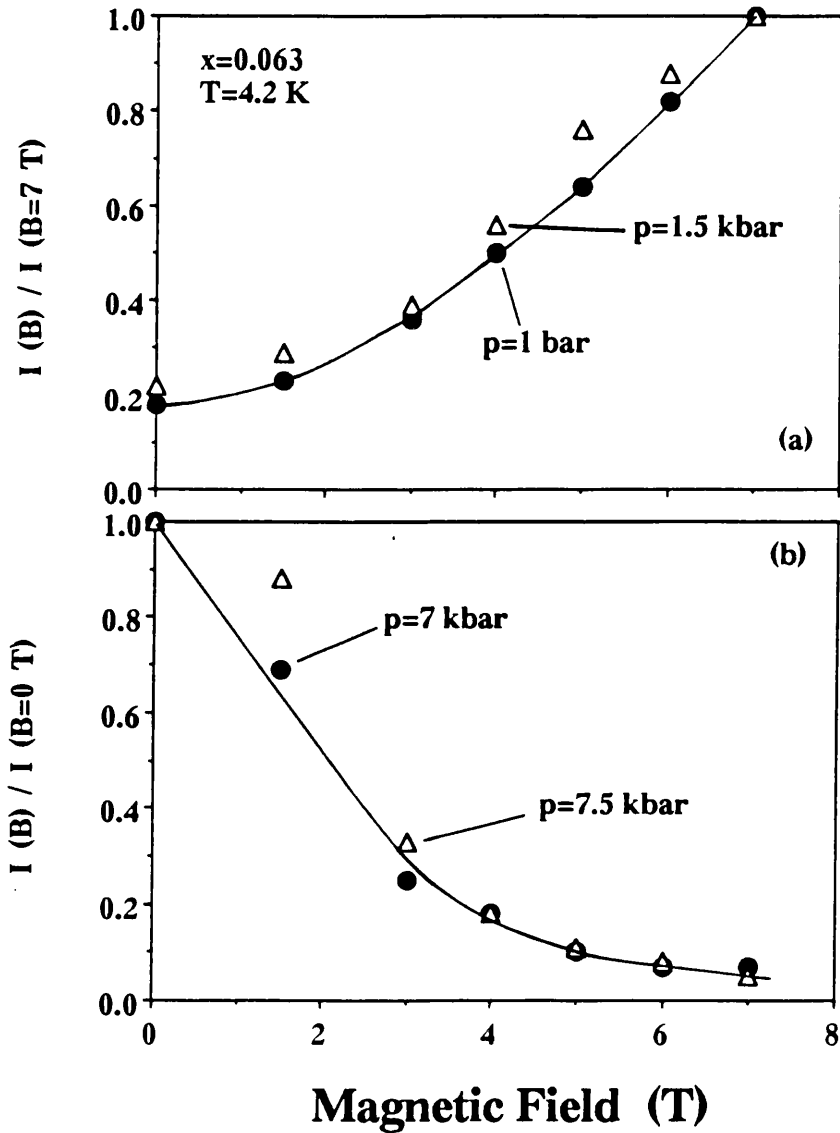
Fig. 5.18. The relative emission intensity of peak A from the $Cd_{1-x}Mn_xTe$ (x = 0.063)
capping layer as a function of magnetic field at four different pressures and
4.2 K for sample M157. (a): I (B) / I (B = 7 T) at pressures 1 bar and ~ 1.5
kbar; (b): I (B) / I (B = 0 T) at pressures about ~ 7 and ~ 7.5 kbar. The
solid lines are a guide to the eyes.

We may think that applying high pressures is somewhat similar to increasing the magnetic ion concentration x. For small Mn concentrations (x < 0.1), the materials are essentially paramagnetic, and the magnetic polaron binding energy increases with x. For x > 0.1, the antiferromagnetic Mn^{2+} - Mn^{2+} interaction will play an important role in determining the polaron binding energy.

In particular, for materials with larger x values, there is a competition between the strong carrier- Mn^{2+} exchange interaction, which tends to align Mn^{2+} spins parallel to that of the carrier, and the direct Mn^{2+} - Mn^{2+} interaction which favours antiferro-magnetic alignment. It may be possible that under higher pressures sample M157 behaves as if its x value were near the critic value 10% Mn, even though it actually contains 6.3% Mn.

To confirm our arguments, we investigated the SQWs (sample M230) with larger magnetic concentration (x = 0.125). In Fig. 5.19, we show the variations of the relative emission intensity from $Cd_{1-x}Mn_xTe$ (x = 0.125) capping layer with magnetic field at two different pressures and 4.2 K for sample M230. The luminescence intensity decreases with increasing field at atmospheric and higher pressures. Comparing these results with those of sample M157 at ~ 7 and ~ 7.5 kbar, it is clear that this variation trend is very similar to that in Fig. 5.18 (b).

Thus, these results confirmed our hypothesis that the magneto-optical spectra can be changed from that of a lower x value to that of a higher one by hydrostatic pressures in DMS systems. One final observation is that the rate of decrease of emission intensity with magnetic field is slower for the sample with 12.5% Mn suggesting that the mechanisms involved are somewhat more complex.
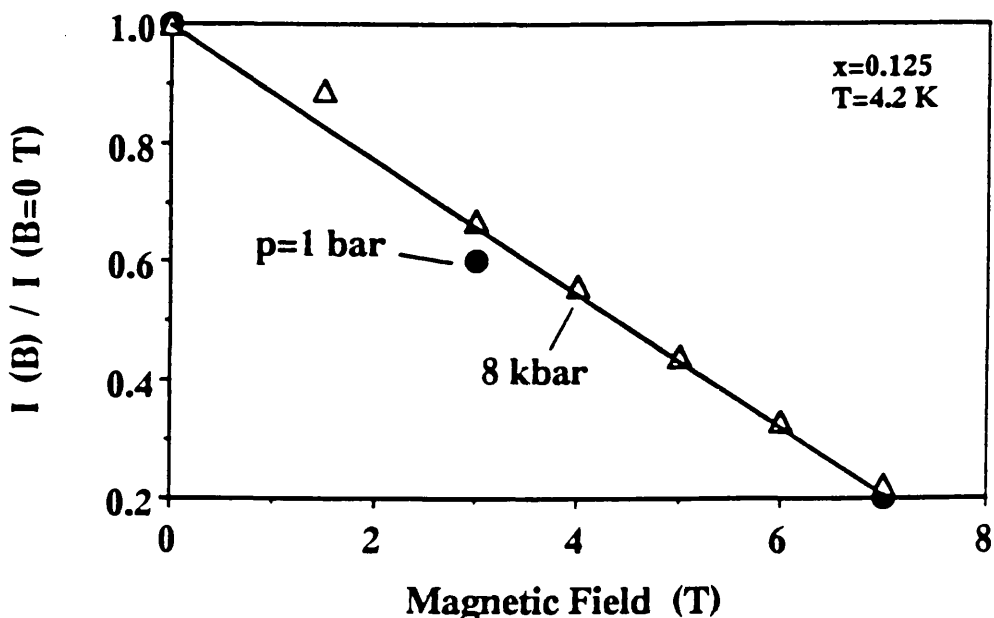
Fig. 5.19. The relative intensity I (B) / I (B = 0 T) of the emission at 4.2 K from the $Cd_{1-x}Mn_xTe$ capping layer (x = 0.125) as a function of magnetic field at two different pressures 1 bar and ~ 8 kbar for sample M230. The solid line is a guide to the eyes.

The energy shifts of the luminescence from the capping layer (x = 0.125) for sample M230 at 4.2 K as a function of magnetic field at two different pressures are plotted in Fig. 5.20. The luminescence energies decrease almost linearly at low fields and tend to saturate at higher magnetic field values, which is similar to the trend observed in sample M157 (x = 0.063).

With respect to the overall energy shift from 0 to 7 T, at 1 bar the luminescence energy shifts ~ 27 meV, whereas at ~ 8 kbar it shifts ~ 39 meV. These much larger energy shifts with pressure compared to those of sample M157, arise from the fact that the exchange constant depends on Mn concentration and in the sample with higher concentration the application of pressure has a stronger effect.
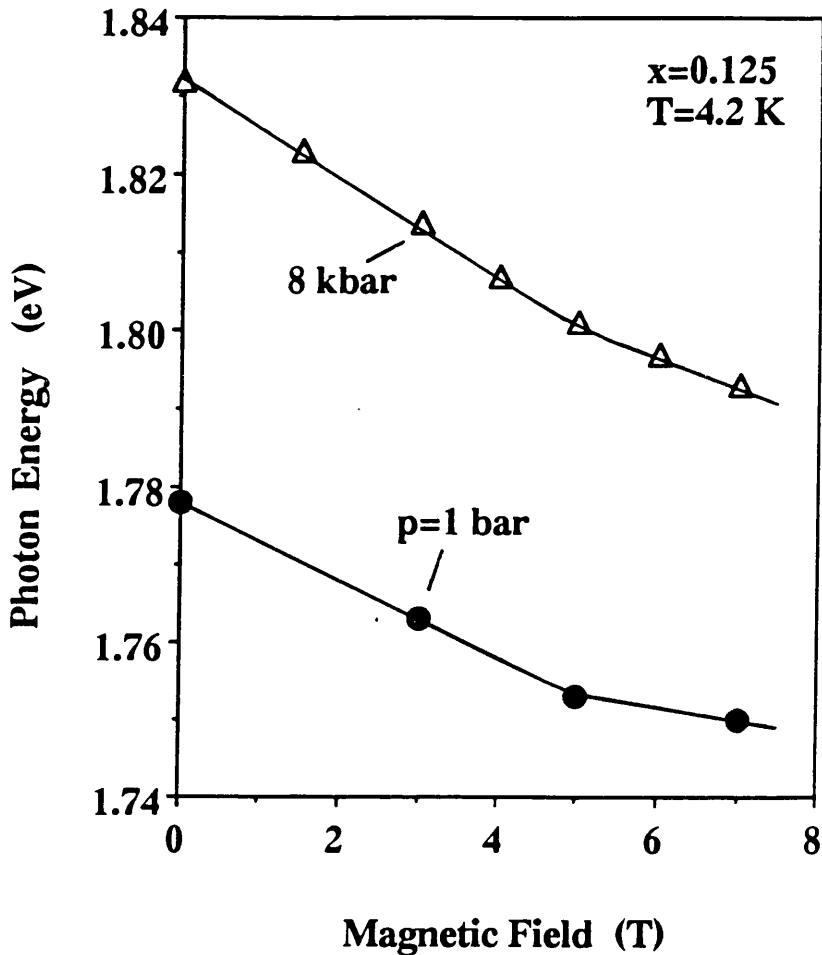
Fig. 5.20. The energy shift of the emission from the $Cd_{1-x}Mn_xTe$ capping layer (x = 0.125) as a function of magnetic field at two different pressures 1 bar and ~ 8 kbar and 4.2 K for sample M230. The solid lines are a guide to the eyes.

Furthermore, for sample M230 a very small exciton energy shift of the quantum well (L_w = 20 Å) with magnetic fields can be observed under atmospheric pressure (2 ± 1 meV from 0 to 7 T) as shown in Fig. 5.21. However, at 8 kbar there is a larger energy shift 22 ± 1 meV over the same field range. A similar trend was observed at ~ 6 kbar.
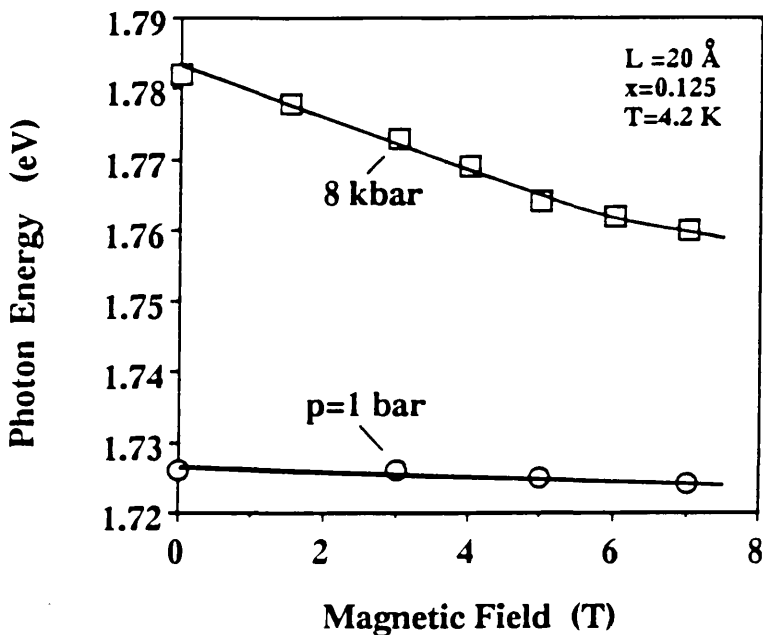
Fig. 5.21. Variations of the exciton energy of the quantum well ($L_w = 20$ Å) at 4.2 K as a function of magnetic field at two different pressures of 1 bar and ~ 8 kbar for sample M230. The solid lines are a guide to the eyes.

The most important observation that can be made from Fig. 5.21 is the dramatic difference of the magnetic field dependence of the free exciton energy in the quantum well ($L_w = 20$ Å) under zero and high pressures. These results substantially differ from those of sample M157 where the well exciton energy was almost insensitive to the magnetic field (see peak B in Fig. 5.14 and Fig. 5.16). This phenomenon appears to originate from the exchange interaction between the exciton in the well and the Mn-ion spins in the barrier layers.

We recall that the $CdTe/Cd_{1-x}Mn_xTe$ quantum well structure is a type-I QW, consisting of a nonmagnetic well and a magnetic barriers. The valence band offset is known to be small. The variations of the exciton energy with magnetic field will depend strongly on the wavefunction penetration of the optically excited carriers into the barrier layers, changing as the confinement energy of the carriers is varied.

When a magnetic field is applied, the magnetisation of manganese ions in the barriers is altered. This causes a reduction in the bandgap and produces changes in the potential well depths seen by the electrons and holes in the CdTe well. As a result, the confinement energies are altered. The extent of the penetration of the carrier wavefunctions into the barriers also changes.

If the carrier wavefunction is confined mainly to the well with little penetration into the barriers, the magnetic tuning cannot be observed as the magnetism is induced primarily in the barrier layers. This is expected to be the case for sample M157 (L_w = 100 Å) at atmospheric and higher pressures and to some degree in sample M230 (L_w = 20 Å) at atmospheric pressure.

Considering that a well width of 20 A approaches the narrow width limit, the well will become narrower under high pressures. In addition, the different compressibilities of the semiconductors may introduce biaxial strains. If CdTe is "harder" than CdMnTe ($\alpha_{CdTe} < \alpha_{CdMnTe}$), then the biaxial strain in the well will have a compressive component, raising the confined energy levels further and probably enhancing penetration of the well exciton wavefunction into the barrier. Therefore, the applied pressure can vary the mismatch of this sample and the strain in the well. Given these two factors, the wavefunction penetratation may be more significant, a larger part of the induced magnetization signal is associated with alignment of the spins in the $Cd_{1-x}Mn_xTe$ barriers.

Furthermore, the smaller energy shift of ~ 22 meV of the ground-state exciton transition (which originates and terminates in the nonmagnetic well) is a manifestation of the partial penetration of the wavefunctions of the initial and the final states into the magnetic barriers. By contrast, the larger energy shift of ~ 39 meV (see Fig. 5.20) indicates that this transition originates and terminates on states localized predominantly in the $Cd_{1-x}Mn_xTe$ layer.

5.7 Summary

The photoluminescence (PL) of CdTe/$Cd_{1-x}Mn_xTe$ MQWs and SQWs with well widths from 20 to 150 Å has been investigated as a function of hydrostatic pressure (1 bar – 35 kbar) at liquid-helium temperature. No band crossovers were observed before the phase transition at ~ 33 kbar. Pressure coefficients of the E^Γ_{1h} transitions between the quantized ground levels of the Γ-conduction band and the heavy-hole valence band are presented for various well widths. The pressure coefficient is found to increase with decreasing well widths, as in InGaAs/GaAs strained quantum wells but unlike that observed in the GaAs/AlGaAs quantum well system.

The magneto-optical spectra of CdTe/$Cd_{1-x}Mn_xTe$ quantum wells have been investigated as a function of hydrostatic pressures at liquid helium temperature. DMS systems are very sensitive to magnetic fields and their band gaps are magnetically tunable. The band gap of the $Cd_{1-x}Mn_xTe$ barrier layers decreases with increasing magnetic fields.

On the other hand, for CdTe/$Cd_{1-x}Mn_xTe$ MQWs (x = 0.063), the CdTe wells (L_w = 100 Å) have no detectable exciton energy shift with magnetic field at atmospheric and higher pressures. In contrast, for CdTe/$Cd_{1-x}Mn_xTe$ SQWs (x = 0.125), the CdTe well (L_w = 20 Å) has large energy shifts with field under high pressures. These observations are qualitatively explained by the degree of penetration of the electron-hole pair wavefunction into the DMS barrier layers with high pressure acting in a similar manner as increasing the Mn concentration. It is not completely clear what sample characteristic is dominant in modifying this conclusion, but strain is the leading candidate.

Ch. 6   CONCLUDING REMARKS

6.1.   Results of This Thesis

The running theme of this thesis has been the use of high pressure in hydrostatic and uniaxial form, applied after sample growth or built-in during sample growth.

It has been shown here that the application of hydrostatic pressure is a valuable variable in: (i) aiding the understanding of the origin of the low temperature emission in semiconductor alloys, such as AlInAs and (ii) modifying the strength of magnetic ions interactions in dilute magnetic semiconductors, such as CdMnTe-CdTe quantum wells.

On the other hand, highly strained superlattices were shown to be mechanically unstable over a period of time in the month-scale. Nevertheless the study of their optical properties over a short period of time allowed an insight into the optical processes in type II superlattices.

6.1.1.   Optical Properties of $Al_{0.48}In_{0.52}As$ under High Pressures

Until this work was completed no detailed studies of the low-temperature luminescence of $Al_{0.48}In_{0.52}As$ under high pressures were available to the best of our knowledge. The motivation for this work was to identify the low-temperature emission and to provide the first detailed high pressure investigation of the luminescence properties of $Al_{0.48}In_{0.52}As$, grown lattice matched to InP.

Previous work had suggested that the low-temperature emission of $Al_{0.48}In_{0.52}As$ was due to band-to-band transitions or bound excitons,[3.6] and other assignments such as free-to-bound and donor-acceptor-pair transitions were also considered: PL work on $Al_{0.48}In_{0.52}As$ under hydrostatic pressure,[3.7] which yielded a linear pressure coefficient of the direct-conduction band gap of 10.1 meV/kbar at 80 K, ascribed the 80

K emission to free-to-bound.

We investigated the low-temperature PL and PLE spectral characteristics of $Al_{0.48}$-$In_{0.52}As$ under high pressures from 1 bar up to 92 kbar. Our results provide an insight into the luminescence processes that occur in $Al_{0.48}In_{0.52}As$, especially with respect to the changes in luminescence mechanisms that occur concurrently with the crossover between the direct- and indirect-related bands. At the same time these studies have furnished important data on the pressure behaviour of impurity states in the alloy.

We observed the band-to-band and the bound-to-free transitions in the PLE spectra and found a large shift between the PL and the PLE spectra, ~ 74 meV. By investigating the temperature and excitation-power dependences of the PL spectra together with the PLE spectra, we demonstrated that the low-temperature emission of the $Al_{0.48}In_{0.52}As$ is not excitonic but due to (D^O, A^O) transitions with a relatively deep acceptor of ~ 68 meV, which occurs in both the direct- and in the indirect-band gap.

At low temperature, the main change in the appearance of the spectrum, as one goes from direct gap to indirect gap, is the abrupt variation of the pressure coefficients at ~ 52.5 ± 0.5 kbar. However, the emission intensity does not change drastically. The linear pressure coefficient α^Γ of the (D^O, A^O) band related to the Γ minimum in the conduction band of $Al_{0.48}In_{0.52}As$ was found to be 7.9 ± 0.1 meV/kbar, which is almost the same as that of bulk InAs (8 meV/kbar),[3.9] but significantly lower than that of $Al_{0.48}In_{0.52}As$ at 80 K.[3.7] The linear pressure coefficient α^X of the (D^O, A^O) band related to the X minimum in the conduction band was found to be − 2.9 meV/kbar, which is close, but not equal to that of bulk GaAs (− 1.8 meV/kbar at 110 K).[3.10]

There is evidence for the donor-acceptor level. The acceptor level is quite deep with a binding energy of 68 ± 1 meV. Moreover, emission from a DX-like level is observed

above p_c , the energy of which is independent of pressure.

We also find that the transition of the (D^O, A^O) band from a direct-pair band to an indirect one (i.e., a pair band that follows the indirect-conduction band pressure dependence) occurs abruptly within the resolution of the present data in that the indirect emission appears clearly above p_c. In the intermediate range 50 kbar < p < 55 kbar, direct (D^O, A^O) recombination occurs together with indirect pair recombination. Thus significant mixing occurs over a pressure range of less than 5 kbar.

Finally , we suggest that the shallow donor ground states associated with the X- and the Γ- conduction bands seem to be tied quite rigidly to these conduction bands since variations in the donor binding energies with pressure and near the direct-indirect crossover seem to be minor in the PL and PLE spectra.

6.1.2. Optical Properties of GaAs/GaP Strained-Layer SL

GaAs/GaP strained-layer superlattices are the limit case (x = 1, maximum lattice mismatch) for the system GaP/GaAs$_x$P$_{1-x}$, in which the lattice mismatch is 3.7 %. Optical studies of this kind on strongly strained-layer GaAs/GaP superlattices grown on GaAs substrates have been reported previously.[4.9, 4.10] In this work, we investigated the optical characterization of a type-II GaAs/GaP strained-layer superlattice grown by atomic layer molecular-beam epitaxy (ALMBE) on GaAs substrate. Photoluminescence (PL) and photoluminescence excitation (PLE) measurements were carried out. By combining these two techniques and observing the PL evolution as a function of temperature and excitation power we identified the origin of the observed transitions.

For (GaAs)$_6$/(GaP)$_6$, the lowest conduction band is X level in GaP layers. The energy separation between X-level in GaP layers and Γ-level in GaAs layers is ~ 44

meV at 75 K. Electron transfer effects between states confined in GaAs and GaP layers were observed when the excitation power and temperature are raised, in the form of emission intensity variation of both the X- and Γ-related emission bands. The intensity changes are well explained in terms of lifetime and density of states of the electron valleys involved.

The temperature dependence of the PL spectra for this type-II $(GaAs)_6/(GaP)_6$ SLS is found to be different from previously reported results.[4.10]   We have probably observed, for the first time, the strain relaxation induced optical transitions, which would be associated with defects or impurities related to Γ- and X-states. However, the broad emission lines precluded further studies on the precise nature of these suggested strained-induced transitions.

Because of the large lattice mismatch in GaAs/GaP systems, the samples are highly strained structures. We found that the type-II $(GaAs)_6/(GaP)_6$ SLS is mechanically unstable as revealed by the energy separation between X- and Γ-levels changing with time. Thus, we have pointed out a crucial problem in this kind of systems, namely temporal strain relaxation, which probably pre-empts device applications of this material system.

6.1.3.   Magneto-Optical Studies of CdTe/CdMnTe QWs under High Pressures

Although the optical and electronic properties of $CdTe/Cd_{1-x}Mn_xTe$ SLs and QWs had been studied in some detail, a substantial number of questions remain concerning the basic electronic structure and properties of the systems. Compared with the more widely studied III-V SLs and QWs, notably the GaAs/(GaAl)As system, few of the fundamental parameters necessary for the engineering of CdTe based devices were

known. Such parameters are particularly important in the strained layer SLs and QWs.

In this work the photoluminescence (PL) of CdTe/Cd$_{1-x}$Mn$_x$Te MQWs and SQWs with well widths from 20 to 150 Å has been investigated as a function of hydrostatic pressure (0 - 35 kbar) at liquid-helium temperature. No band crossovers were observed before the phase transition at ~ 33 kbar. The absence of band crossover augurs well for devices which rely on electron confinement since the deleterious effects associated with contributions from X-levels are expected. Pressure coefficients of the E^{Γ}_{1h} transitions between the quantized ground levels of the Γ conduction band and the heavy-hole valence band were determined for various well widths. The pressure coefficient is found to increase with decreasing well widths, as in InGaAs/GaAs strained quantum wells but unlike that observed in the GaAs/AlGaAs quantum well system. The limit of the narrowest well in this study compares well with the pressure coefficient of CdMnTe.

The magneto-optical spectra of CdTe/Cd$_{1-x}$Mn$_x$Te quantum wells were investigated as a function of hydrostatic pressures at liquid helium temperature. DMS systems are very sensitive to magnetic fields and their band gaps are magnetically tunable. As expected, the band gap of the Cd$_{1-x}$Mn$_x$Te barrier layers decreased with increasing magnetic fields.

On the other hand, for CdTe/Cd$_{1-x}$Mn$_x$Te MQWs (x = 0.063), the CdTe wells (L$_w$ = 100 Å) have no detectable exciton energy shift with field under zero and high pressures. In contrast, for CdTe/Cd$_{1-x}$Mn$_x$Te SQWs (x = 0.125), the CdTe well (L$_w$ = 20 Å) has large energy shifts with field under high pressures. These behaviours were explained by the degree of penetration of the electron-hole pair wavefunction into the DMS barrier layers. It is not completely clear which sample characteristic is dominant in modifying this conclusion.

We found that the magnetic field dependence of the luminescence intensity of the $Cd_{1-x}Mn_xTe$ layers can be dramatically changed by high pressures due to the variations of the distance between the carriers and the Mn ions with pressure. This result provides a use in the design of future optical devices requiring band-to-band recombination as the sample characteristics for maximum intensity can now be determined from this data.

6.2.   Future Research Work

Here, we concentrate mostly on DMS, the properties of which have been discussed in chapter 5 together with the contribution of this research.

An obvious extension of the work on CdTe/CdMnTe is the patterning of these quantum wells into nanostructures of dimensions comparable to the de Broglie wavelength, i.e., less than 100 nm. The spatial confinement of the electronic wavefunction to 1- and 0-dimensions has given rise to many attractive predictions related to optical transitions and quantum transport properties, including: a) the increase overlap of the electron and hole wavefunctions is predicted to enhance the oscillator strength; b) the density of states in the 0-D limit tends to concentrate more and more carriers in quantum states; c) the restrictions on the values of the wavevector **k** suggest an increased carrier mobility in 1-D due to limited scattering processes. Therefore, the field of II-VI nanostructures is wide open, particularly, exciton and phonon-related phenomena focussing on the influence of lower dimensional effects.

6.2.1.   Phonon-Related Phenomena in Low-Dimensional II-VI

The phonon lattice vibrations and Zeeman splittings in 2- and 1-D can be studied by resonant-Raman-scattering (RRS) with circularly polarized components in external magnetic fields and high pressures. RRS by phonons provides the link between electronic and lattice-dynamical properties: the energy dependence of the Raman efficiency and its absolute value are determined by electron-phonon interaction and by

parameters of the band structure, such as gap energy, effective masses and broadening.

RRS by LO phonons is particularly interesting because both short- and long-range parts of the electron-phonon interaction are present. The short-range part can be represented by deformation potentials, while the long-range part, the Fröhlich interaction, arises from the electric field generated by LO phonons in polar semiconductors. An important aspect is the character of optical phonons in 1-D as novel predictions of phonon hybridization in wires are emerging in the literature. The high Raman efficiency of these II-VI materials makes them a superior candidate for such work.

The DMS materials show in general characteristically very large Zeeman effects at the lowest interband excitonic transitions, emanating from the exchange coupling between the exciton s-p (Bloch) states and those of the Mn-ion d-electrons. Zeeman spectroscopy can yield direct quantitative information about the degree of penetration of the electron-hole pair wavefunction into the DMS barrier layers (and hence quantum well confinement and band offsets). In this thesis only qualitative information on this topic was presented.

6.2.2. Magnetic Polarons and Dimensional Effects

A particularly attractive study concerns the effects of changes in dimensionality (to 1- and 0-D) on magnetic phenomena. For example, probing the magnetic behaviour on a local scale by exploiting the strong spin-spin interaction between the carriers and the magnetic ions and observing the effects of quantum-confined carriers on the magnetic properties of the system.

In nanostructures, spin polarized carriers can induce a magnetization whose spatial extent will be completely determined by the quantum mechanical wavefunctions of the confined carriers. Therefore, with low-dimensional DMSs, one may construct a tailored

potential to shape the electronic wavefunctions and vary the length scale of the magnetic probe, thereby providing an opportunity to study quantum phenomena in a new manner.

6.2.3.   Theoretical Work in II-VI DMS Nanostructures

Theoretically, this field would deal with the electronic structures, light emitting mechanisms, emission efficiency and strength of quantum interactions in II-VI nanostructures, such as electron-photon and spin-exchange interactions. Theoretical study of the electronic structure of II-VI QWs and SLs is highly complex and worthy of research, because of the number of overlying effects of comparable magnitude which enter the basic Hamiltonian.

REFERENCES

1.1. L. Esaki and R. Tsu, IBM J. Res. Dev. **14**, 61 (1970).

1.2. C. Weisbuch, in: "Physics and Applications of Quantum Wells and Superlattices", Nato ASI series. Series B; Physics Vol. **170** Plenum Press, NY. pp. 261 (1987).

1.3. J. J. Hopfield, Phys. Rev. **112**, 1555 (1958).

1.4. W. Heitler, "The Quantum Theory of Radiation", Dover, New York (1984).

1.5. C. Weisbuch, in: "Physics and Applications of Quantum Wells and Superlattices", Nato ASI series. Series B; Physics Vol. **170** Plenum Press, NY. pp. 261 (1987).

1.6. G. A. Samara, Physica **B 139 & 140**, 3 (1986).

1.7. S. Lee, J. Sanchez-Dehesa, and J. D. Dow, Phys. Rev. **B 32**, 1152 (1985).

1.8. C. Pickering and A.R. Adams, J. Phys. C: Solid State Phys. **B 10**, 3115 (1977).

1.9. Murnaghan, Proc. Natl. Acad. Sci. U.S.A. **30**, 244 (1944).

1.10. M. Jaros, Rep. Prog. Phys. B 48 B, 1091 (1985).

1.11. M. Cardona and N. E. Christensen, Phys. Rev. **B 35**, 6182 (1987).

1.12. D. Bertho, D. Boiron, A. Simon and C. Jouanin, Phys. Rev. **B 44**, 6118 (1991).

1.13. B. Rockwell, H. R. Chandrasekhar and M. Chandrasekhar, Phys. Rev. **B 44**, 11307 (1991).

1.14. J. Bardeen and W. Shockley, Phys. Rev. **8 0**, 72 (1950).

1.15. D. Bertho, D. Boiron, A. Simon and C. Jouanin, Phys. Rev. **B 44**, 6118 (1991).

1.16. R. People, A. Jayaraman, K. W. Wecht, D. L. Sivco and A. Y. Cho, Appl. Phys. Lett. **5 2**, 2124 (1988).

1.17. I. T. Ferguson, T.P. Beales, T. S. Cheng, C.M. Sotomayor Torres and E. G. Scott, Semicond. Sci. Technol. **4**, 243 (1989).

1.18. U. Venkateswaran, M. Chandrasekhar, H. R. Chandrasekhar, B. A. Vojak, F. A. Chambers and J. M. Meese, Superlattic. Microstruc. **3**, 217 (1987).

1.19. D. J. Wolford, T. F. Kuech, J. A. Bradley, M. A. Gell, D. Ninno and M. Jaros, J. Vac. Sci. Technol. **B 4**, 1043 (1986).

1.20. P. Lefebvre, B.Gil and H.Mathieu, Phys. Rev. **B 35**, 5630 (1987).

1.21. P. Lefebvre, B.Gil, J.Allegre, H.Mathieu, Y.Chen, and C.Raisin, Phys. Rev. **B 3 5**, 1230 (1987).

1.22. G. H. Li, D. S. Jiang, H. X. Han, Z. P. Wang and K. Ploog, Phys. Rev. **B 4 0**, November (1989).

1.23. U. Venkateswaran, M. Chandrasekhar, H. R. Chandrasekhar, B. A. Vojak, F. A. Chambers and J. M. Meese, Phys. Rev. **B 33**, 8416 (1986).

1.24. L. D.L. Brown, M. Jaros, and D.J. Wolford, Phys. Rev. **B 40**, 6413 (1989).

1.25. G. C. Osbourn, IEEE J. Quantum Electron. QE-2 **2**, 1677 (1986).

1.26. C. Pickering and A.R. Adams, J. Phys. C: Solid State Phys. **1 0**, 3115 (1977).

1.27. G. C. Osbourn, IEEE J. Quantum Electron. QE-2 2, 1677 (1986).

1.28. F. H. Pollak, in Strained-Layer Superlattices: Physics, edited by T. P. Pearsall (Academic, Boston, 1990).

1.29. C. G. Van de Walle, Phys. Rev. B 39, 1871 (1989).

1.30. B. Rockwell, H. R. Chandrasekhar and M. Chandrasekhar, Phys. Rev. B 44, 11307 (1991).

1.31. H. Q. Hou, Y. Segawa, Y. Aoyagi and S. Namba, Phys. Rev. B 42, 1284 (1990).

1.32. K. Shahzad, D. J. Olego, C. G. Van De Walle and D. A. Cammack, J. of Luminescence 46, 109 (1990).

1.33. H. Barry Bebb and E. W. Williams, "Photoluminescence I: Theory", in "Semiconductors and Semimetals" Vol. 8, R. K. Willardson and A. C. Beer eds., pp. 182, Academic, New York (1972).

1.34. R. J. Elliot and A. F. Gibson, "Solid State Physics", Pub. Macmillan Press Ltd, London, (1982).

1.35. B. Cavenett, in "Luminescence Spectroscopy", Ed. M. D. Lumb, Academic Press, NY, (1978).

1.36. E. F. Schubert and K. Ploog, J. Phys. C 18, 4549 (1985).

1.37. B. Hamilton, "Low-Dimensional Structures in Semiconductors", Edited by A. R. Peaker and H. G. Grimmeiss, Plenum Press, New York, 1991, pp 37.

1.38. P. J. Dean, Prog. Cryst. Growth Charact. 5, 89 (1982).

1.39. R. C. Miller and D. A. Kleinman, J. Lumin. 3 0, 520 (1985).

1.40. G. Bastard and J. A. Brum, IEEE J. Quantum Elect. **22**, 1625 (1986).

1.41. J. C. Maan, in: "Magneto-Optical Properties of Heterojunctions, Quantum Wells and Superlattices", Nato ASI series, Series B; Physics Vol. **170**, Plenum Press, NY. pp.347 (1987).

1.42. J. Singh and K. Bajaj, Appl. Phys. Lett. **44**, 1075 (1984).

1.43. L. Esaki, IEEE J. Quantum Elect. **22**, 1611 (1986).

2.1. W. Rodden, "A Study of the Optical Properties of Semiconductor Crystallites" Chapter 4, Ph.D thesis, University of Glasgow (1992).

2.2. "Model 2040 and 2045 High Power Ion Laser Instruction Manual", Spectra Physics Laser Products Division.

2.3. "Model 590 Dye Laser Instruction Manual", Spectra Physics Laser Products Division.

2.4. "Laserspec III Instruction Manual".

2.5. "Ramanor U1000 Monochromator Operating Instructions", Jobin Yvon Division d'Instruments S.A.

2.6. M. Watt, "Inelastic Light Scattering by Low-dimensional Structures", Chapter 4, Ph.D Thesis, University of Glasgow, (1989).

2.7. "Enhanced Prism Software Instruction Manual", version 1.2, Jobin Yvon Division d'Instrument S.A.

2.8. "Photomultiplier Power Supply Type PM288/VP Opertating Manual", Thorn EMI Electron Tubes Ltd.

2.9.   "Instructions, Models 3457, 3461, 3463, 3470 Thermoelectric PMT housings", Pacific Instruments Inc.

2.10.   "Model 33 Power Supply/Temperature Controller Operation and Maintenance Manual", Pacific Instruments Inc.

2.11.   C. J. Adkins, "Equilibrium Thermodynamics" 3rd Edition, pp. 174, Cambridge University Press, 1983.

2.12.   I. T. Ferguson, "Optical Properties of Novel GaAs-Based Semiconductors", Chapter II, Ph. D Thesis, University of St. Andrews, 1986.

2.13.   A. Jayaraman, Rev. Mod. Phys. **55**, 65 (1983).

2.14.   A Van Valkenburg, Conference Internationale Sur-les Hautes Pressions, Le Creusot, Saoneet-Loire, France (1965).

2.15.   R. A. Forman, G. J. Piermarini, J. D. Barnett and S. Block, Science **176**, 284 (1972).

2.16.   G. J. Piermarini, S. Block and J. D. Barnett, J. Appl. Phys. **44**, 5377 (1973).

2.17.   A. Jayaraman, Rev. Sci. Instrum. **57**, 1013 (1986).

2.18.   A. Jayaraman, Rev. Sci. Instrum. **57**, 65 (1986).

2.19.   G. J. Piermarini, S. Block, J. D. Barnett and R. A. Forman, J. Appl. Phys. **46**, 2774 (1975).

2.20.   B. Weinstein, Rev. Sci. Instrum. **57**, 910 (1986).

2.21.   R. A. Naok and W. B. Holzapfel, "High Pressure Science and Technology", Plenum Press, New York, Vol. **1**, pp. 748 (1979).

3.1. M. R. Lorenz and A. Onton, Proc. 10th Int. Conf. Semicond. Phys., Cambridge-Mass, USAEC, New York 1970, pp. 444.

3.2. D. Oertel, D. Bimberg, R. K. Bauer and K. W. Carey, Appl. Phys. Lett. **5 5**, 140 (1989).

3.3. L. G. Shantharama, A. R. Adams, C. N. Armad and R. J. Nicholas, J. Phys. C **1 7**, 4429 (1984).

3.4. Z. Wasilewski and R. A. Stradling, Semicond. Sci. Technol. **1**, 264 (1986).

3.5. A. R. Adams and D. J. Dunstan, Semicond. Sci. Technol. **5**, 1194 (1990).

3.6. B. Wakefield, M. A. Halliwell, T. Kerr, D. A. Andrews, G. J. Davies and D. R. Wood, Appl. Phys. Lett. **4 4**, 341 (1984).

3.7. I. T. Ferguson, T. P. Beales, T. S. Cheng, C. M. Sotomayor-Torres and E. G. Scott, Semicond. Sci. Technol. **4**, 243 (1989).

3.8. G. J. Piermartini, S. Block, J. D. Barnett and R. A. Forman, J. Appl. Phys. **4 6**, 2779 (1975).

3.9. R. C. Weast, "CRC Handbook of Chemistry and Physics", pp. E101, (1983).

3.10. D. Olego, M. Cardona and H. Müller, Phys. Rev. **B 22**, 894 (1980).

3.11. C. S. Menoni and I. L. Spain, Phys. Rev. **B 35**, 7520 (1987).

3.12. S. W. Tozer and D. J. Wolford, Presented at 19th ICPS, Warsaw, Poland (1988).

3.13. R. N. Bhargava, Philips Tech. Rev. **3 2**, 261 (1971).

3.14. G. D. Pitt, J. Phys. C **6**, 1586 (1973).

3.15. H. Ohno, C. E. C. Wood, D. L. Rathbun, D. V. Morgan, G. W. Wicks and L. F. Eastman, J. Appl. Phys. 5 2, 4033 (1981).

3.16. D. J. Thomas, Physics Today 2 1, No. 2, 43, (1968).

3.17. S. Nakashima and Y. Yamaguchi, J. Appl. Phys. 5 0, 4958 (1979).

3.18. Z. Y. Xu, J. Z. Xu, W. K. Ge, B. Z. Zheng, J. Y. Xu and Y. Z. Li, Solid State Commun. 6 1, 707 (1987).

3.19. PJ. Dean, Prog. Solid State Chem. 8, 1 (1973).

3.20. J. Shah, R. C. C. Leite and J. P. Gordon, Phys. Rev. 1 7 6, 938 (1968).

3.21. J. A. W. Van der Does de Bye, A. T. Vink, A. J. Bosman and R. C. Peters, J. Luminescence 3, 185 (1970).

3.22. S. Nilsson and L. Samuelson, Solid State Commu. 6 7, 19 (1988).

3.23. A. Onton and R. J. Chicotka, Phys. Rev. B 4, 1847 (1971).

3.24. J. Shah, B. I. Miller and A. E. Digiovanni, J. Appl. Phys. 4 3, 3436 (1972).

4.1. L. Esaki and R. Tsu, IBM J. Res. Dev. 1 4, 61 (1970).

4.2. L. L. Chang and L. Esaki, in: "Progress in Crystal Growth and Characterization", edited by B. R. Pamplin (Pergamon, Oxford, pp1, 1979).

4.3. D. Gershoni and H. Temkin, J. Lumin. 4 4, 381 (1989), and references cited therein.

4.4. G. C. Osbourn, J. Vac. Sci. Technol. 2 1, 469 (1982).

4.5. J. C. Bean, T. T. Sheng, L. C. Feldman, A. T. Fiory and R. T. Lynch, Appl. Phys. Lett. **44**, 102 (1984).

4.6. J. W. Matthews and A. E. Blakeslee, J. Cryst. Growth **27**, 118 (1974).

4.7. G. C. Osbourn, Phys. Rev. **B 27**, 5126 (1983).

4.8. M. J. Ludowise, J. Appl. Phys. **58**, R31 (1985).

4.9. G. Armelles, M. Recio, J. Melendez, A. Ruiz, F. Briones, K. Khirouni and J. Barrau, Japan. J. Appl. Phys. **28**, L1495 (1989).

4.10. M. Recio, G. Armelles, J. Melendez and F. Briones, J. Appl. Phys. **67**, 2044 (1990).

4.11. D. Z. Ting and Y. C. Chang, Phys. Rev. **B 36**, 4359 (1987).

4.12. M. S. Skolnick, G. W. Smith, I. L. Spain, C. R. Whitehouse, D. C. Herbert, D. M. Whittaker and L. J. Reed, Phys. Rev. **B 39**, 1119 (1989).

4.13. F. Briones, L. Gonzalez and A. Ruiz, Appl. Phys. **A 49**, 729 (1989).

4.14. M. Potemski, J. C. Maan, T. P. Smith and L. L. Chang, Surf. Sci. **228**, 57 (1990).

4.15. J. Feldmann, J. Nunnenkamp, G. Peter, E. Gobel, J. Kuhl, K. Ploog, P. Dawson and C. T. Foxon, Phys. Rev. **B 42**, 5809 (1990).

4.16. Y. Masumoto, T. Mishina, F. Sasaki and M. Adachi, Phys. Rev. **B 40**, 8581 (1989).

4.17. M. V. Klein, M. D. Sturge and E. Cohen, Phys. Rev. **B 25**, 4331 (1982).

4.18. F. Minami, K. Hirara, K. Era, T. Yao and Y. Masumoto, Phys. Rev. **B 36**, 2875 (1987).

4.19. B. A. Wilson, C. E. Bonner, R. C. Spitzer, R. Fischer, P. Dawson, K. J. Moore, C. T. Foxon and G. W. t Hooft, Phys. Rev. **B 40**, 1825 (1989).

4.20. Y. Masumoto, T. Mishina and F. Sasaki, J. Lumin. **45**, 189 (1990).

4.21. K. J. Moore, P. Dawson and C. T. Foxon, Phys. Rev. **B 38**, 3368 (1988).

4.22. A. Chomette, B. Deveaud, A. Regreny and G. Bastard, Phys. Rev. Lett. **57**, 1464 (1986).

4.23. M. Nakayama, I. Tanaka, I. Kimura and H. Nishimura, Japan. J. Appl. Phys. **29**, 41 (1990).

4.24. M. Potemski, J. C. Maan, T. P. Smith and L. L. Chang, Surf. Sci. **228**, 57 (1990).

5.1. M. Haase, J. Qiu, J. M. DePuydt and H. Cheng, Appl. Phys. Letters **59**, 1272 (1991).

5.2. H. Jeon, J. Ding, W. Patterson, A. Nurmikko, W. Xie, D. Grillo, M. Kobayashi and R. L. Gunshor, Appl. Phys. Letters **59**, 3619 (1991).

5.3. D. D. Awschalom, J. Warnock, J. M. Hong, L. L. Chang, M. B. Ketchen and W. J. Gallagher, Phys. Rev. Lett. **62**, 199 (1989).

5.4. W. M. Becker, in: "Semiconductors and Semimetals", Vol. 25, Chapter 2, pp. 35 - 72, R. K. Willardson and A. C. Beer eds., Academic, New York (1972).

5.5. R. Brun Del Re, T. Donofrio, J. Avon, J. Majid and J. C. Wooley, Il Nuovo Cimento **2D**, 1411 (1983).

5.6. A. G. Thompson and J. C. Woolley, Can. J. Phys. **45**, 255 (1967).

5.7. J. A. Van Vechten, Proceedings of the Tenth International Conference on the Physics of Semiconductors, Cambridge, Massachusetts, pp 602, (1970).

5.8. J. A. Gaj, R. R. Galazka and M. Nawrocki, Solid State Commun. **2 5**, 193 (1978).

5.9. A. Twardowski, M. Nawrocki and J. Ginter, Phys. Stat. Sol. (b) **9 6**, 497 (1979).

5.10. N. Bottka, J. Stankiewicz and W. Giriat, J. Appl. Phys, **5 2**, 4189 (1981).

5.11. M. P. Vecchi, W. Giriat and L. Videla, Appl. Phys. Lett. **3 8**, 99 (1981).

5.12. Y. R. Lee and A. K. Ramdas, Solid State Commun. **5 1**, 861 (1984).

5.13. J. A. Gaj, "Semiconductors and Semimetals", Vol. 25, Chapter 7, pp. 275 - 309, R. K. Willardson and A. C. Beer eds., Academic, New York (1972).

5.14. G. Bastard, C. Rigaux, Y. Guldner, J. Mycielski and A. Mycielski, J. Physique **3 9**, 87 (1978).

5.15. S. A. Jackson, Surf. Science **1 9 6**, 654 (1988).

5.16. G. L. Bir and G. E. Pikus, "Symmetry and Strain-induced Effects in Semiconductors", Wiley ed., Section **2 3** and **2 4**, 1974.

5.17. J. A. Gaj, P. Byszewski, M. Z. Cieplak, G. Fishman, R. R. Galazka, J. Ginter, M. Nawrocki, R. R. Galazka, R. Planel, R. Ranvaud and A. Twardowski, In "Physics of Semiconductors" (14th Int. Conf.), Inst. Phys. No. **4 3**, pp. 1113 (1979).

5.18. G. W. Williams, A. G. Cullis, C. R. Whitehouse, D. E. Ashenford and B. Lunn, Appl. Phys. Lett. **5 5**, 1303 (1989).

5.19. D. Heiman, P. Becla, R. Kershaw, D. Ridgley, K. Qwight, A. Wold and R. R. Galazka, Phys. Rev. **B34**, 3961 (1986).

5.20. U. Venkateswaran, M. Chandrasekhar, H. R. Chandrasekhar, B. A. Vojack, F. A. Chambers and J. M. Meese, Phys. Rev. **B 33**, 8416 (1986).

5.21. H. Mariette, F. Dalbo, N. Magnea, G. Lentz and H. Tuffigo, Phys. Rev **B 38**, 7740 (1988).

5.22. B. Gil, D. J. Dunstan, J. Calatayud, H. Mathiue and J. P. Faurie, Phys. Rev. **B 40**, 5522 (1989).

5.23. B. Gil and D. J. Dunstan, Semicond. Sci. Technol. **6**, 428 (1991).

5.24. G. J. Piermarni, S. Block, J. D. Barnett and R. A. Forman, J. Appl. Phys. **46**, 2779 (1975).

5.25. M. Zigone, H. Roux-Buisson, H. Tuffigo, N. Magnea and H. Mariette, Semicond. Sci. Technol. **6**, 454 (1991).

5.26. D. J. Dunstan, B. Gil and K. P. Homewood, Phys. Rev. **B 38**, 7862 (1988).

5.27. V. A. Wilkinson, D. E. Ashenford, B. Lunn and D. J. Dunstan, High Press. Res. **3**, 72 (1990).

5.28. U. Venkateswaran, M. Chandrasekhar, H. R. Chandrasekhar, B. A. Vojak, F. A. Chambers and J. M. Meese, Phys. Rev. **B 33**, 8416 (1986).

5.29. H. Q. Hou, L. J. Wang, R. M. Tang and J. M. Zhou, Phys. Rev. **B 42**, 2926 (1990).

5.30. W. A. Wilkinson, A. D. Prins, J. D. Lambkin, E. P. O'Reilly, D. J. Dunstan and L. K. Howard, Phys. Rev. **B 42**, 3113 (1990).

5.31. S. Adachi, J. Appl. Phys. **53**, 8775 (1982); **58**, R1 (1985).

5.32. P. Lefebvre, B. Gil and H. Mathieu, Phys. Rev. **B** **35**, 5630 (1987).

5.33. J. A. Gaj, R. Planel and G. Fishman, Sol. St. Commun. **29**, 435 (1979).

5.34. P. M. Young, H. Ehrenreich, P. M. Hui and K. C. Mass, Phys. Rev. **B** **43**, 2305 (1991).

5.35. A. Wasiela, Y. Merle d' Aubigne, J. E. Nicholls, D. E. Ashenford and B. Lunn, Solid State Commun. **76**, 263 (1990).

5.36. A. V. Nurmikko, Surf. Sci. **196**, 632 (1988).

5.37. D. D. Awschalom and M. R. Freeman, J. Luminescence **44**, 399 (1989).

5.38. J. M. Hong, D. D. Awschalom, L. L. Chang and Armin Segmuller, J. Appl. Phys. **63**, 3285 (1988).

5.39. J. Warnock, A. Petrou, R. N. Bicknell, N. C. Giles-Taylor, D. K. Blanks and J. F. Schetzina, Phys. Rev. **B** **32**, 8116 (1985).

5.40. X. C. Zhang, S. K. Chang, A. V. Nurmikko, L. A. Kolodziejski, R. L. Gunshor and S. Datta, Appl. Phys. Lett. **47**, 59 (1985).